Weak intermolecular interactions of imidazole, urea and thiourea studied by microwave spectroscopy

John Connor Mullaney

Doctor of Philosophy

School of Chemistry

Newcastle University

November 2017

Abstract

Microwave spectroscopy is a powerful spectroscopic tool in determining the structure of gas phase molecules. The microwave spectra of imidazole, urea or thiourea containing complexes such as $(C_3N_2H_4)_2$, $(H_2N)_2CO\cdots HNCO$, $(H_2N)_2CO\cdots C_3H_4N_2$, and $H_2O\cdots CS(NH_2)_2$ have been recorded. The spectrum of various isotopologues have been measured in order to determine structural information. The geometry of these weakly bound complexes is investigated, alongside the nature of the weak intermolecular interactions present.

A chirped-pulse Fourier transform microwave spectrometer (CP-FTMW) has been used in the work detailed in this thesis to measure the spectra of such molecules. The instrument allows measurement of spectra over the full range of 6.5-18.5 GHz. The molecules presented in this thesis were formed as a result of laser vaporisation of solid organic precursors in the presence of argon introduced from a pulsed nozzle. The subsequent supersonic expansion generates rotationally cool molecules (~2 K) and stabilises the weakly bound complexes.

The $(C_3N_2H_4)_2$ complex was found to adopt a twisted configuration with a single stabilising intermolecular hydrogen bond. The $(H_2N)_2CO\cdots HNCO$ complex was observed to adopt an almost planar structure, forming two intermolecular hydrogen bonds. The N-H group of HNCO acts as both a hydrogen bond donor and acceptor. The $(H_2N)_2CO\cdots C_3H_4N_2$ complex was found to adopt a conformation where two intermolecular hydrogen bonding interactions around the N-H group of imidazole are present. Finally the $H_2O\cdots CS(NH_2)_2$ complex was found to contain two intermolecular hydrogen bonds, where water acts as a donor and acceptor forming $S\cdots H$ and $O\cdots H$ interactions. The results of *ab initio* calculations at the DFT (density functional theory), MP2 (second order Møller-Plesset perturbation theory) and CC (coupled cluster) level of theory are presented and compared to experimental results.

Acknowledgements

I would first like to thank my supervisor Nick Walker for giving me the opportunity to work with him, as both an undergraduate Masters student and later as a PhD student. His endless optimism despite many failed experiments has been a source of inspiration, from teaching me how to use PGOPHER a few years ago to always being amenable to ideas for new experiments.

I must thank all of the past and present members of the group who have all influenced me throughout my PhD in their own way. Susanna introduced me to the nuances of fitting spectra, and trained me in the early days, showing me how to press rods which would later become such a large part of my work. Dan impressed upon me the beauty of coding and the necessity of efficiency in a research lab. Chris has been a source of guidance, constantly modifying the instrument and always up for a pint after a long day. Dror taught me not to invest so much of myself in the outcome of experiments, along with many quirks that I found myself adopting. Eva has reminded me of the optimism and curiosity that first motivated me to start my PhD. In a similar vein, I must thank the various Masters students I have had the pleasure of working with over the years, who are too numerous to mention individually. Each challenged me in a different way, and taught me a great deal. Perhaps more appropriately I should apologise to all those that I've mentioned for putting up with me for quite so long.

Tony Legon must also be mentioned, for his guidance and assistance, in particular with the study of urea – isocyanic acid. Susana Blanco contributed to the work of urea – imidazole, taught me some tricks of the trade in sample preparation and was always a joy to be around. My parents and family must also be thanked for the support they have given me over the years and more recently while I have been finishing my PhD. Lastly I should thank the ERC for funding.

Table of Contents

1. Introduction

1.1 History and developments of microwave spectroscopy

Spectroscopy is concerned with the interaction of electromagnetic radiation with matter, depending on the type of radiation different properties can be determined. Microwave spectroscopy, for example, can be used to determine structural information of a molecule by its rotational transitions, using radiation in the 3 to 300 GHz region. Due to the relationship between rotational constants and moments of inertia, information such as bond lengths and angles can be determined from a rotational spectrum.

Ammonia was the first reported molecule to be investigated by microwave spectroscopy, by Cleeton and Williams[1] in 1934. Many other works[2-7] examined the structure of ammonia in the late 1940s, particularly the inversion vibration of the molecule. Many key observations were made such as evidence for hyperfine structure[8] and the presence of the Stark effect[9]. As microwave spectroscopy is a gas phase technique, originally smaller gas phase molecules, such as ammonia, were the first to be studied. As the technology surrounding microwave spectroscopy advanced, bigger and more complex molecules were targeted. For certain metals[10-11] it was shown that high temperature ovens could be used to generate species to probe by microwave spectroscopy in the gas phase, in the 1950s.

The results of laboratory experiments were used to identify the first stable molecule in the interstellar medium[12-13], ammonia. Measurements performed in the lab were compared to the spectra obtained by radio-telescopes, allowing for the identification of a handful of molecules[14-19] in the interstellar medium throughout the late 1960s and 1970s. Transitions observed by microwave spectroscopy continue to this day to be used in tandem with astronomical measurements to identify molecules present in the interstellar medium.

The popularity of the field grew with the work of Flygare and co-workers in the 1970s and 1980s with the advent of Fourier transform microwave (FTMW) spectroscopy. They used rapidly pulsed radiation to excite molecules and then measured the emission in the time domain which was Fourier transformed by a computer. This increased the sensitivity and signal to noise, compared to previous absorption studies. In the 1980s a microwave spectrometer with a Fabry-Perot cavity was reported[20-21], which is often referred to as a Balle-Flygare (BF) microwave spectrometer. Previously samples were commonly interrogated in waveguide cells. The spectrometer utilised

advances in pumping technology and employed a molecular beam source. Advantages of the subsequent supersonic expansion and adiabatic cooling are twofold; pressure broadening is reduced or eliminated and complexes that would usually dissociate at higher temperatures can form. This setup was popular throughout the 1980s and is in use within research groups to this day.

One of the limitations of the BF microwave spectrometer is the limited bandwidth. This meant that only a ~1 MHz range could be measured at once. Reported in 2008, Pate and co-workers[22] developed the first arbitrary waveform generator (AWG) based, chirped-pulse Fourier transform microwave (CP-FTMW) spectrometer, reinvigorating the field of microwave spectroscopy. The spectrometer has a bandwidth of 11 GHz and operated over the 7.5 to 18.5 GHz range. The large bandwidth significantly reduced spectral acquisition time compared to the BF setup. Since 2008, many groups now use similar CP-FTMW spectrometers.[23-26] It is particularly suited to the conformational survey of molecules, as the large bandwidth allows multiple conformers or isotopologues of a species to be measured simultaneously. The setup of the CP-FTMW spectrometer used to measure the rotational spectra presented in this thesis is of a similar design and is described in greater detail in section 3.

A recent advance in the field of microwave spectroscopy was the development of experiments that enabled the differentiation of asymmetric chiral molecules. Patterson and co-workers[27] first reported the technique in 2013, using a modified cavity spectrometer. The technique relies on the fact that the dipole moments of enantiomers are mirrored, and hence the sign of the product of the dipole moments is opposite for each enantiomer. This technique also allows determination of a value for the enantiomeric excess of a sample. Lobsiger and co-workers[28] later reported modifications to an existing CP-FTMW spectrometer that allowed them to perform similar three-wave mixing experiments with the addition of another set of antenna horns. Since 2013 this technique has seen use in probing a wide range of molecules from organic species such as carvone,[29] to metal containing species such as the chiral $[CpRe(CH_3)(CO)(NO)]$ complex, with a BF type spectrometer.[30]

1.2 Hydrogen bonding and the studies of weakly bound complexes

As mentioned previously, the use of molecular beam techniques allows weakly bound complexes to form and be studied by microwave spectroscopy. A significant amount of research has been conducted on the nature of weak interactions. Hydrogen bonding is ubiquitous in nature, from interactions between DNA base pairs, to protein structure, to the shapes water molecules adopt when forming clusters. There is much activity in the area of weakly bound complexes containing different interactions such as van der Waals, e.g. argon containing complexes, and π interactions, which will not be discussed here. The IUPAC definition of a hydrogen bond is as follows:

"The hydrogen bond is an attractive interaction between a hydrogen atom from a molecule or molecular fragment X-H in which X is more electronegative than H, and an atom or a group of atoms in the same or different molecule, in which there is evidence of bond formation."[31]

One of the first studies of an intramolecular hydrogen bond was carried out on glycoaldehyde[32-33]. It was found to contain an intramolecular O-H···O hydrogen bonding interaction. Other studies followed on other molecules that could contain an intramolecular hydrogen bond, such as the group of 2- substituted alcohols[34-35], for example, 2-methoxyethanol[36]. A recent study this year determined the structure of 4-aminobutanol,[37] which contains an intramolecular O-H···N hydrogen bonding interaction.

The first study of an intermolecular hydrogen bonding interaction using microwave spectroscopy was by Klemperer and co-workers[38] in 1972. The hydrogen fluoride dimer, $(HF)_2$, was observed with the dimer possessing a FH···F hydrogen bonding interaction between the individual HF units. The water dimer[39], $(H_2O)_2$, was reported shortly afterwards. A large body of work carried out by Legon and co-workers[40] throughout the 1980s and 90s examined the hydrogen bonding interaction in many complexes of the type B···HX, where B is a hydrogen bond acceptor, e.g. H_2O and HX is a hydrogen bond donor, e.g. HF. From a wide range of observations the empirical Legon-Millen rules[40] were established, which gave information on the gas-phase equilibrium geometries of B···HX complexes. They state that (i) the HX axis is coaxial with a nonbonding pair of electrons on B or (ii) it intersects the axis of the atoms forming a π bond. The first rule is definitive, if the molecule B has both nonbonding and π bonding electron pairs.

Since then, larger and more complex systems have been studied, varying from metal halide containing complexes of the form B···MX[41-43], to complexes containing biomolecules and their associated complexes when bound to a water molecule[44-45]. A large body of work has been performed in studying various systems and their associated gas phase complexes with water by high resolution spectroscopy. One example is the microwave study of the methanol water dimer by Stockman and co-workers[46] in 1997. The dimer exhibits a structure where water acts as a hydrogen bond acceptor and the alcohol group of methanol acts as a hydrogen bond donor.

The versatility of water and the hydrogen bonds it can form to organic molecules was demonstrated in the report of the tert-butylalcohol water dimer. In the work Evangelisti and Caminati[47] catalogue the typical types of complexes that organic molecules can form with water, for example where water acts only as a proton donor. Such is the case with a recent study in 2017[48] which reports the structure of a complex of isopropanol and water. Measurements from both CP and BF type FTMW spectrometers were used to probe the structure and characterise the barrier to the internal rotation of the hydroxyl group of one of the observed isomers.

The shape and types of hydrogen bonds formed by water give an insight into the nature of solvation, with a particularly popular area of research being the structure of water clusters. As mentioned previously, the microwave spectrum of the water dimer was first investigated in 1974 by Dyke and co-workers[39]. Recently the structure of the water hexamer, $(H_2O)_6$, was investigated by microwave spectroscopy. In 2012, Pérez and co-workers[49] reported the structure of three different isomers of the water hexamer. The three isomers were observed simultaneously in the same spectrum using a CP-FTMW spectrometer. They were able to observe only one isomer, the cage, while using argon as a backing gas and hence concluded that it is the lowest energy isomer of the water hexamer. Typically only the lowest energy conformer is observed when using argon as a carrier gas, which is a result of the cooling efficiency of argon. By investigating various different systems, such as those containing multiple cooperative hydrogen bonding interactions, information regarding the nature of the hydrogen bond can be gained. The types of molecules discussed in this thesis are all weakly bound complexes involving at least one intermolecular hydrogen bonding interaction.

1.3 Biomolecules and laser ablation

Molecules of biological importance have been widely studied by microwave spectroscopy as structure and conformation affects function and activity. Understanding how these biological molecules interact with each other, water and other biological molecules is of fundamental interest. Modelling larger structures, such as the active site of a protein, can be challenging theoretically. Experimental structures provide benchmarks and starting points for such problems, often by targeting smaller 'prototype' systems. As technology and the spectroscopic techniques used to characterise molecules evolve, bigger systems are able to be investigated.

Microwave spectroscopy is a gas phase technique, so often generating the target molecules in the gas phase is an important experimental consideration. Many research groups employ heating methods for studying solid molecules that possess a high vapour pressure. This technique can produce relatively large molecules in the gas phase, some being originally liquids, with enough intensity to observe the ^{13}C and ^{15}N isotopologues at natural abundance.[50-51] Heating techniques usually involve the use of a reservoir before the nozzle, where the carrier gas passes through and flows over the solid. Optimisation of the heating temperature is essential, too high a temperature can cause fragmentation and loss of monomer signal. Similarly too low a temperature can produce poor signals, as only a small amount of molecules will be produced in the gas phase.

Another widely used technique is laser ablation, also referred to as laser vaporisation. Some of the earliest rotational spectroscopy experiments that utilised laser ablation were to study metal containing complexes such as MgCl. Endo and co-workers[52] were able to observe MgCl in the gas phase using a modified BF type spectrometer and the second harmonic, 532 nm, of a pulsed Nd:YAG laser. Endo describes a laser ablation source that houses a solid rod, which is ablated by the laser. Designs of sources such as this and others by Smalley[53] and Gerry[54-55] would later influence the design of sources used by different groups. Most share common features such as a motor assembly to constantly rotate and translate a solid rod, so that a fresh surface is exposed to each laser pulse. This leads to improved signal stability and lifetime of solid sample.

Certain molecules can possess properties that make them less amenable to study by conventional heating techniques. The combination of high melting points, low vapour

pressure and relatively low thermal stability can mean that some larger biomolecules are experimentally challenging to generate in the gas phase by heating. Laser ablation presents an alternative method of generating molecules in the gas phase. For example, laser ablation was originally shown in the case of glycine[56] to be less efficient than traditional heated nozzle techniques. Lovas and co-workers used both techniques and initially found the signal strength to be greatly improved when using a heated nozzle reservoir as opposed to the fundamental 1064 nm of a pulsed Nd:YAG laser. One of the first experiments that demonstrated the effectiveness of laser ablation with respect to studying organic species was the study of thiourea[57] in 2004. Lessari and co-workers generated thiourea in the gas phase using the second harmonic of a pulsed Nd:YAG laser and measured its rotational spectrum using a BF type FTMW spectrometer.

The technique of laser ablation continues to adapt and evolve with inventive ways to study different types of systems constantly being developed. A recent study by Ecija and co-workers[58] in 2016 reports the rotational spectrum and structure of scopine, a naturally occurring tropane alkaloid. This is a particularly interesting case as scopine exists as a sticky syrup-like solid under standard conditions. Target rods were formed by mixing the scopine syrup with a glycine matrix and commercial binder, and subsequently ablated by an ultrafast UV laser beam, ~5 mJ per pulse, to generate scopine in the gas phase. It was shown that in this case, heated nozzle methods caused the molecule to isomerise at temperatures as low as 90 °C.

The work detailed in this thesis aims to explore the structure of complexes involving imidazole, urea and thiourea by microwave spectroscopy. Microwave spectroscopy was chosen to probe these species as it allows structural information to be determined. These complexes illustrate the hydrogen bonding capabilities of each individual unit. As discussed earlier, the nature of the hydrogen bonding of molecules of biological significance is of fundamental interest. The technique of laser ablation was chosen as it has been shown to be able to generate biological molecules in the gas phase for study by FTMW spectroscopy.

Imidazole is part of many naturally occurring substances such as alkaloids and is part of the amino acid histidine and the hormone histamine. It also makes up part of purine, an abundant heterocycle in natural products. Imidazole is also a moiety featured in many drugs. The geometry of the imidazole dimer was determined recently[59] from its microwave spectrum using the Newcastle CP-FTMW spectrometer, and is

discussed in further detail in section 4. Section 5 focusses on a hydrogen bonded complex formed between urea and isocyanic acid.[60] The hydrogen bonding of urea is of great importance to the fields of crystal engineering[61] and protein denaturing.[62] The amide group of urea is a simple prototype system of the peptide groups of proteins. Section 6 aims to expand on the previous sections by presenting a complex formed between imidazole and urea. Section 7 features a complex between thiourea and water, expanding on the body of work regarding organic molecules and their complexes with water.[63-65]

2. Theoretical background

2.1 Rotational spectroscopy

This chapter is concerned with explaining the theoretical basis of rotational spectroscopy. Rotational transitions are fitted to a Hamiltonian, allowing the determination of spectroscopic constants. All of the molecules presented in this thesis are asymmetric tops and as such this chapter will focus on relevant theoretical aspects. Both classical and quantum mechanical aspects will be considered.

2.1.1 The Born-Oppenheimer approximation

The energy of a molecule is mainly affected by the electronic, vibrational, translational and rotational motion. The Born-Oppenheimer approximation assumes that as electrons move significantly faster than nuclei that these components can be treated separately. The Schrödinger equation cannot be solved analytically so the Born-Oppenheimer approximation is often employed to solve the energy of a molecule. The total Hamiltonian can be expressed as:

$$H_{total} = H_{el} + H_{vib} + H_{rot} + H_{trans} \qquad (2.1)$$

Where el = electronic, vib = vibrational, rot = rotational and $trans$ = translational. Hence the total energy of a molecule can be expressed as:

$$E_{total} = E_{el} + E_{vib} + E_{rot} + E_{trans} \qquad (2.2)$$

With the wavefunction expressed as:

$$\Psi_{total} = \Psi_{el} \, \Psi_{vib} \, \Psi_{rot} \, \Psi_{trans} \qquad (2.3)$$

2.1.2 Rotation and the rigid rotor

In a rotating molecule, if each atom is treated as a point mass rigidly connected to the other atoms that all rotate about the centre of mass of the molecule then they will all have the same angular velocity, ω. The total angular momentum of such a molecule, **P**, given by classical mechanics, is defined in equation 2.4, where **I** denotes the moment of inertia.

$$\mathbf{P} = \mathbf{I} \, \omega \qquad (2.4)$$

The moment of inertia tensor in a 3 axes, *a*, *b*, *c*, system is given by the matrix:

$$\mathbf{I} = \begin{pmatrix} I_{aa} & I_{ab} & I_{ac} \\ I_{ba} & I_{bb} & I_{bc} \\ I_{ca} & I_{cb} & I_{cc} \end{pmatrix} \qquad (2.5)$$

If the axes about a body are arbitrarily chosen such that the origin lies at the centre of mass then the diagonalised moment of inertia tensor is given by:

$$\begin{pmatrix} I_{aa} & 0 & 0 \\ 0 & I_{bb} & 0 \\ 0 & 0 & I_{cc} \end{pmatrix} \qquad (2.6)$$

where the I_{aa} I_{bb} and I_{cc} represent the moments of inertia in the system such that:

$$I_{aa} = \sum_i m_i (b_i^2 + c_i^2) \qquad (2.7)$$

$$I_{bb} = \sum_i m_i (a_i^2 + c_i^2) \qquad (2.8)$$

$$I_{cc} = \sum_i m_i (a_i^2 + b_i^2) \qquad (2.9)$$

The axes *a*, *b*, and *c*, are known as the principal inertial axes and are labelled so that:

$$I_{aa} \leq I_{bb} \leq I_{cc} \qquad (2.10)$$

The rigid rotor Hamiltonian has the form:

$$H = AP_a^2 + BP_b^2 + CP_c^2 \qquad (2.11)$$

where P_a, P_b and P_c represent the components of angular momentum of rotation and *A, B* and *C* are the rotational constants, in Hz, are defined as

$$A = \frac{h}{8\pi^2 I_{aa}}, \quad B = \frac{h}{8\pi^2 I_{bb}}, \quad C = \frac{h}{8\pi^2 I_{cc}} \qquad (2.12)$$

Molecules can be classified geometrically, from the magnitude of their moments of inertia or rotational constants. In the case of asymmetric tops,

$$I_{aa} \neq I_{bb} \neq I_{cc} \qquad (2.13)$$

such that:

$$A > B > C \qquad (2.14)$$

The degree of asymmetry in a molecule can be given by means of Ray's asymmetry parameter, κ, where:

$$\kappa = \frac{2B - A - C}{A - C} \tag{2.15}$$

κ = 1 indicates the limiting case of an oblate symmetric top and κ = -1 indicates the limiting case of a prolate symmetric top. κ = 0 indicates the most perfectly asymmetric case. All of the molecules presented in this thesis are classified as asymmetric tops.

The inertial defect, Δ, is related to the moments of inertia by the relationship:

$$\Delta = I_{cc} - I_{aa} - I_{bb} \tag{2.16}$$

For the perfectly planar case, using equilibrium values for the moments of inertia, Δ = 0. Most of the molecules presented in this thesis are not planar, and have an inertial defect that reflects this. The inertial defect can be a useful way of determining the degree of planarity of a molecule from the rotational constants without any prior structural determination or knowledge of the species.

2.1.2 Energy levels and selection rules

The energy of an asymmetric top can be given by the rearranged rigid rotor Hamiltonian:

$$H = \tfrac{1}{2}(A + C)P^2 + [\tfrac{1}{2}(A - C)(P_a^2 + \kappa P_b^2 + P_c^2)] \tag{2.17}$$

The rigid rotor Hamiltonian is not sufficient to fit the spectrum of molecules with respect to experimental uncertainty. A quantum mechanical approach is taken and an effective Hamiltonian is derived. Terms can be added to account for effects such as centrifugal distortion or nuclear quadrupole coupling which is described later.

The energy for a particular level of an asymmetric top may be expressed as:

$$E = \tfrac{1}{2}(A+C)J(J+1) + \tfrac{1}{2}(A-C)E_\tau \tag{2.18}$$

where J is a quantum number representing angular momentum, E_τ is a function of Ray's asymmetry parameter, κ, equation 2.15 and can also be expressed as $E_{K_aK_c}$. Solutions of E_τ are given elsewhere[66] and will not be described here. Simplified solutions exist for the energy levels of near prolate and near oblate asymmetric rotors and are given in reference 66.

For transitions to occur between energy levels a set of selection rules must be obeyed. Most importantly, a molecule must possess a permanent dipole moment in order to be

observed by rotational spectroscopy. Asymmetric molecules have allowed transitions when:

$$\Delta J = \pm 1, 0 \qquad (2.19)$$

In asymmetric tops the quantum number K, which is used for symmetric tops, is no longer suitable to describe the rotational energy levels and the King-Hainer-Cross notation of K_a and K_c is instead used. The ΔK_a / ΔK_c selection rules for transitions of asymmetric tops are outlined in table 2.1. Rotational transitions can be labelled J_{KaKc}. The type of transitions depend on the dipole moments about the inertial axes. A dipole moment about the a axis of a molecule, for example, is denoted as μ_a. Most of the molecules discussed in this thesis have large μ_a dipole moments and as such exhibit mostly a-type transitions.

Dipole component	ΔK_a	ΔK_c
$\mu_a \neq 0$	0, ±2, ...	±1, ±3, ...
$\mu_b \neq 0$	±1, ±3, ...	±1, ±3, ...
$\mu_c \neq 0$	±1, ±3, ...	0, ±2, ...

Table 2.1. Selection rules for asymmetric tops

2.1.3 Centrifugal distortion

Molecules experience centrifugal force as they rotate, distorting bonds and angles. Asymmetric tops are complex and require more terms to describe the energy levels of rotation, where it is required to add quartic centrifugal distortion constant terms Δ_J, Δ_K, Δ_{JK}, δ_J and δ_K to the total Hamiltonian. Watson[67] has outlined two ways of reducing the Hamiltonian of asymmetric tops. The A reduced Hamiltonian is given below, with the S reduced Hamiltonian including centrifugal distortion terms is available elsewhere.[68]

$$H^A = \tfrac{1}{2}(B^A + C^A)J^2 + [A^A - \tfrac{1}{2}(B^A + C^A)]J_z^2$$
$$+ \tfrac{1}{2}(B^A - C^A)(J_x^2 - J_y^2) - \Delta_J J^4 - \Delta_{JK} J^2 J_z^2$$
$$- \Delta_K J_z^4 - 2\delta_J J^2(J_x^2 - J_y^2) + \delta_K[J_z^2(J_x^2 - J_y^2) + J_z^2(J_x^2 - J_y^2)] \ldots \qquad (2.20)$$

where J_x/J_y/J_z are angular momentum vectors of the principal axes and:

$$J^2 = J_x + J_y + J_z \qquad (2.21)$$

2.1.4 Nuclear quadrupole coupling

Molecules with atoms that possess a nuclear spin larger than $I = \frac{1}{2}$ present further splitting of rotational transitions. This splitting arises from the nuclear angular momentum and molecular angular momentum coupling due to the interaction between the electric field gradient of the molecule at the nucleus and the nuclear electric quadrupole.

The spin angular momentum of a quadrupolar nucleus is given by

$$\mathbf{I} = [I(I + 1)]^{1/2} \hbar^2 \tag{2.22}$$

As a result of the electric field gradient, the spin angular momentum couples to the rotational angular momentum. The total angular momentum, F, can be expressed by

$$\mathbf{F} = \mathbf{J} + \mathbf{I} \tag{2.23}$$

Where F can take the values

$$F = J + I, J + I - 1, ... |J - 1| \tag{2.24}$$

With the selection rule

$$\Delta F = 0, \pm 1 \tag{2.25}$$

With this coupling each rotational transition is split into multiple components, the splitting of which, decreases with increasing J. Factors such as the number of quadrupole nuclei, the spin angular momentum and the nuclear quadrupole moment affect the extent of the splitting observed. This is significant for some of the molecules presented in this work, for example, where more than two quadrupolar nuclei are present. Splitting as a result of nuclear quadrupole coupling is accounted for by addition of nuclear quadrupole coupling terms to the overall Hamiltonian.

Nuclear quadrupole coupling constants, χ_{aa}, χ_{bb} and χ_{cc}, are used to describe the coupling of the nuclear spin of a nucleus with the overall spin of the molecule in the three inertial axes. The nuclear quadrupole coupling constants are related such that:

$$\chi_{aa} + \chi_{bb} + \chi_{cc} = 0 \tag{2.26}$$

2.1.5 Line widths and sources of broadening

The Heisenberg uncertainty principle gives the lifetime of an excited state in relation to the uncertainty in its energy:

$$\Delta t \, \Delta E \approx \hbar \qquad (2.27)$$

Where the spread of the energy of the state can be described by:

$$\Delta v \approx \frac{1}{2\pi\Delta t} \qquad (2.28)$$

Spontaneous emission can be the limiting factor for some spectroscopic techniques. This proves to be insignificant when it comes to microwave spectroscopy, with resulting natural linewidths of the order of ~10^{-5} - 10^{-7} Hz which is negligible when compared to other sources of broadening.

Pressure broadening can be a source of significant spectral broadening. Collisions can shorten the lifetime of excited states and by extension increase the uncertainty in their emitted energy. In the experiments described in this thesis molecular beam techniques are employed to reduce the number of collisions, to eliminate pressure broadening.

Doppler broadening can result from the differing velocities of molecules within the vacuum chamber, with respect to a detector. Some BF type Fourier transform microwave (FTMW) spectrometers[69-71] observe rotational transitions as Doppler doublets.

2.2 Principles of FTMW spectroscopy

Before the advent of FTMW spectroscopy absorption techniques were favoured in the field of microwave spectroscopy. With the development of pulsed molecular beam and pulsed laser techniques in the 1970s, a way to perform pulsed microwave spectroscopy became desirable. FTMW spectroscopy uses the interaction of an electric field with the dipole moments of molecules in an ensemble. After a microwave field or pulse is applied this creates a macroscopic dipole moment in the ensemble. This ensemble begins to emit radiation resonant to molecular rotation, which decreases in intensity over time as a result of relaxation, increasing disorder in the ensemble, and or collisions. This technique is similar to NMR techniques, where a radiofrequency magnetic field interacts with the nuclear magnetic moments of molecules in an ensemble.

The density matrix can be used to describe the ensemble. Approximating the ensemble, of N particles, as optically thin and 'two level', wherein only two rotational energy levels are considered, the density matrix $\rho(t)$ is given by its elements:[72]

$$\rho_{mn}(t) = \frac{1}{N} \Sigma_{v=1}^{N} c_{vn}^{*}(t)c_{vm}(t) \tag{2.29}$$

The time dependence of $\rho(t)$ is given by:

$$i\hbar \frac{\delta\rho}{\delta t} = [H, \rho] = H\rho - \rho H \tag{2.30}$$

where H is the Hamiltonian of a two level particle. Equation 2.30 is a generalisation of the time dependent Schrödinger equation with:

$$H = H_0 + H_1 \tag{2.31}$$

where H_1 denotes the part of the Hamiltonian that describes the time dependence of the microwave field and collisions. By neglecting collision interactions this gives:

$$\hat{H}_1 = -2\mu . \varepsilon \cos [\omega(t - t_0) - kz] \tag{2.32}$$

where ε is the amplitude of the microwave field, μ is the molecular dipole moment operator, ω is the angular frequency of the radiation of the microwave field, z is the direction of the propagation of the microwave field and k is given by the relationship with the phase velocity, c_p.

$$k = \omega / c_p \tag{2.33}$$

The time dependence of the density matrix elements is given by:

$$\dot{\rho}_{mm} = ik\varepsilon \cos[\omega(t - t_0) - kz](\rho_{nm} - \rho_{mn}) \tag{2.34}$$

$$\dot{\rho}_{nn} = -ik\varepsilon \cos[\omega(t - t_0) - kz](\rho_{nm} - \rho_{mn}) \tag{2.35}$$

$$\dot{\rho}_{mn} = i\omega_0\rho_{mn} + ik\varepsilon \cos[\omega(t - t_0) - kz](\rho_{mm} - \rho_{nn}) \tag{2.36}$$

$$\dot{\rho}_{nm} = \dot{\rho}_{mn} \tag{2.37}$$

If $k = 2\mu_{mn}/\hbar$ then the polarization in a given volume, z, is given by:

$$P(t,z) = N\,Tr\,(\mu\rho) \tag{2.38}$$

where P represents the macroscopic dipole moment of the ensemble consisting of N molecules, and Tr denotes the trace. P can be expressed as two different parts, N_a and N_b, where one is in phase with the microwave field and the other is in quadrature, i.e. separated in phase by π / 2. The two parts can be expressed as:

$$N_a = N\,\rho_{mm} \tag{2.39}$$

$$N_b = N\,\rho_{nn} \tag{2.40}$$

The difference in population is given by:

$$\Delta N = N_a - N_b = N(\rho_{mm} - \rho_{nn}) \tag{2.41}$$

Simplifying equations 2.34 – 2.36 as shown by Dreizler[72], partly by using the rotating-wave approximation, wherein rapidly oscillating terms are neglected, leads to the optical Bloch equations, shown in equations 2.42 – 2.44. With the assumption that ΔN relaxes to zero, ΔN_0. The relaxation times are given by T_1 and T_2 for the relaxation of P_r and P_i to zero respectively.

$$\dot{P}_r + (\omega_0 - \omega)\,P_i + \frac{P_r}{T_2} = 0 \tag{2.42}$$

$$\dot{P}_i - (\omega_0 - \omega)P_r + 2\varepsilon\frac{\hbar}{4}k\Delta N + \frac{P_i}{T_2} = 0 \tag{2.43}$$

$$\frac{\delta}{\delta t}\left(\frac{\hbar}{4}\Delta N\right) - \varepsilon P_i + \frac{\hbar}{4}\frac{\Delta N - \Delta N_0}{T_1} = 0 \tag{2.44}$$

Assuming the period of the microwave pulse is much shorter than T_1 and T_2 such that:

$$t_1 - t_0 \ll T_1, T_2 \tag{2.45}$$

and that:

$$1 / (k^2\varepsilon^2 + (\Delta\omega)^2)^{1/2} \ll T_1, T_2 \tag{2.46}$$

Equations 2.42 – 2.44 can be approximated to:

$$\dot{P}_r + \Delta\omega P_i = 0 \tag{2.47}$$

$$\dot{P}_i - \Delta\omega P_r + k^2\varepsilon \frac{\hbar}{4} \Delta N = 0 \tag{2.48}$$

$$\frac{\hbar}{4} \Delta\dot{N} - \varepsilon P_i = 0 \tag{2.49}$$

With the starting conditions of P_r and $P_i = 0$ at t_0 gives a solution for the above equations. An additional term can be added, as described by McGurk and colleagues[73] to account for the Doppler effect in the optical Bloch equations.

The maximum signal that can be obtained for a resonant microwave pulse is given by:

$$k\varepsilon(t_1 - t_0) = (2n + 1) \pi / 2, \qquad n = 0, 1, ... \tag{2.50}$$

which simplifies further for a $\pi / 2$ pulse to:

$$t_{\pi/2} - t_0 = \pi / 2k\varepsilon \tag{2.51}$$

With the advances in high speed arbitrary wave form generator (AWG) technology brings the opportunity to excite molecules with a chirped pulse, in a time shorter than T_2. The electric field of a linear frequency sweep that is produced by a chirped pulse is given by:

$$E(t) = E_{max}e^{i(\omega_0 t + \frac{1}{2}\alpha t^2)} \tag{2.52}$$

where E_{max} represents the peak electric field of the pulse, which is constant across the whole chirped pulse, α represents the linear sweep rate and ω_0 is the initial frequency. The instantaneous frequency is given by:

$$\omega_{inst} = \frac{d}{dt}(\omega_0 t + \frac{1}{2}\alpha t^2) = \omega_0 + \alpha t \tag{2.53}$$

The sweep range of the pulse, $\Delta\omega$, is related to the duration of the pulse, t_p, such that:

$$\Delta\omega = \alpha t_p \tag{2.54}$$

18

As a result, the frequency range of the excitation and the energy transmitted to the ensemble can be separately controlled. The signal resulting from an excitation using a chirped pulse can be described by:

$$S \propto \omega \, \mu^2 \, E_{pulse} \, \Delta N_0 \, (\pi/\alpha)^{1/2} \qquad (2.55)$$

where ω is the frequency, μ is the transition dipole moment, E_{pulse} is the strength of the electric field. The implications and the efficiency of excitation using a chirped pulse is further explored by Brown and co-workers.[22]

In order to optimally polarise samples CP-FTMW spectrometers require more peak power, relative to BF type spectrometers. BF type spectrometers feature a cavity that creates a resonance that amplifies signals. The bandwidth covered with each microwave pulse is also another important consideration with regards to power. To solve this problem high power components such as travelling wave tube (TWT) amplifiers are used in most CP-FTMW spectrometer setups.

2.3 Structural determination

Microwave spectroscopy can provide structural information, due to the relation of rotational constants to the mass and position of atoms in a molecule. A few methods are employed in the structural analysis of molecules presented in this thesis and are described in sections 2.3.2 to 2.3.3. Where appropriate, the results of these methods are presented alongside calculated equilibrium, r_e, structures.

2.3.1 Equilibrium structure, r_e

The equilibrium structure refers to the hypothetical structure at the bottom of the potential energy curve. As rotational constants depend on the vibrational state of the molecule, determining the equilibrium structure would require measurement of several vibrational states and isotopologues and as a result this is difficult to achieve experimentally. The relationship between the equilibrium rotational constant, B_e, and the rotational constants of a given vibrational state of a diatomic molecule, B_v, is given by:

$$B_v = B_e - \alpha_r(v + \tfrac{1}{2}) + ... \tag{2.56}$$

where α_r is the rotation-vibrational coefficient. Equilibrium bond lengths have been determined for simple molecules such as diatomics and triatomics to serve as benchmarks. One such example is the case of PbI and InI,[74] with some higher vibrational states measured using the Newcastle CP-FTMW spectrometer. For example, rotational transitions in vibrational states up to v = 11 was measured and fitted for InI yielding a full analytical potential energy function.

2.3.2 Effective structure, r_0

In the effective structure, also known as the ground state structure, structural parameters are least squares fit to the ground state rotational constants. This method assumes that the structure is the same independent of isotopic substitution, which is only valid for a rigid equilibrium structure. Introduction of different isotopes will have an effect on the zero-point vibrations of a molecule, meaning that position of lighter atoms in a molecule, such as hydrogen, are most greatly affected by this assumption due to the large change in relative mass.

Programs such as STRFIT, by Kisiel[75], have been developed in order to fit the effective structure of complicated molecules. The STRFIT program was used to fit the effective structures presented in this thesis. The program uses a least squares fitting

method to fit the moments of inertia of a species, and any measured isotopologues, to a given input model geometry. The amount of measured rotational constants of isotopologues determines what parameters can be fit using this method. The user generates an input file containing a model geometry that the program then fits the given set of measured rotational constants provided to.

2.3.3 Substitution structure, r_s

The coordinates of an atom in a molecule can be determined by isotopic substitution of that atom. Equations described by Kraitchman[76] relate the changes in the moments of inertia of a molecule from its isotopologues to determine the coordinates of substitution. For a full structure determination using this method, substitution at every atom position is needed which is often hard to achieve experimentally. Additionally, if the substituted atom is close to the centre of mass of the molecule this can lead to larger errors or even produce imaginary coordinates. The error of r_s coordinates can be estimated by an empirical rule[77] proposed by Costain:

$$\delta a_s = K / |a_s| \tag{2.57}$$

where K is usually set as a constant of 0.0015, and a_s represents the coordinate of an atom.

2.4 Spectral analysis and fitting

The spectra presented in this thesis were analysed using Western's PGOPHER[78] program. It allows the user to assign quantum numbers to rotational transitions and fit rotational, centrifugal distortion and nuclear quadrupole coupling constants to a Hamiltonian using a least squares fitting method.

Chapter 3. Experimental

3.1 Introduction

The experiments detailed in this thesis were performed with a CP-FTMW spectrometer which was originally based on the design reported by Pate and co-workers[22]. The instrument features some modifications such as the inclusion of a laser ablation source. The Newcastle CP-FTMW spectrometer was used in this work as opposed to the Newcastle BF spectrometer. The Newcastle CP-FTMW spectrometer[79] allows for measurement over 6.5 – 18.5 GHz range at once while the BF spectrometer can only measure ~ 1 MHz at one time. The BF type spectrometer offers greater sensitivity than the CP-FTMW spectrometer. Each instrument has distinct advantages and limitations but only the Newcastle CP-FTMW spectrometer will be discussed further here.

Typically the sequence of events of the experiments detailed in this work is as follows. First, a gas sample is pulsed into a vacuum chamber, undergoing supersonic expansion, which is described in further detail in section 3.5.3. Next, microwave radiation is broadcast into the vacuum chamber which will excite any molecules to a higher rotational state. The subsequent relaxation will cause microwave radiation to be emitted which is then recorded in the time domain, averaged and then fast Fourier transformed to generate the frequency domain spectrum. This process is repeated to improve the signal to noise ratio.

CP-FTMW spectrometers typically operate by broadcasting a high-powered microwave pulse into the vacuum chamber. Antenna horns are used due to their efficiency of broadcasting signals. More detailed descriptions of the circuitry and components of the Newcastle CP-FTMW spectrometer is given in section 3.2. The linewidth of the Newcastle CP-FTMW spectrometer is ~ 80 kHz which gives errors around the order of 10 kHz on peak positions. This uncertainty propagates through into the fitted constants from measured spectra.

The range of 6.5 – 18.5 GHz was originally selected by the Walker group for the aim of studying weakly bound complexes, historically these included metal halide complexes of the form B⋯MX, where B is a Lewis base. The frequency range is limited by the oscilloscope which operates over 0 – 12.5 GHz, which when mixed against a 19 GHz source gives a range of 6.5 – 18.5 GHz. This range was also chosen due to the affordability and availability of suitable electronic components. The trigger sequence and timings are critically important for these experiments and are discussed

further in section 3.3. A description of the vacuum chamber and components is given in section 3.4. Sample preparation and the two different laser ablation sources used in this work are discussed in section 3.5. The composition and method of creating target rods is described in section 3.5.2.

3.2 Microwave circuitry

The microwave circuitry of the Newcastle CP-FTMW spectrometer is outlined in sections 3.2.1 - 3.2.3. A schematic of the microwave circuitry is shown in figure 3.1. The following circuitry and components are necessary to effectively produce, control and transmit the high powered pulses and also detect the resulting free induction decay, (FID).

3.2.1 Polarisation circuit

A linear frequency sweep, also known as a chirp, is produced by a 10 GS/s arbitrary waveform generator (component A) which sweeps from 12.5 – 0.5 GHz with a duration of 1 µs. The AWG is referenced to a 10 MHz signal produced by a rubidium frequency standard (component B). The same component is used to reference the oscilloscope and phase-locked dielectric resonant oscillator (PLDRO) as phase matching is necessary to prevent destructive interference of signals.

The chirp is passed through a low pass filter (component C) and is mixed in a triple balanced mixer (component D) with a 19 GHz signal from a PLDRO (component E). This achieves a 6.5 – 18.5 GHz chirped pulse. The signal from the PLDRO passes through a filter (component F) and power divider (component G) prior to mixing. After mixing, the 6.5 – 18.5 GHz chirped pulse is amplified (component H) and subsequently passes through a bandpass filter (component I). Amplification is advantageous as the power of the chirp affects the intensity of the resulting emission. After attenuation by two attenuators (components J) in order to control the power of the chirp, it is further amplified by a traveling wave tube amplifier (component K) before being broadcast into the vacuum chamber by an antenna horn (component L).

3.2.2 Detection circuit

Another horn antenna (component L), in an opposite side of the vacuum chamber, detects the resulting FID of the gas sample. The signal passes through a pin diode limiter (component M) and then a pin diode single pole single throw switch (component N), which is in place to protect other components from the high power of the polarisation pulse. The switch is only open during the detection of the FID. The signal is then amplified by a low noise amplifier (component O) and an additional amplifier (component P), as molecular signals can be weak. After conversion by a triple balanced mixer (component D), which entails mixing with a 19 GHz signal produced by the PLDRO, it is filtered by a low pass filter (component Q). The signal is then

digitised by a 25 GS/s oscilloscope (component R) over a duration of 20 µs. The oscilloscope is also phase locked to the 10 MHz Rubidium frequency standard (component B).

3.2.3 Mixing

The range of 6.5 – 18.5 GHz, as mentioned previously, was chosen as this is a frequency range where the associated microwave components are widely available and affordable. It is also a region where transitions of interest lie, lower frequency ranges are suited for observation of heavier species. The range of the oscilloscope is 0 – 12.5 GHz so mixing of signals is required. As mentioned previously, the chirp is mixed with a 19 GHz signal from the PLDRO to achieve a 6.5 – 18.5 GHz excitation pulse. The FID is mixed by a triple balanced mixer with another 19 GHz signal from the PLDRO. Mixing twice is necessary to retain phase matching.
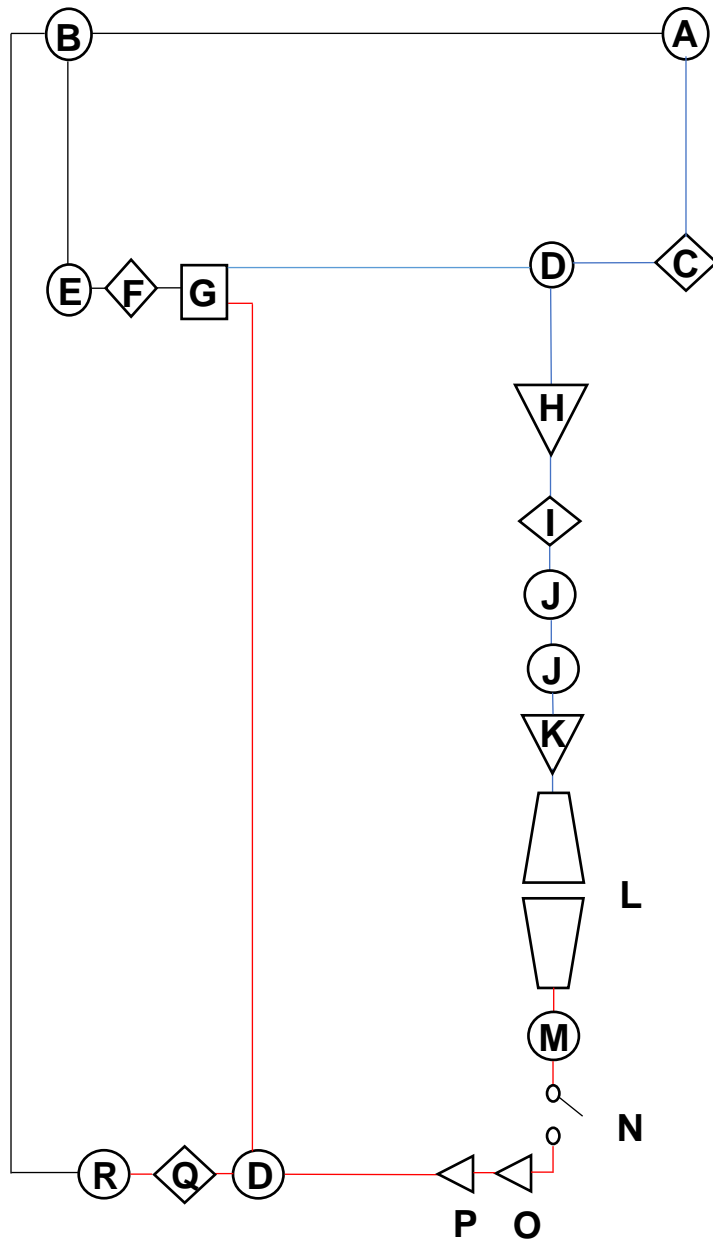
Figure 3.1 The microwave circuitry of the Newcastle CP-FTMW spectrometer. Blue lines show the polarisation circuit and red lines show the detection circuit. A) Arbitrary waveform generator, AWG7105, Tektronix. B) Rubidium frequency standard, FS725, Stanford Research Systems. C) Low pass filter, 12.2 GHz, Lorch. D) Triple balanced mixer, TBO 440LWI-R, MITEQ. E) PLDRO, XPDRO-14373, Herley CTI. F) Filter, 3C60-19000/T100-O/O, K&L Microwave G) Power divider, P218, ATM. H) Amplifier, JS4-02001800, MITEQ. I) Bandpass filter, 11SB10-12500/T12000-O/O, K&L Microwave. J) Attenuator, SA18S5W-03. K) TWT, L) Antenna horns, 750-442-C3, ATM. M) Pin diode limiter, ACLM-4539C6R1K. N) Pin diode single pole single throw switch, H8753-8OD, Arra. O) Low noise amplifier, AMF-5F-08001800-14-10P-R, MITEQ. P) Amplifier, AMF-5F-080018-14-10P-R, MITEQ. Q) Low pass filter, 11SBL10-12500/T19000-O/O, K&L Microwave R) Oscilliscope, DPO71254, Tektronix.

3.3 Trigger sequence and timings

Figure 3.2 depicts the general sequence of events of the experiment. The instruments used to control this sequence are described in greater detail below. The gas sample is pulsed into the chamber where it is polarised by high powered radiation. The switch of the detector circuit is closed during this process and for an adjustable time afterwards to protect the detection circuit. The FID is then measured after the detection switch is opened. The polarisation and detection can be repeated between gas pulses.
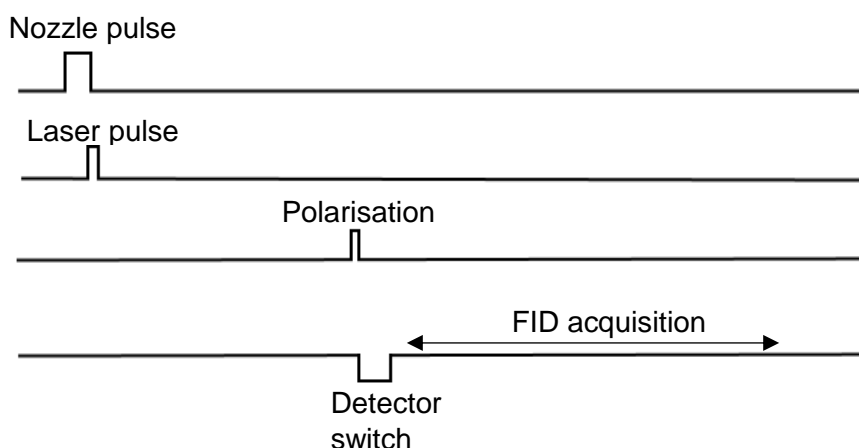
Figure 3.2 General sequence of events of the Newcastle CP-FTMW spectrometer, not to scale.

The trigger sequence is controlled by three instruments, two delay generators and an arbitrary waveform generator. Typically the experiment is triggered every 0.5 s, giving a 2 Hz repetition rate, however this is often adjusted depending on the system being studied. The repetition rate is limited by the pumping power of the current experimental setup. Most work detailed in this thesis was performed with the instrument operating at a 2 Hz repetition rate, except where otherwise stated.

The first delay generator (9520 series, Quantum composers) is triggered internally, setting the T_0 of the overall experiment. This generator has jitter of < 50 ps and contains four channels. The first channel is used to trigger an IOTA one pulse driver (Parker Hannifin), with a pulse of 2 μs and no delay with respect to T_0. The second channel triggers the AWG with a 51 μs pulse and a delay of 1.5 ms with respect to T_0. The third channel triggers the Q switch of a Nd:YAG laser (Minilite, Continuum) with a duration of 100 μs and a delay of 1.3 ms with respect to T_0. The fourth channel is used to trigger the flash lamp of the same Nd:YAG laser with a duration of 100 μs, and triggers 160

µs before the third channel. The flash lamp is triggered with respect to the Q switch allowing the power of the laser to be independently controlled, without affecting the laser pulse delay.

The AWG, as mentioned above, is triggered by the second channel of the first delay generator. The AWG has a trigger jitter of 30 ps. It produces 8 chirps in the 0.5 – 12.5 GHz range, with a duration of 1 µs and each separated by 25 µs. It also has two outputs which are used to trigger the second delay generator and the oscilloscope respectively. The first output, which triggers the second delay generator, has a pulse duration of 1 µs and a delay of 0.1 µs which is repeated 8 times, separated by 25 µs. The second output which triggers the oscilloscope, as described above, has a pulse duration of 1 µs and a delay of 3 µs, which is also repeated 8 times and separated by 25 µs. Triggering the oscilloscope with the AWG helps ensure the phase syncing of the time domain spectra.

The second delay generator (9518 series, Quantum composers) is triggered by the first output of the AWG and has a trigger jitter of < 50 ps. The first channel triggers the single pole single throw switch of the detection circuit with a pulse duration of 2 µs and a delay of 0.75 µs with respect to T_0 of the second delay generator. The second channel is used to trigger the TWT with a pulse duration of 1.5 µs and a delay of 1 µs with respect to T_0 of the second delay generator. The timing of the switch trigger is vital as it protects the rest of the detection circuit from the high power of the excitation pulse.

The FID is digitised by an oscilloscope (Tektronix, DPO71254) measured over a duration of 20 µs, with the oscilloscope having a sampling rate of 25 GS/s. 8 frames, each containing a measured waveform, are averaged to produce a 9th frame. The math channel of the oscilloscope averages the 9th frame, which is then saved regularly at specified intervals using a script written in Python[80]. The spectra are then averaged and Fourier transformed using a script written in Python. Window functions are applied to the waveform, with the High Resolution window function of Tektronix[81] being used throughout this work unless stated otherwise.

The timings of the trigger sequence are vitally important, and are usually optimised to maximise the intensities of observed signals. The stability of the triggers is also an important consideration. For example, the AWG has a low trigger jitter, 30 ps, and as such is used to trigger the oscilloscope. A 12.5 GHz signal has a period of 0.08 ns and

as such requires a sufficiently low jitter on the triggering of the oscilloscope to be able to average without loss of signal.

3.4 Vacuum chamber and pumps

The CP-FTMW spectrometer features a vacuum chamber as shown in figure 3.3.
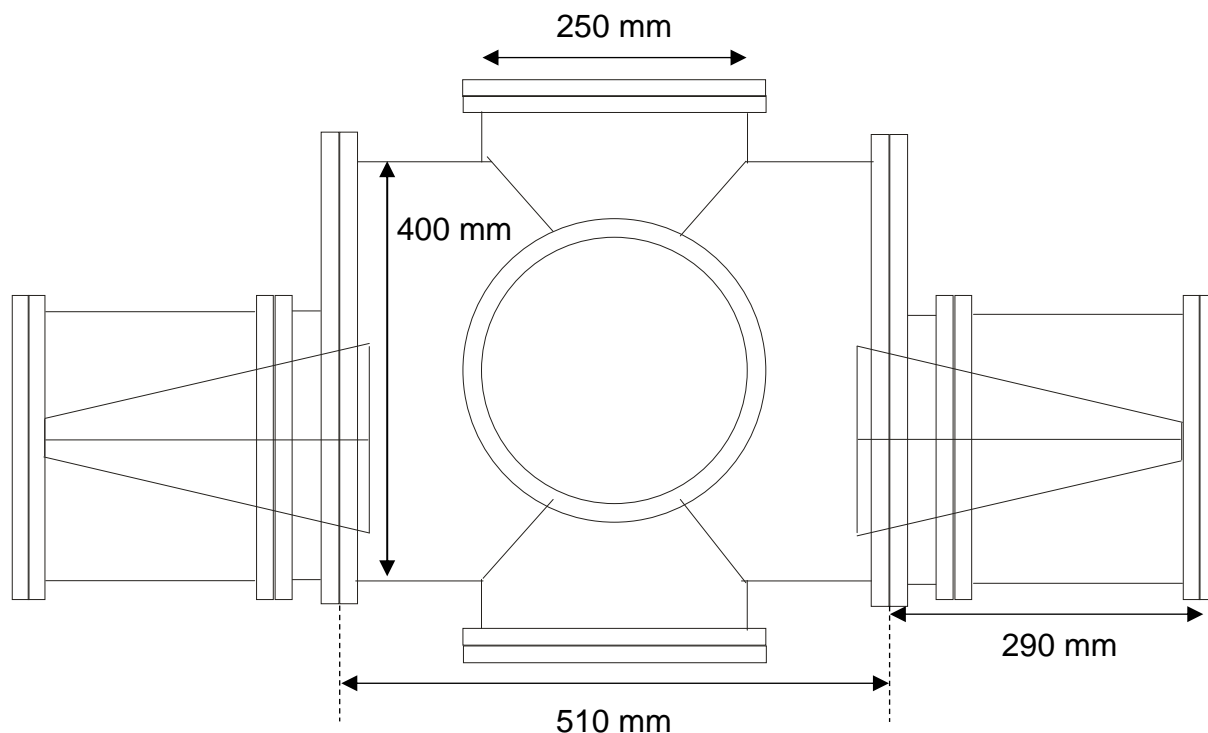
Figure 3.3 Schematic of the vacuum chamber of the Newcastle CP-FTMW spectrometer from a front view, showing both the antenna horns.

The chamber is constructed from a stainless steel six way cross, with ports for sections containing antenna horns, the pumping system and blank flanges for ease of access into the chamber. The bottom port connects to a diffusion pump (Diffstack 250, Edwards) which is backed by a mechanical booster pump (EH250, Edwards) and rotary pump (E2M40, Edwards). A pressure of $\sim 10^{-5}$ torr is achieved when fully pumped down. The pressure of the backing pump assembly and the main chamber are monitored by a Pirani gauge (APG100, Edwards) and Penning gauge (Edwards) respectively. The pressure of the chamber is important as it affects the character of the molecular beam, discussed in greater detail in section 3.5.3. The surface of the chamber is lined with microwave absorbent polyurethane foam (HR-1, Emerson and Cuming), to reduce any potential resonance after the polarisation pulse by reducing the reflections caused by the chamber walls.

3.5 Sample preparation

To generate solid organic precursors in the gas phase, the technique of laser ablation was used. The technique has been shown[56-58] to be effective at generating organic species in the gas phase. The second harmonic (532 nm, ~20 mJ per pulse) of a Nd:YAG laser (Minilite, Continuum) vaporises material from the surface of a solid target rod. The laser beam is perpendicular to the target rod and gas pulse. As discussed in section 1.3 most ablation sources are based on early designs by Smalley,[53] and Gerry[54]. The ablation sources used in the work detailed in this thesis are outlined below.

Target rods are prepared by grinding mixtures of the organic species with powdered copper. The mixture is then pressed into a rod using a benchtop press and die (Specac) to ~ 6 tonnes of pressure. Different dies are used to produce different sized rods, in these experiments rods with a diameter of both 5 mm and 13 mm were used. The composition of rods is further explored in section 3.5.2.

3.5.1 Ablation sources

Different sources (Figure 3.4 – 3.5) were used throughout these experiments and both were modified over time to improve their efficiency and minimise sample consumption. The smaller block, A, is designed for use with short, thin (5 mm diameter) target rods whereas block B was designed for use with much longer and wider (13 mm diameter) rods. Both share features such as a motor assembly so that the target rods are constantly rotated and translated, meaning a fresh surface is exposed to each laser pulse. The assembly consists of a micromotor (DC 1524 024 SR, Faulhaber) fixed to a planetary gearhead (Faulhaber).
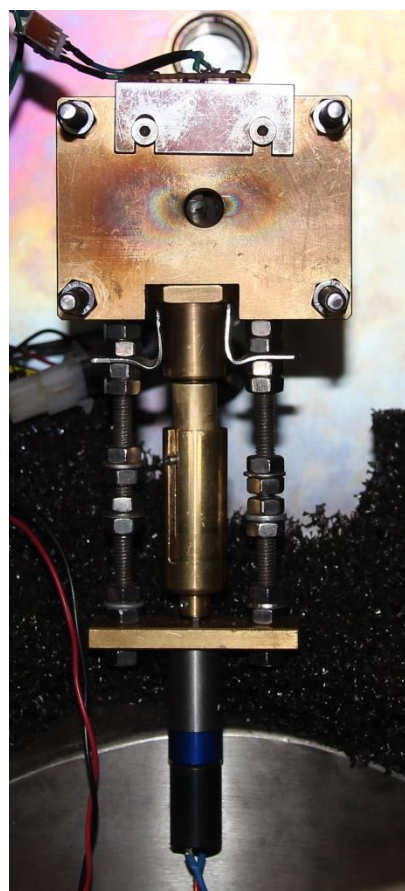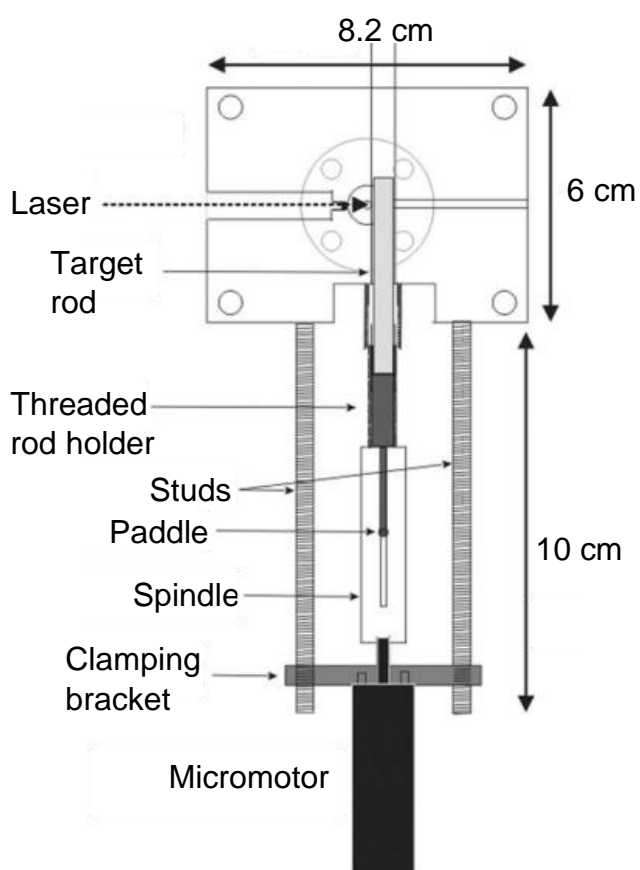
Figure 3.4 Schematic of ablation source A, alongside a photograph of the source inside the Newcastle CP-FTMW spectrometer.

Block A features an enclosed section where the rod is housed. The laser passes through a small hole in the block to reach the rod and vaporise material. This block is designed to place the rod near the nozzle, so that the expanding gas pulse will interact with the ablation plume. The rod winds into the threaded rod holder and presses a switch causing the direction to reverse and unwind from the block. The unwinding duration can be tuned allowing for spectra to be obtained even with very small amounts of sample.
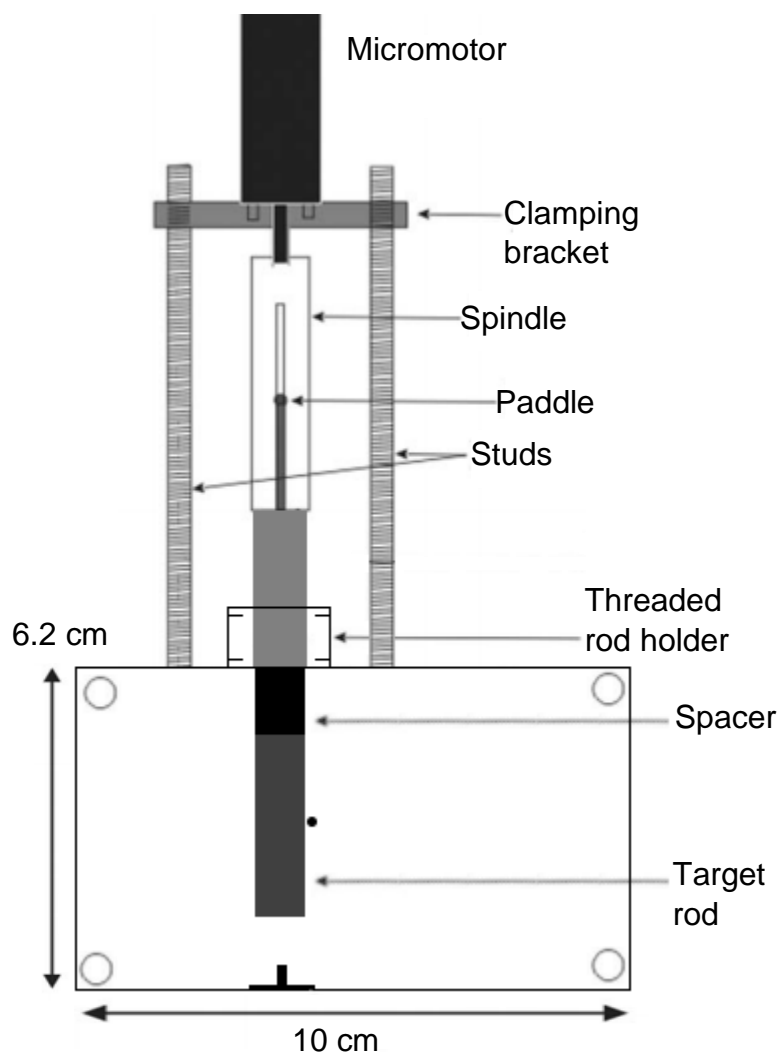
Figure 3.5 Schematic of ablation source B, alongside a photograph of the source inside the Newcastle CP-FTMW spectrometer.

Block B features a more open design and accommodates wider 13 mm diameter rods. The use of wider rods allows for a longer experiment, making it much more time efficient compared to using smaller rods and block A. The motor assembly is above the target rod, to prevent ablated material interfering with it. Similarly to block A, the rod winds into a threaded rod holder until it presses a button, causing it to unwind.

Block A was originally designed for the purpose of studying B···MX complexes, where B is a Lewis base and MX is a metal halide. Organic containing rods were found to deteriorate after short time periods of laser ablation, resulting in loss of signal and sample. The amount of sample required for compatible rods is significantly lower (>400

mg) than with block B (~4 g) and as such was useful for measuring the spectra of certain expensive synthetically enriched isotopologues. Block B was designed to study organic complexes as the wider rods allowed for a longer experimental run times.

For the experiments involving water, a bespoke reservoir based on other similar designs[82] was used. The reservoir is shown in figure 3.6 and was placed after the nozzle. The reservoir typically contained a small quantity of water, ~ 0.2 mL, in order to seed the molecular beam with water.

Figure 3.6 (Left): Photograph of the water reservoir used in this work. (Right): Photograph of the assembled nozzle and reservoir.

3.5.2 Rod composition

A series of experiments were performed to observe how rod composition affects signal intensity for a specific transition of imidazole, in order to optimise experimental conditions. These experiments involved grinding and compressing crystalline imidazole (Sigma-Aldrich, 99% purity) with powdered copper (Sigma-Aldrich, 98% purity) to form a target rod to ablate in the presence of a gas sample consisting of ~1% CCl_4 and the remainder argon held at a stagnation pressure of 6 bar. These experiments originally aimed to form a complex between imidazole and CuCl, as such, CCl_4 was included as a precursor. All other conditions except rod composition were kept constant. The results of these experiments are outlined in table 3.1, with the spectrum of two different compositions shown in figure 3.7. The intensities of lines due to species such as CH_3CN, and other fragmentation products, vary by rod composition, in general following the trend of imidazole monomer signals. Rods containing a 1:1 molar ratio of copper to imidazole was observed to produce the highest signal, and as such the experiments outlined in chapters 4 – 7 were performed using 1:1 molar ratios

of copper to organic species. Notably the imidazole signal observed was significantly worse when using rods of pure imidazole.

Molar ratio Cu : Imidazole	Imidazole signal[a] / μV
0:1	30.3
1:1	83.4
2:1	82.5
4:1	72.7
8:1	47.5
10:1	32.7
12:1	29.9
16:1	11.1

Table 3.1 Summary of the experimentally observed intensity of a specific transition of imidazole with various rod compositions. [a]Represented by intensity of $J' \rightarrow J'' = 3 \rightarrow 2$ of imidazole, 14146.04 MHz, in measured spectra.
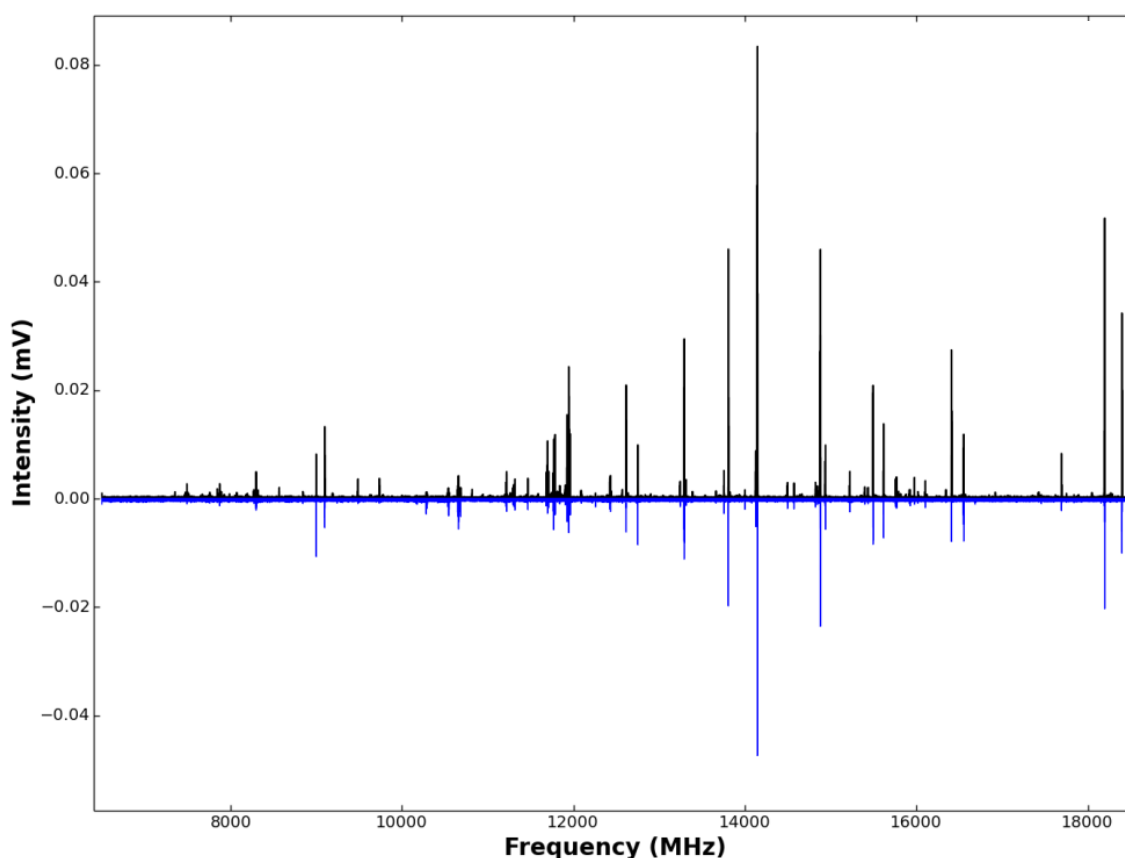
Figure 3.7 Microwave spectra of laser ablation of a copper imidazole rod, with a gas sample of 1% CCl_4 in 6 bar of argon. In black is the spectrum of a 1:1 molar ratio rod and in blue is the spectrum of an 8:1 molar ratio rod with the same conditions, as a negative. Both spectra are 30k FIDs.

3.5.3 Molecular beams and supersonic expansion

Expansion of a gas from an area of high pressure into an area of low pressure, such as a vacuum chamber, through a small orifice, produces what is known as a molecular beam.[83] Adiabatic cooling occurs when the gas rapidly expands, depleting the population of high energy vibrational and rotational energy states. This leads to an increase in population of the lower rotational and vibrational energy states. This is particularly effective for generating and studying weakly bound complexes as the cooling removes energy that can cause the complexes to otherwise dissociate. Molecular beams are also advantageous for use in high resolution gas phase spectroscopic techniques as they eliminate the source of pressure broadening. A supersonic expansion is depicted in figure 3.8.
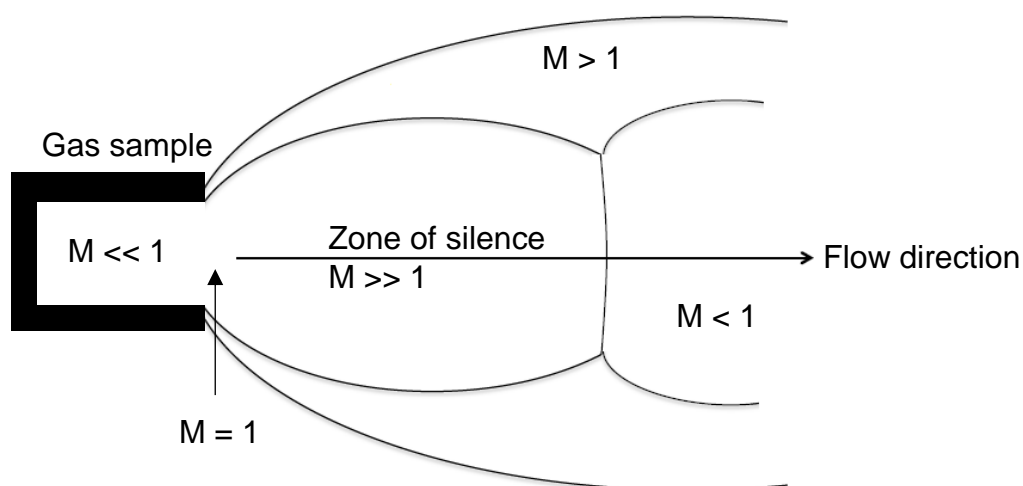
Figure 3.8 Schematic of a supersonic expansion showing the Mach number of specific areas.

The Mach number, M, can be described by the ratio of the velocity of the molecular beam to the speed of sound. In the zone of silence, the molecular beam is at its lowest temperature and hence it is favourable to interrogate the gas sample in this region. The length of the zone of silence is related to the pressure difference of the gas sample before the chamber and the pressure of the vacuum chamber itself. For this reason it is favourable to maintain a high level of vacuum in the chamber, in order to place this zone in the region of overlap between the two antenna horns.

Typically an inert carrier gas such as argon, neon or helium is used with a small amount of seeded reagent. In this work only argon was used in the gas sample, at a backing pressure of 6 bar. Other noble gases can be more expensive and argon provides efficient cooling of a molecular beam, due to its mass and thermal properties. One disadvantage is that argon has been known to form weakly bound Van der Waals complexes which may compete with any other complexes formed. A molecular beam is achieved in these experiments by pulsing the gas sample of argon through a pulsed nozzle (Parker, Series 9 general valve). The nozzle is connected to an ablation source, which is used to generate the organic molecules in the gas phase.

4. The geometry of the imidazole dimer

4.1 Introduction

Imidazole is an important component of purine, a widely abundant N-heterocycle in nature. It is also part of many naturally occurring compounds such as some alkaloids, and the amino acids histamine and histidine. For example, it has been shown that the imidazole unit of histidine plays a vital role in ammonia transport in bacterial membranes. [84-85] The structure of the ammonia transport channel depends on the intermolecular interaction between two distinct imidazole moieties of different histidines in the proteins. In this chapter the nature of the intermolecular interactions between imidazole will be studied and characterised using rotational spectroscopy.

The structure of imidazole has been studied by neutron diffraction,[86] which shows that all the atoms of the ring of imidazole are coplanar. These properties are highlighted in the crystal structure of imidazole[87-88] where a series of NH···N intermolecular hydrogen bonding interactions dominate. Due to the presence of both a pyridinic N atom and a pyrollic N atom, imidazole can act as both a hydrogen bond donor and acceptor. The neutron diffraction data also shows that all the atoms of the ring of imidazole are coplanar, with each unit involved in a hydrogen bonding interaction to another imidazole monomer. The crystal structure is shown to consist of a series of NH···N hydrogen bonding interactions, and that these interactions form units that stack, forming cooperative CH-π and elongated 3 centred H···N···H interactions.

Previous work by Choi[89-90] characterised the imidazole monomer, dimer, and the various water complexes through the use of IR spectroscopy. The complexes were studied using helium nanodroplets as a matrix. The studies showed that the imidazole dimer contains an intermolecular N-H···N hydrogen bonding interaction. This was observed by both the appearance of a new temperature dependent N-H band at 3515.8 cm^{-1} and the slight blue shift of the N-H band, compared to the N-H band of the imidazole monomer. In this work they performed a conformational survey of the imidazole dimer using second order Möller-Plesset perturbation theory (MP2) and the 6-311+G(d) basis set, alongside density functional theory calculations (DFT). They reported a twisted geometry, figure 4.1, for the dimer complex as a global minimum possessing a large dipole moment, wherein a single N-H···N hydrogen bond interaction is formed between the two imidazole monomers. Other low energy structures for the complex were reported, all being planar and involving two hydrogen bonding interactions, N-H···C and C-H···N, but differing by at least ~ 1420 cm^{-1} from the lowest energy structure. Most of these structures are symmetric and possess no dipole

moment overall and hence would not be able to be observed using microwave spectroscopy. This chapter aims to further characterise the imidazole dimer, to determine structural parameters such as the length of the intermolecular hydrogen bonding interaction. The results of the experiments detailed in this chapter have been published elsewhere.[59]
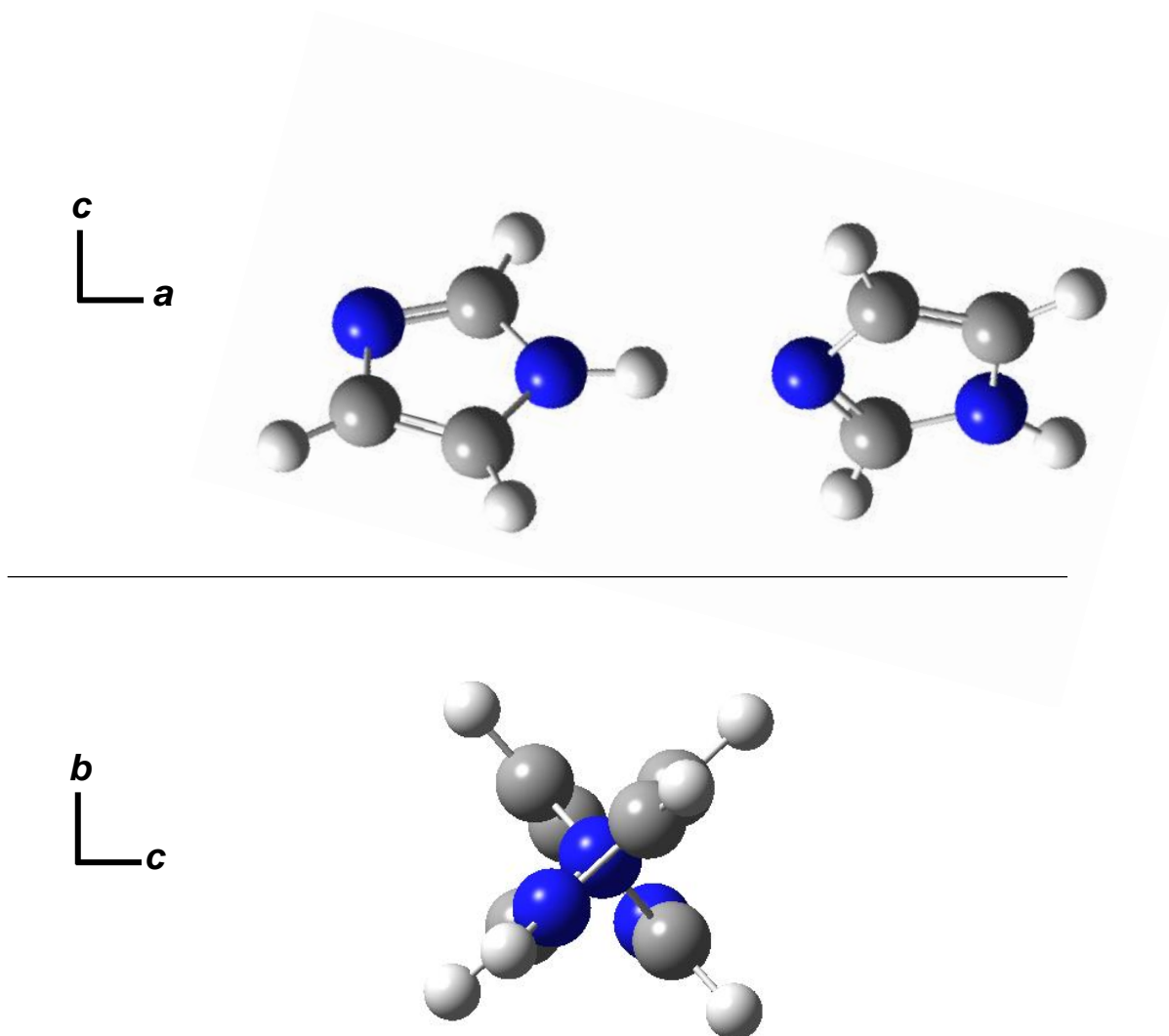
Figure 4.1. The proposed geometry of the imidazole dimer, based on IR spectra and calculations found in reference [89]. (Top) View of the molecule down the *b* inertial axis, (bottom): view of the complex down the *a* inertial axis.

41

4.2 Experimental details

Imidazole (Sigma-Aldrich, 99% purity) was used in the experiments in this chapter without further purification, alongside powdered copper (Sigma-Aldrich, 98% purity). Copper powder was used as this was shown to enhance the imidazole monomer signal and reduce sample consumption, which proved useful when performing experiments involving expensive synthetically enriched isotopologues. Target rods were produced using a table top press and 5 mm die (Specac), by grinding and mixing the solids together and applying ~6 tonnes of pressure. The effect of rod composition on the monomer signal intensity is discussed further in section 3.5.2, but it was found through a series of experiments the optimum composition was a 1:1 molar ratio of copper to imidazole. Further experiments involving synthetically enriched isotopologues of imidazole are detailed in this chapter. Imidazole-d_4 (CDN Isotopes, 98% purity, 97% D) was available commercially whereas the imidazole-d_1, where the N-H of imidazole is selectively deuterated, was prepared by a colleague by repeatedly dissolving imidazole in D_2O and freeze-drying to remove the solvent. The details of the CP-FTMW spectrometer used in the experiments in this chapter is described in section 3, however unlike the other experiments in this work, the repetition rate was set to 1.05 Hz due to the past limitations of the vacuum pumps.

4.3 Ab initio calculations

Using the geometry reported by Choi[89] as a starting point, calculations were initially performed at the MP2/6-311++G(d,p) level of theory to aid spectral assignment. The agreement between the experimentally determined constants and *ab initio* results is discussed later in section 4.4. The following coupled cluster (CC) calculations were performed by David Tew, of Bristol University. An approximation of CC level of accuracy was achieved by first optimising the imidazole monomers and dimer at the MP2 level of theory. This was to show which parameters change significantly upon forming the dimer complex, which was the length of the N-H involved in the hydrogen bonding interaction. An optimisation at the CCSD(T)(F12*)/cc-pVDZ-F12[91] level of theory was performed for the complex, keeping all but the N-H bond length fixed at MP2 optimised values for the monomers. The results of this calculation is shown in table 4.1.

	CCSD(T)(F12*)/cc-pVDZ-F12 $(C_3H_4N_2)_2$
A / MHz	4864.02
B / MHz	454.07
C / MHz	453.91
μ_a / D	9.38
μ_b / D	-0.08
μ_c / D	1.70

Table 4.1. The calculated rotational constants and dipole moment for the lowest energy conformer of $(C_3H_4N_2)_2$.

4.4 Spectral analysis

The 6.5 – 18 GHz spectrum was measured using the Newcastle CP-FTMW spectrometer. The full spectrum is shown in figure 4.2, where the most intense lines in the spectrum can be assigned to imidazole[92]. Other transitions can be assigned to various CN containing species including CH_3CN, CH_3CH_2CN, HCCCN, NH_2CH_2CN, HC_5N, HC_7N and CH_3C_3N, which have all been previously characterised by microwave spectroscopy.[93-99] The presence of these molecules shows that some amount of imidazole must undergo fragmentation and further reaction as a result of being vaporised. This is further evidenced in other experiments detailed in this work, such as section 5, which pertains to a complex formed between urea, and one of its products of thermal decomposition, isocyanic acid. Transitions that are not due to any previously reported species were observed and fit to the Hamiltonian of an asymmetric top. These lines exhibit a structured pattern that is characteristic of the *a*-type transitions of an asymmetric top with spacing of ~ 900 MHz.
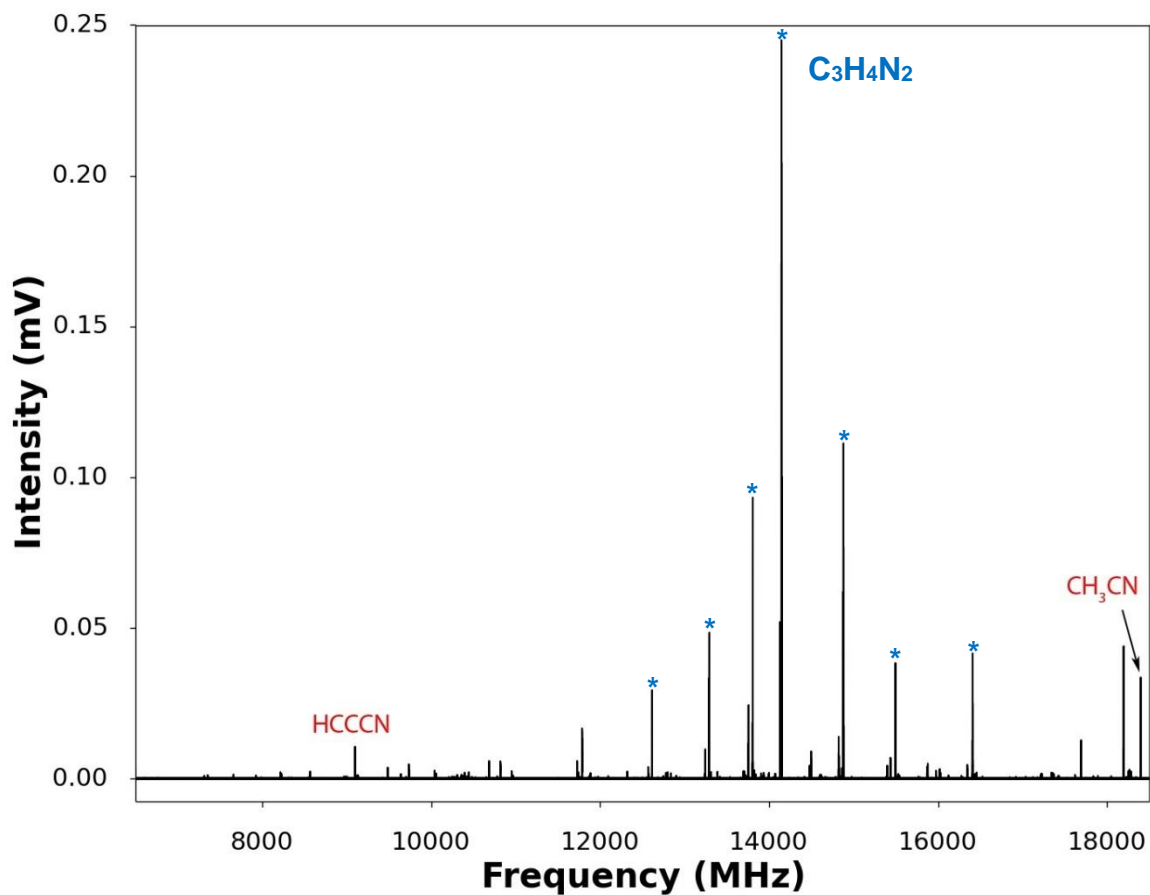
Figure 4.2 The broadband spectrum measured with ablation of a 1:1 molar ratio copper/imidazole rod in the presence of argon held at a stagnation pressure of 6 bar. The spectrum was obtained after adding 60k FIDs in the time domain, equating to data collected over 2 hours. Select transitions due to CH_3CN and HCCCN are labelled. Transitions due to $C_3H_4N_2$ are marked with asterisks.
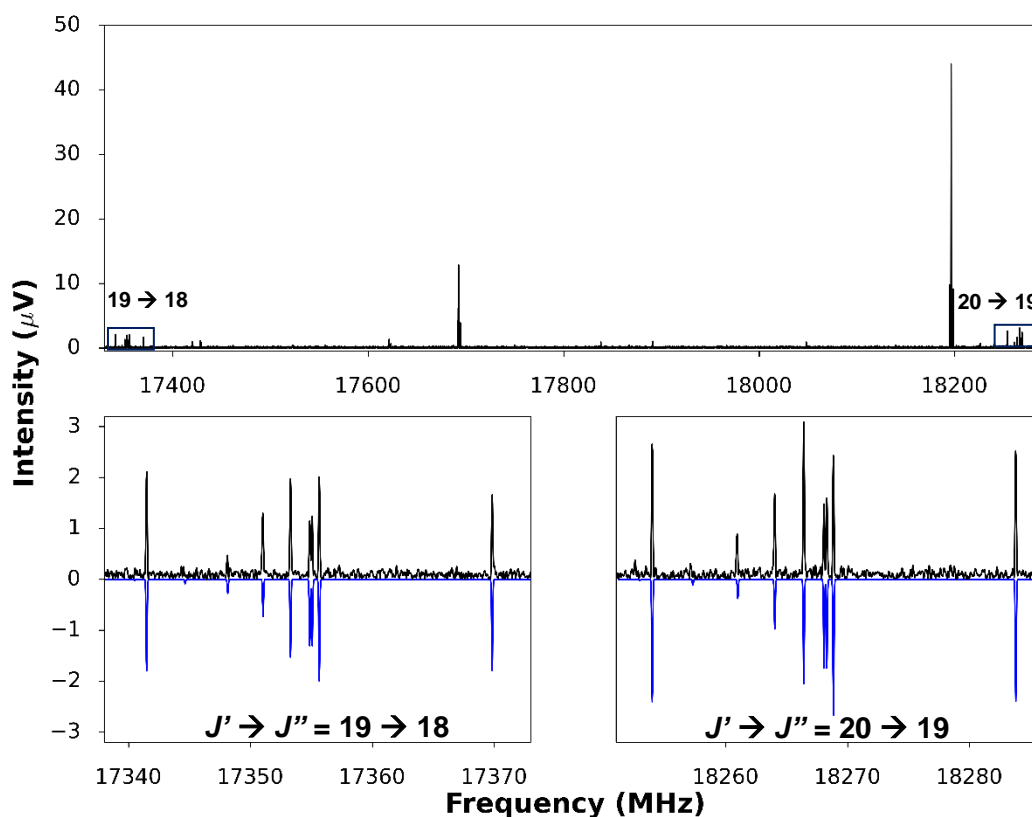
Figure 4.3. (Top): A section of the rotational spectrum, from 17.3 to 18.3 GHz, showing $J' \rightarrow J'' = 19 \rightarrow 18$ and $J' \rightarrow J'' = 20 \rightarrow 19$ of the $(C_3H_4N_2)_2$ complex. The most intense transitions displayed are due to HC_3N and $C_3H_4N_2$ respectively. (Bottom left): An expanded view showing $J' \rightarrow J'' = 19 \rightarrow 18$ transition in black and simulation in blue. (Bottom right): An expanded view showing $J' \rightarrow J'' = 20 \rightarrow 19$ transition in black and simulation in blue.

	Exp.	CCSD(T)(F12*)/cc-pVDZ-F12 $(C_3H_4N_2)_2$
A / MHz	4800(25)	4864.02
B / MHz	457.53869(27)	454.07
C / MHz	456.03871(26)	453.91

Table 4.2. The rotational constants determined for $(C_3H_4N_2)_2$ alongside the calculated constants from the r_e geometry.

Figure 4.3 shows two $J' \rightarrow J''$ transitions of the assigned species and the corresponding simulated fit. The simulations were generated using Western's PGOPHER[78] and subsequently the transitions were fit using the same program to the S reduced Hamiltonian of an asymmetric top. A comparison of the A, B and C rotational constants generated by geometry optimisation calculations to those of the fit are shown in table 4.2. The experimental results agree well with the calculated results, especially the B and C constants which were predicted within a few MHz. The appearance of only a-type transitions agrees with the calculated values of the dipole moment, which predicts $\mu_a = 9.38$ D, $\mu_b = -0.08$ D and $\mu_c = 1.70$ D. Given the signal to noise ratio of the observed a-type transitions and the relative predicted magnitude of μ_a and μ_c, c-type transitions were not expected to be observed as the signal intensity depends on μ^2. The full set of fitted constants is shown in table 4.3, alongside the constants determined from additional experiments using synthetically enriched imidazole.

In total 4 isotopologues were measured and assigned, the associated rotational and centrifugal distortion constants are shown in table 4.3. Figure 4.4 shows the same transition from two different isotopologues of the complex that was observed in a single experiment. Notably the signal to noise ratio of this transition of both species is much less than the transition shown in the bottom right panel of figure 4.3. The molar ratio of copper to organics was maintained, so in order to form the mixed species $(C_3H_4N_2)(C_3H_3DN_2)$, both $(C_3H_4N_2)$ and $(C_3H_3DN_2)$ were pressed into a single rod, in equimolar quantities. The identity of the species, based on the evidence of calculations and further experiments involving synthetically enriched isotopes, is therefore the lowest energy conformer of the $(C_3H_4N_2)_2$ complex.

	$(C_3H_4N_2)_2$	$(C_3H_4N_2)(C_3H_3DN_2)$	$(C_3H_3DN_2)_2$	$(C_3D_4N_2)_2$
A_0 / MHz	4800(25)	4710(50)	4680(53)	3970(16)
B_0 / MHz	457.53869(27)	457.32707(37)	449.86071(31)	422.81625(39)
C_0 / MHz	456.03871(26)	455.84958(38)	448.01603(31)	422.81625(39)
D_{JK} / kHz	8.3740(54)	8.299(15)	7.828(14)	7.311(11)
D_J / kHz	6.907(15)	6.773(22)	6.952(25)	5.926(18)
d_1 / Hz	−2.63(22)	−2.96(29)	−3.39(28)	-2.10(28)
N	63	36	39	43
$\sigma_{r.m.s}$ / kHz	6.4	7.9	6.9	8.0
D_3 / Hz	3.79(28)	4.4(7)	-	0.56(25)

Table 4.3. The ground state rotational and centrifugal distortion constants determined for $(C_3H_4N_2)_2$ and some of its isotopologues. D_3 was fitted separately to the other parameters and is derived in equation 4.1.
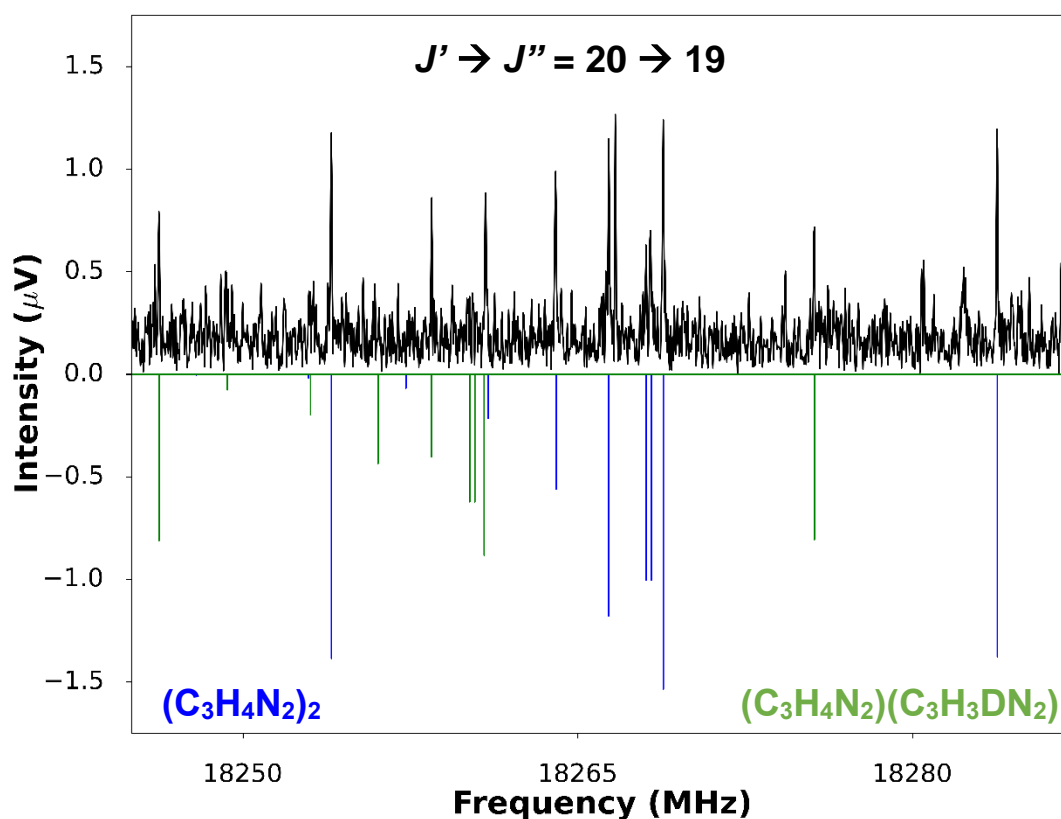
Figure 4.4. A small region of the microwave spectrum of the laser ablation of a 2:1:1 molar ratio rod comprised of copper, $C_3H_4N_2$ and $C_3H_3DN_2$. The $J' \rightarrow J'' = 20 \rightarrow 19$ transitions of $(C_3H_4N_2)_2$ are shown, simulated in blue, and $(C_3H_4N_2)(C_3H_3DN_2)$, simulated in green, 60K FIDs.

Further information can be provided by the asymmetry parameter, κ, which is defined earlier in section 2. A value for the determined constants, κ = 0.9993, shows that the species is a near prolate asymmetric top, which agrees with a twisted hydrogen bonded geometry proposed in section 4.1. Only one conformer of this species was observed under the current experimental conditions. Hyperfine splitting, due to the presence of the four nitrogen nuclei in the complex, was not observed. The splitting was calculated to be ~ 50 MHz, which is too low to be resolved with the Newcastle CP-FTMW spectrometer. The magnitude of the change in rotational constants from isotopologues can provide information about the structure before performing any structural analysis. For example, the slight change in A_0 in $(C_3H_4N_2)(C_3H_3DN_2)$ relative to the parent species indicates that the substituted hydrogen atom must be relatively near the centre of mass of the complex. This means that the deuterium in $(C_3H_4N_2)(C_3H_3DN_2)$ must be the N-D group that is involved in the intermolecular hydrogen bond.

Upon fitting the rotational constants A_0, B_0, C_0, and the centrifugal distortion constants D_J, D_{JK}, d_1 it was observed that numerous $K_a = 2$ transitions are split to a greater degree than can be accounted for by the magnitude of the rotational constants alone. This is due to a centrifugal distortion induced splitting of $K_a = n$ doublets which is observable in asymmetric rotors that are close to the limit of a prolate symmetric rotor, suggesting such is the case with the $(C_3H_4N_2)_2$ complex. The effect scales with $(J+1)^3$ and as such is only resolvable for transitions in this spectrum where $J' > 12$. This effect was only observed to significantly affect $K_a = 2$ transitions. Highlighted in figure 4.5 are the $K_a = 2$ lines of $J' \rightarrow J'' = 18 \rightarrow 17$ of $(C_3H_4N_2)_2$.
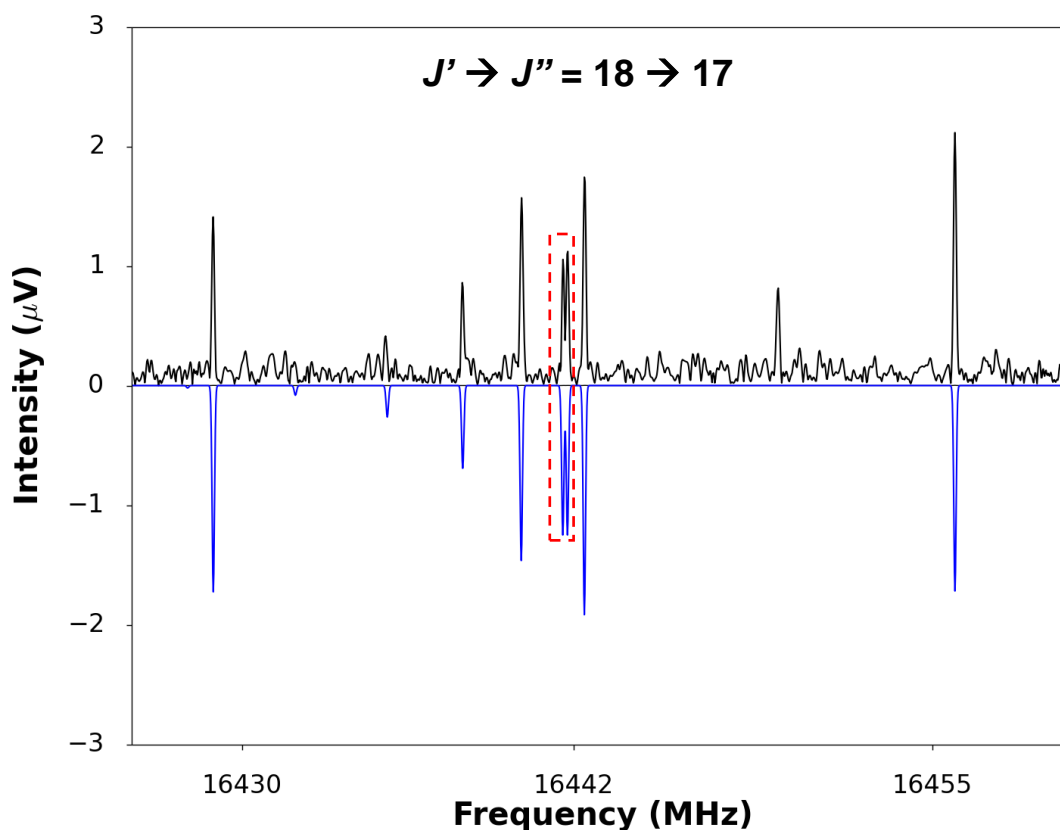
Figure 4.5. A region of the microwave spectrum, showing $J' \rightarrow J'' = 18 \rightarrow 17$ transitions of $(C_3H_4N_2)_2$, simulated in blue. Highlighted are two $K_a = 2$ lines.

This effect was first reported by Winnewisser[100-101] in the measurement of the microwave spectrum of HSSH and its isotopologue DSSD. The effect was observed in the less asymmetric DSSD, where $K = 3, 2$ transitions were split. It was observed that $K > 3$ transitions exhibited no observable splitting. Doubling of $K_a = n$ transitions in asymmetric tops occurs as a result of the inertial asymmetry and the asymmetry of the molecular force field. The former is responsible for the asymmetry splitting and the latter causes centrifugal distortion induced splitting. Usually the contribution of the centrifugal distortion is small in comparison to the splitting caused by asymmetry, hence the effect is only observable in certain near symmetric cases such as DSSD and the observed complex. Corrected transition frequencies were calculated using a mean value of D_3 for each isotopologue, which is determined by equation 4.1.[100]

$$D_3 = (obs - calc) / [4(J''+1)^3] \tag{4.1}$$

Where obs, in this case, refers to the observed frequency of a-type transitions having $K_a=2$, calc refers to the same transitions calculated after a preliminary fit excluding

50

K_a=2 transitions. D_3 is used in equation 4.2.

$$\text{corr} = \text{obs} \pm 4D_3(J''+1)^3 \tag{4.2}$$

Where corr refers to the corrected frequency of the K_a=2 transition. The sign applied depends on whether the This treatment was applied to $(C_3H_4N_2)_2$, $(C_3H_4N_2)(C_3H_3DN_2)$ and $(C_3D_4N_2)_2$ however the signal to noise ratio of $(C_3H_3DN_2)_2$ was too low to observe the K_a=2 transitions. An example of this applied correction is shown in tables 4.4 - 4.6. These corrected frequencies were used in the final fit of measured frequencies to determine the constants shown in table 4.2.

J'	J''	K_c'	K_c''	Obs / MHz	Calc / MHz	Corr / MHz
16	15	15	14	14615.075	14614.992	14615.001
16	15	14	13	14615.184	14615.252	14615.259
17	16	16	15	15528.354	15528.267	15528.266
17	16	15	14	15528.496	15528.580	15528.584
18	17	17	16	16441.631	16441.514	16441.527
18	17	16	15	16441.789	16441.885	16441.893
19	18	18	17	17354.856	17354.730	17354.735
19	18	17	16	17355.052	17355.166	17355.173
20	19	19	18	18268.054	18267.912	18267.914
20	19	18	17	18268.283	18268.421	18268.423

Table 4.4. List of K_a=2 transitions exhibiting the centrifugal distortion induced splitting of the $(C_3H_4N_2)_2$ complex. D_3 is determined by an average of equation 4.1 to yield D_3 = 3.79(28) Hz. Corrected frequencies are determined using equation 4.2

J'	J''	K_c'	K_c''	Obs / MHz	Calc / MHz	Corr / MHz
13	12	12	11	12782.910	12782.946	12782.957
17	16	17	16	16434.450	16434.343	16434.347
18	17	18	17	17347.300	17347.165	17347.182
18	17	17	16	17347.470	17347.600	17347.596

Table 4.5. List of K_a=2 transitions exhibiting the centrifugal distortion induced splitting

of the $(C_3H_4N_2)(C_3H_3DN_2)$ complex. D_3 is determined by an average of equation 4.1 to yield $D_3 = 4.4(7)$ Hz.

J'	J''	K_c'	K_c''	Obs / MHz	Calc / MHz	Corr / MHz
12	11	11	10	10167.030	10167.038	10167.025
12	11	10	9	10167.220	10167.216	10167.224
14	13	14	13	12708.500	12708.489	12708.489
14	13	13	12	12708.840	12708.837	12708.849
15	14	15	14	13555.590	13555.595	13555.601
18	17	17	16	16097.450	16097.470	16097.469
19	18	19	18	16943.790	16943.763	16943.772
19	18	18	17	16944.570	16944.588	16944.591
20	19	20	19	17790.750	17790.733	17790.728
20	19	19	18	17791.650	17791.687	17791.674

Table 4.6. List of K_a=2 transitions exhibiting the centrifugal distortion induced splitting of the $(C_3D_4N_2)_2$ complex. D_3 is determined by an average of equation 4.1 to yield $D_3 = 0.56(25)$ Hz.

4.5 Molecular geometry

In the structural treatment the geometry of each monomer in the complex is assumed to be unchanged from the r_0 geometry of the imidazole monomer except the N-H bond which is involved in the intermolecular hydrogen bonding interaction. This assumption is based on the results of *ab initio* geometry optimisation calculations, detailed in section 4.2, which show that the only structural parameter to significantly change in the dimer geometry is the N-H bond length. This is further supported by previously reported calculations in literature regarding the complex.[89-90] The N-H bond involved in the hydrogen bonding interaction was found to lengthen by 0.016 Å in the calculated complex. A correction of +0.016 Å is therefore applied to the N-H bond, on the assumption that the bond lengthens in the r_0 geometry of the dimer by the same magnitude of that in the calculated r_e geometry.
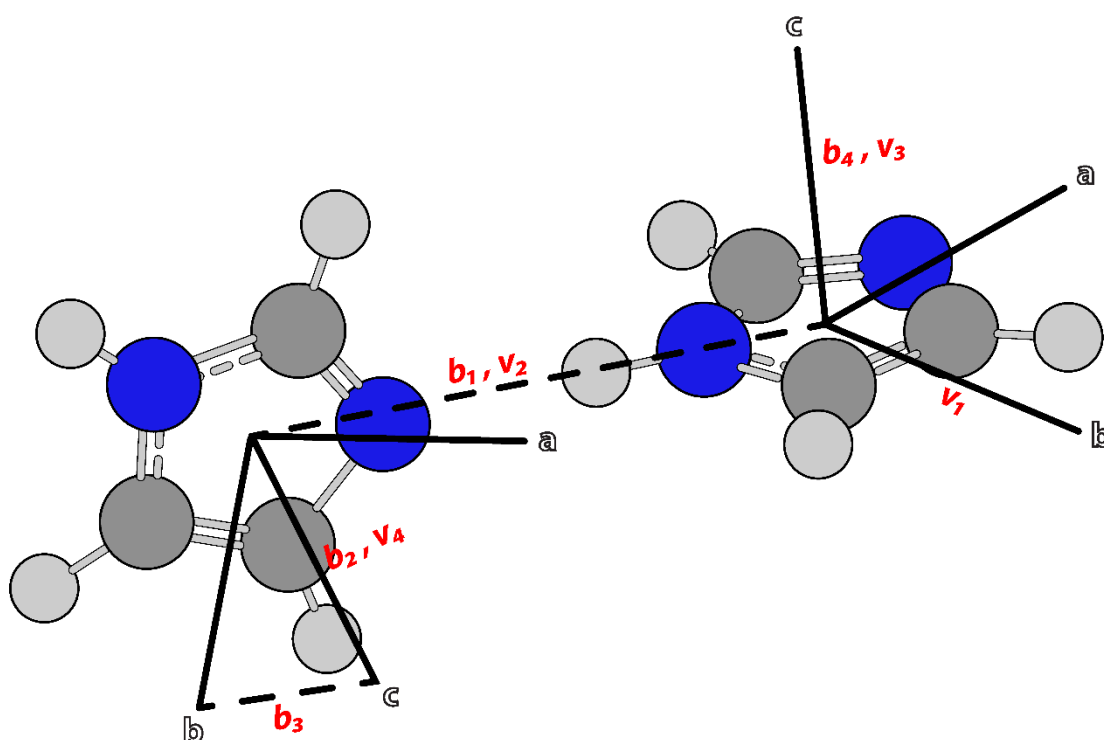
Figure 4.6. Diagram showing the vectors described in the text for the imidazole dimer and inertial axes (solid lines) of each respective imidazole monomer.

The geometry of the dimer, with reference to the inertial axes of the each monomer, is defined with the use of six intermolecular coordinates shown in figure 4.6 and defined by equations 4.3 – 4.7. One parameter not defined below is R_{CM} which is the distance between the centres of mass of each monomer unit in the complex and is shown as a dashed line in figures 4.6 – 4.7.

$$|v_3||v_2|\cos(\alpha) = v_3 \cdot v_2 \tag{4.3}$$

$$|v_1||v_2|\cos(\beta) = v_1 \cdot v_2 \tag{4.4}$$

$$|v_2||v_4|\cos(\theta) = v_2 \cdot v_4 \tag{4.5}$$

$$\phi = \text{atan2}([[b_1 \times b_2] \times b_2] \cdot [b_2 \times b_3], [b_1 \times b_2] \cdot [b_2 \times b_3]) \tag{4.6}$$

$$\gamma = \text{atan2}([[b_4 \times b_1] \times b_1] \cdot [b_1 \times b_2], [b_4 \times b_1] \cdot [b_1 \times b_2]) \tag{4.7}$$

Where $|v_n|$ are magnitude vectors and b_n are normalised vectors, as shown in figure 4.6. The angles α, β and θ are shown in figure 4.7 and are used to define the orientation of the second monomer with respect to the first. The tilting of the second monomer towards or away from the first is described by α. The turning of first monomer in the plane of the second is represented by β. Additionally, the twist of the second monomer about the line connecting the centres of masses of the two monomers is described by γ. Three of the parameters describe the positions of the monomers relative to one another. ϕ and γ represent the polar and azimuth angles.
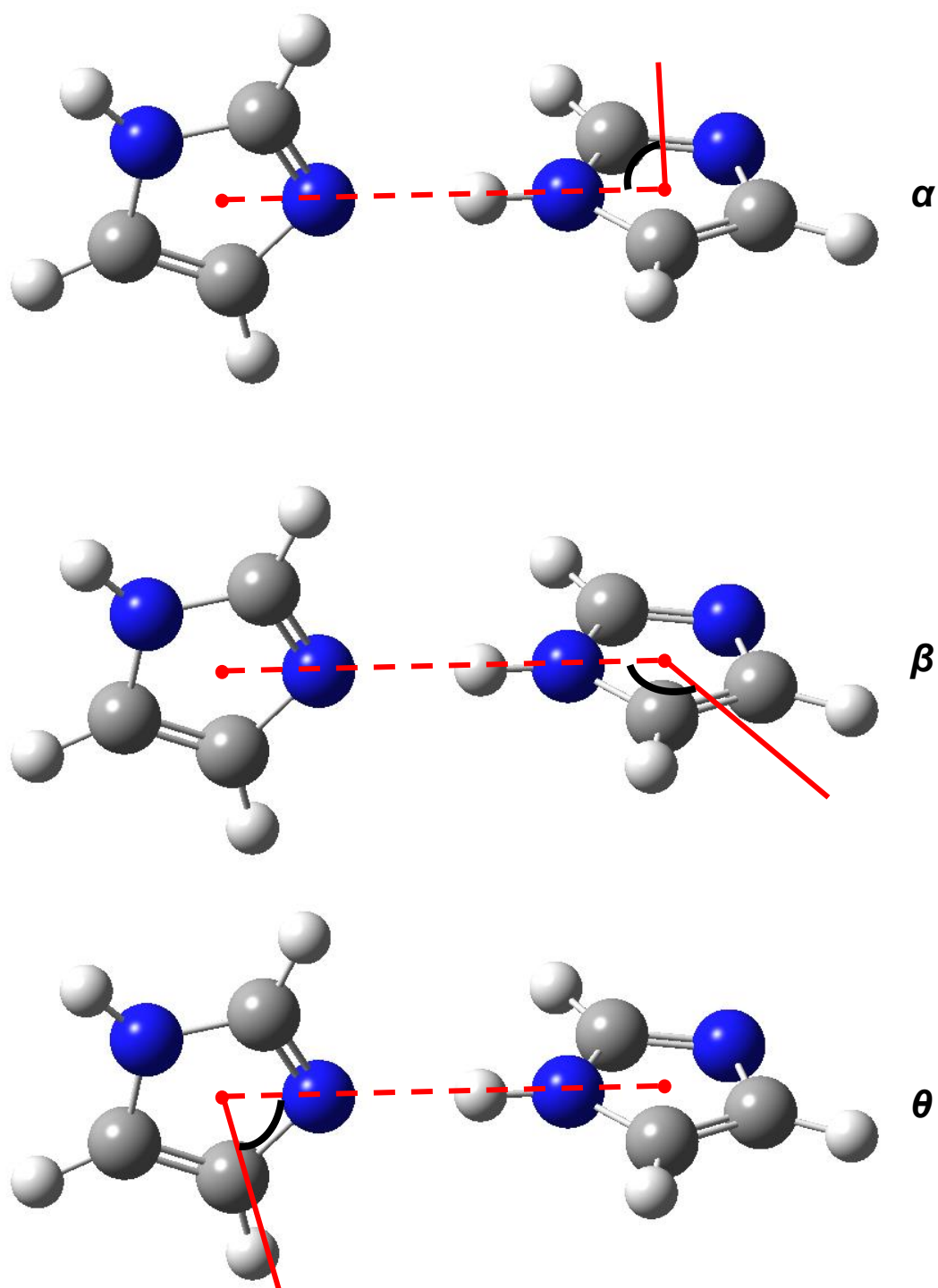
Figure 4.7. The geometry of the imidazole dimer, depicting three angles formed between the inertial axes (solid lines) and the axis formed by the centre of mass (red dots) of both monomers (dashed lines).

	r_0	r_e[a]
R_{CM} / Å	5.2751(1)	5.297
θ / °	[90][b]	90.0
ϕ / °	106.3(50)	99.9
α / °	[90][b]	90.0
β / °	122.3(54)	117.4
γ / °	87.9(4)	90.0
r(H···N) / Å	1.960[c]	1.947
$\angle$(NH···N) / °	169.3[c]	179.6

Table 4.7. Structural parameters for the model geometry of $(C_3H_4N_2)_2$.
[a] CCSD(T)(F12*)/VDZ level of theory.
[b] Fixed to calculated values.
[c] Not included in the set of parameters fit to the experimentally determined rotational constants. These are deduced from the values of fitted parameters.

Due to the lack of full isotopic substitution at all atom positions not all intermolecular parameters were able to be fitted. θ and α were fixed to the calculated value of 90°, based on the evidence of a twisted hydrogen bonded geometry provided by the *ab initio* results. The remaining parameters were fitted and are shown alongside of determined values in table 4.7. r(H···N) and $\angle$(NH···N) were not included in the fit, and were instead determined by the geometry produced from fitting the other structural parameters.

The experimental results agree generally well with the calculated results, as shown in figure 4.8 where the calculated geometry is overlaid with the geometry obtained by fitting to the experimental data. The intermolecular $\angle$(NH···N) implied by the r_0 geometry, 169.3°, differs from that given by the calculated r_e geometry, 179.6°. The intermolecular hydrogen bond interaction, r(H···N), also differs by 0.013 Å from the r_0 to r_e geometry. This is likely the result of some of the assumptions made in fitting the r_0 geometry of the complex, such as starting with the r_0 geometry of the imidazole monomers.
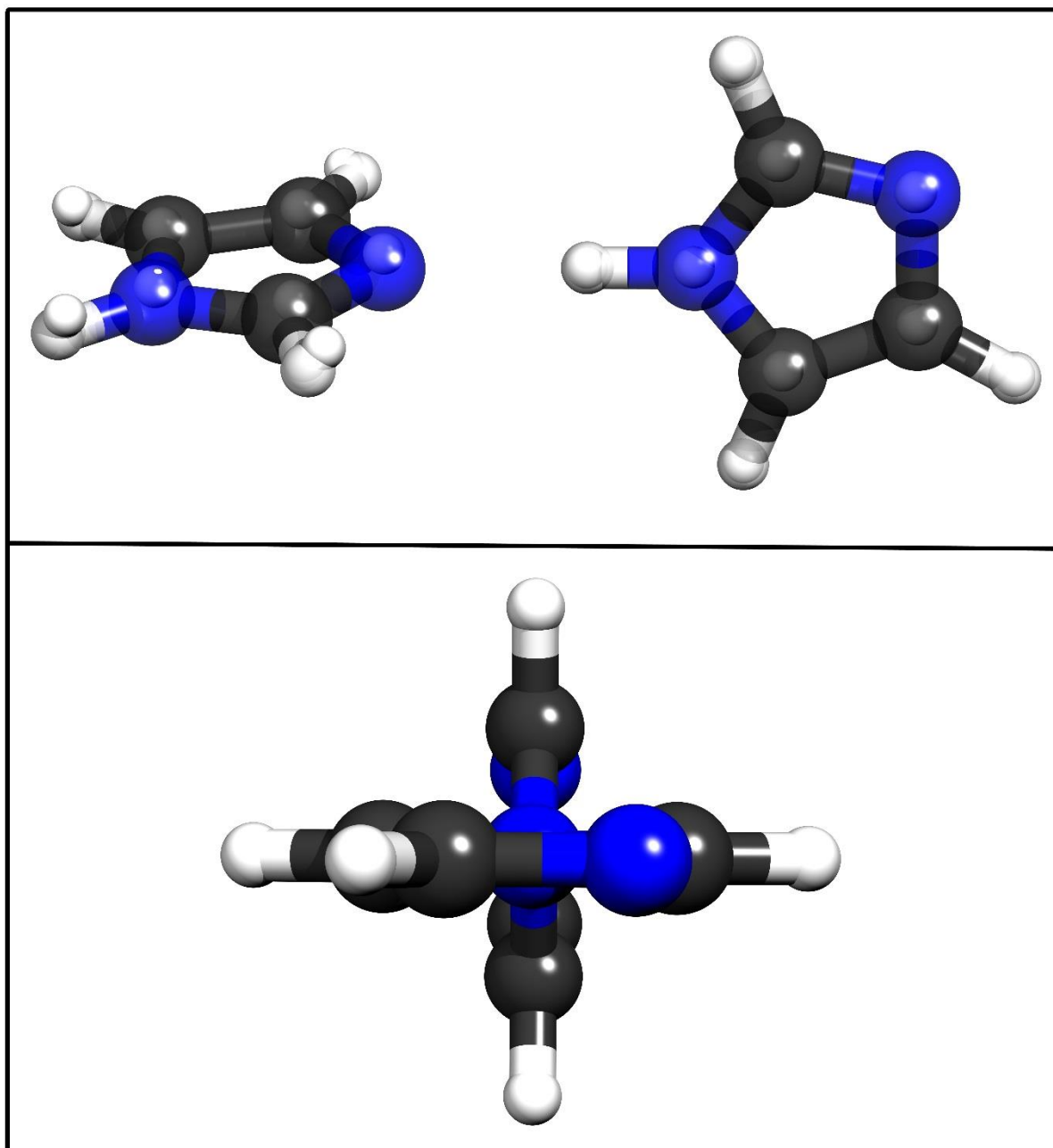
Figure 4.8 (Top): The geometry of the lowest energy conformer of the imidazole dimer, with the experimentally determined r_0 geometry (small spheres) overlaid onto the calculated geometry (large spheres), at the CCSD(T)(F12*)/cc-pVDZ-F12 level of theory. (Bottom): The geometry of the dimer from a view coaxial to the intermolecular hydrogen bond.

4.6 Conclusions

The lowest energy conformer of a complex consisting of two imidazole monomer units was observed using microwave spectroscopy in the 6.5 – 18 GHz range. No other conformers were detected, however the spectrum shows that imidazole undergoes significant fragmentation during the experiment. This work has shown that an intermolecular hydrogen bonding interaction is necessary to stabilise the formation of a dimer between two imidazole monomer units. The experimentally determined r_0 structure is in good agreement with calculated results and is similar to the structure presented by Choi.[89-90] This work has also shown that imidazole undergoes significant fragmentation under the experimental conditions and forms multiple CN containing species.

5. The hydrogen bonded complex of urea – isocyanic acid

5.1 Introduction

Denaturation of proteins is often induced to study the properties of their primary structure and assess their stability.[102-103] Denaturation disrupts the secondary structure of proteins, such as the α-helices and β-sheets, typically by affecting the network of hydrogen bonding interactions between groups such as the amide groups of peptides. The denaturation process keeps the primary structure of the protein intact, which consists of the sequence of amino acids. Various chemicals have been used as denaturants for this purpose, including alcohols.[104] Urea has historically seen wide use[105-107] as a protein denaturant, when in aqueous solution.

The exact properties of urea that are responsible for its efficacy in denaturation are not fully known, with many computational studies[108-111] reported exploring this subject. One proposed model, suggests that urea directly binds to proteins and competes with the existing intermolecular interactions between the amino acids of the protein itself. Another approach suggests that urea interferes with the solvation surrounding the protein, inducing denaturation. Both theories suggest that its ability to form multiple intermolecular interactions, such as hydrogen bonding is an important factor for its activity as a denaturant.

Urea has multiple sites that can form hydrogen bonding interactions. Each N-H could potentially act as a hydrogen bond donor and the oxygen atom of the carbonyl group could act as hydrogen bond acceptor. This is evidenced by the crystal structure of urea[112] which is shown in figure 5.1. Each urea forms up to six hydrogen bonding interactions with four other urea molecules, forming interactions as a donor and acceptor. Figure 5.2 shows another isomorph of urea which is observed when the crystal is exposed to high pressure, 0.5 GPa. This arrangement features a lesser degree of intermolecular interactions than the more stable isomorph, but still features multiple hydrogen bonds to each urea unit.
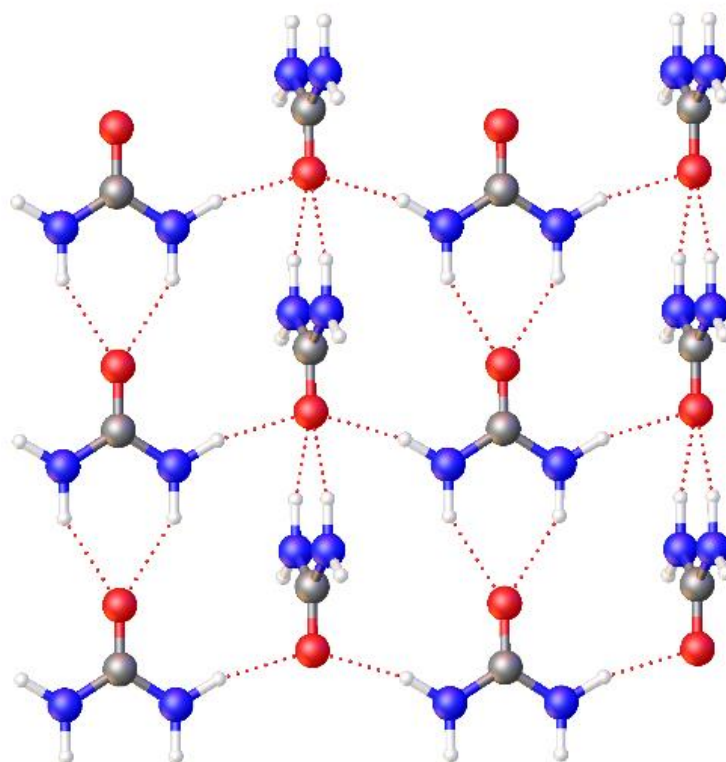
Figure 5.1 The crystal structure of the most stable isomorph of urea under standard conditions.[112] Hydrogen bonding interactions are indicated with dotted lines.
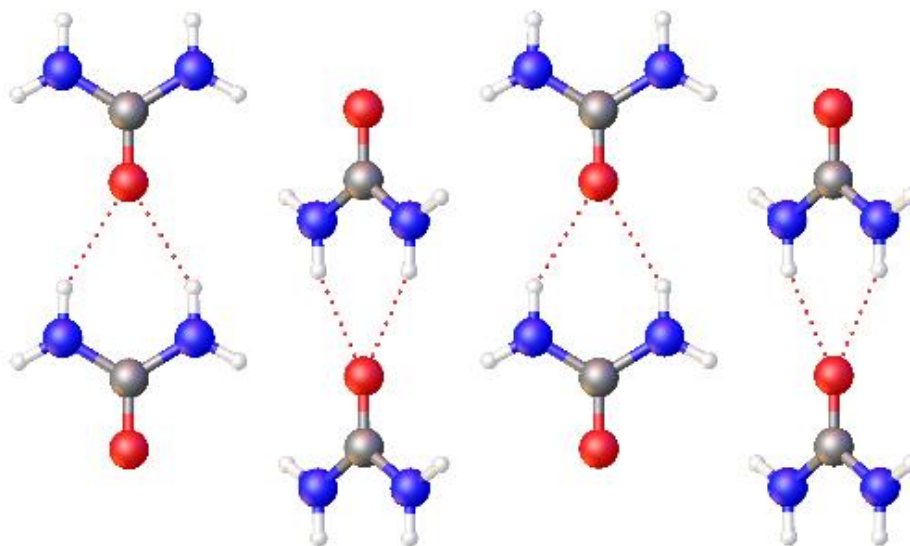
Figure 5.2 The isomorph observed when exposing crystalline urea to a high pressure (0.5 GPa).[113]

The versatility of urea is evidenced by its ability to form co-crystals with a wide range of compounds, from alcohols[114], to ethers[115], hydrocarbons and carboxylic

acids.[116] It is widely regarded as a useful agent for the isolation of crystalline solids that would otherwise be hard to crystallise, for example, long chain hydrocarbons.[117] The hydrogen bonding interactions of urea are centred on the carboxyl and amine groups, which can act as hydrogen bond acceptors and donors respectively. Urea is one of the smallest amides, and as such can be seen as a simple prototype model for understanding the hydrogen bonding interactions of peptides. This chapter aims to explore these interactions of urea, by examining the structure of a complex formed between urea and isocyanic acid in the gas phase.

5.2 Experimental details

Urea (Sigma-Aldrich, ≤99% purity) was used in the experiments described in this chapter, without further purification. Copper powder was also used throughout this work as discussed in section 3.5.2 in further detail. Target rods were created by grinding and mixing powdered samples of urea and copper in a 1:1 molar ratio and then compressing the mixture using a table top press and die (Specac). A variety of synthetically enriched isotopologues of urea were used during these experiments. To observe mixed species of $(H_2N)_2CO\cdots HNCO$, such as $(H_2N)_2^{13}CO\cdots HN^{12}CO$ and $(H_2N)_2^{12}CO\cdots HN^{13}CO$, equal quantities of the normal and isotopically enriched urea were used such that the overall molar ratio of the rod was 2:1:1 of copper to normal urea to an isotopologue of urea. $(H_2N)_2^{13}CO$ (Sigma-Aldrich, 99% ^{13}C, 99% purity), $(H_2^{15}N)_2CO$ (Sigma-Aldrich, 98% ^{15}N, 99% purity) and $(D_2N)_2CO$ (Sigma-Aldrich, 98% D, 99% purity) were all available commercially. $(H_2N)_2C^{18}O$ was synthesised by Luke Lewis-Borrell and Bernard Golding of Newcastle University, using $H_2^{18}O$. Only small amounts of some of the isotopologues were available due to their high cost, as a result smaller (5 mm) rods were used to minimise sample consumption.

5.3 Spectral analysis and calculations

The spectra in this chapter were recorded using a CP-FTMW spectrometer which is described in greater detail in section 3, in the range of 6.5 – 18.5 GHz. The full spectrum is shown in figure 5.3, where the most intense transitions were readily assigned to the previously reported monomer of urea.[118] Other signals due to other known species were observed. These included CH_3CN, HC_3N, H_2CO and NH_3 [93, 119-120] which presumably formed as a result of fragmentation of urea due to laser ablation.

A group of transitions which were unable to be assigned to any previously reported species were assigned to the Hamiltonian of a near-prolate asymmetric rotor, applying Watson's *S* reduction[67] and using PGOPHER.[78] Only *a*-type transitions for this species were observed. A smaller region of the spectrum showing two $J' \rightarrow J''$ transitions of this species is shown in figure 5.4.
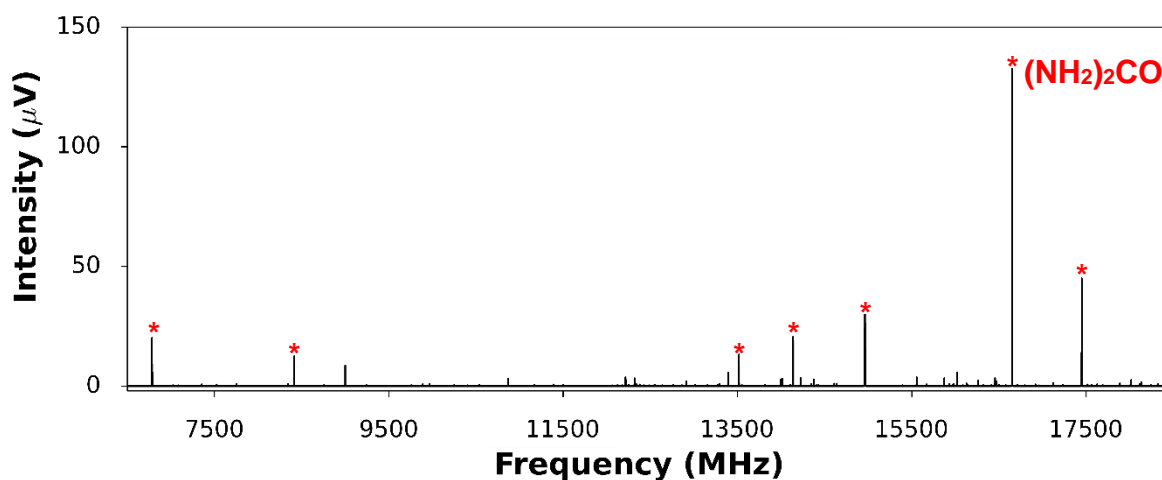
Figure 5.3 The broadband spectrum measured with ablation of a 1:1 copper and urea rod in the presence argon held at a stagnation pressure of 6 bar. The spectrum was obtained after adding 3.9 M FIDs in the time domain. Lines indicated with an asterisk are due to urea.
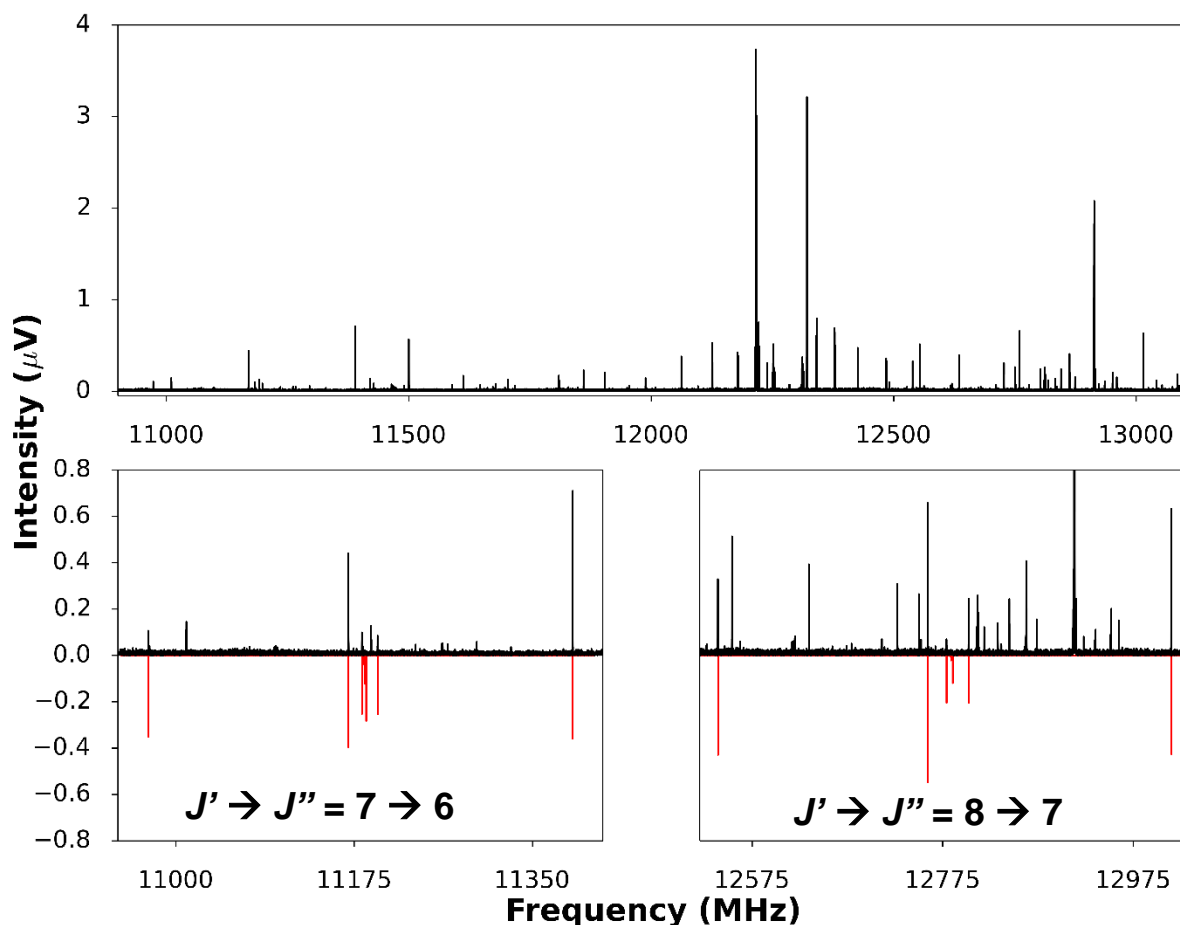
Figure 5.4 (Top): A section of the spectrum shown in Figure 5.2, from the range 10.9 – 13.1 GHz. (Left): An expanded region showing the $J' \rightarrow J'' = 7 \rightarrow 6$ transitions of the fitted species, with the experimental spectrum in black and the simulation shown in red. (Bottom right): An expanded region showing the $J' \rightarrow J'' = 8 \rightarrow 7$ transitions of the fitted species.

The identity of the fitted species was initially unknown. The experiment originally aimed to observe a dimer of urea, with the lowest energy structures presenting a bifurcated hydrogen bonding geometry, as shown in figure 5.5. Comparing the rotational constants shown in table 5.1 for the structures presented in figure 5.5, it is evident that the identity of the fitted species is not similar to either calculated structure.

	Exp.	D1	D2
A / MHz	10383.2(11)	5229	4615
B / MHz	828.6929(14)	655.878	862.853
C / MHz	769.1716(16)	582.788	805.759

Table 5.1 The rotational constants for the fitted species and potential conformers of a dimer of urea.

D1   **D2**
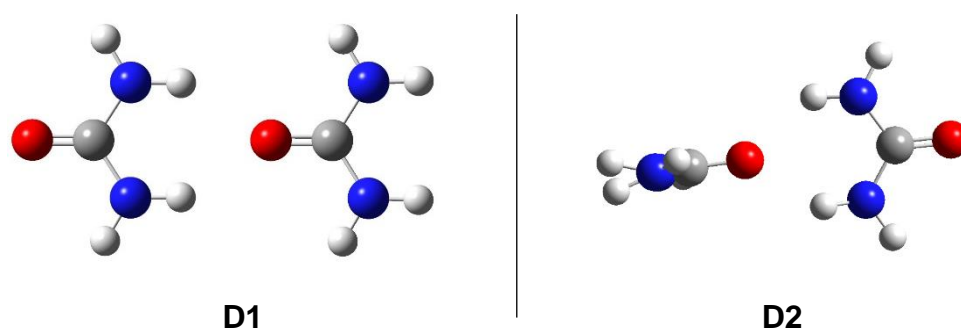
Figure 5.5 The geometries of two conformers of the urea dimer, calculated at the MP2/6-311++G(d,p) level of theory.

Initially multiple possible molecules were explored, prompted by the presence of a large number of fragments of imidazole which were observed during experiments detailed in section 4. Fragments such as CH_3CN, HC_3N, H_2CO and NH_3 were observed. Urea is known to thermally decompose[121] to form ammonia and isocyanic acid. Complexes involving urea and fragmentation products such as isocyanic acid were therefore amongst the first complexes to be investigated by calculations.

The calculated rotational constants of the lowest energy conformer of a complex between urea and isocyanic acid is shown in table 5.2 alongside the constants obtained from the fit of experimental data. David Tew of Bristol University performed the CC calculations shown in table 5.2 and the conformational survey, at the MP2/aug-cc-pVTZ level of theory, which is shown in figure 5.6.

	Exp.	CCSD(T)/AVTZ $(H_2N)_2CO\cdots HNCO$
A / MHz	10383.2(11)	10340
B / MHz	828.6929(14)	835.6
C / MHz	769.1716(16)	775.0
D_{JK} / kHz	2.702(56)	-
D_J / kHz	0.1772(24)	-
d_1 / Hz	-14.7(37)	-
N	24	-
$\sigma_{r.m.s}$ / kHz	10.3	-
Δo / u Å^2	-1.480	-1.584

Table 5.2 Rotational constants fitted for the unknown species compared to the calculated geometry of the lowest energy conformer of a complex between urea and isocyanic acid, $(H_2N)_2CO\cdots HNCO$.
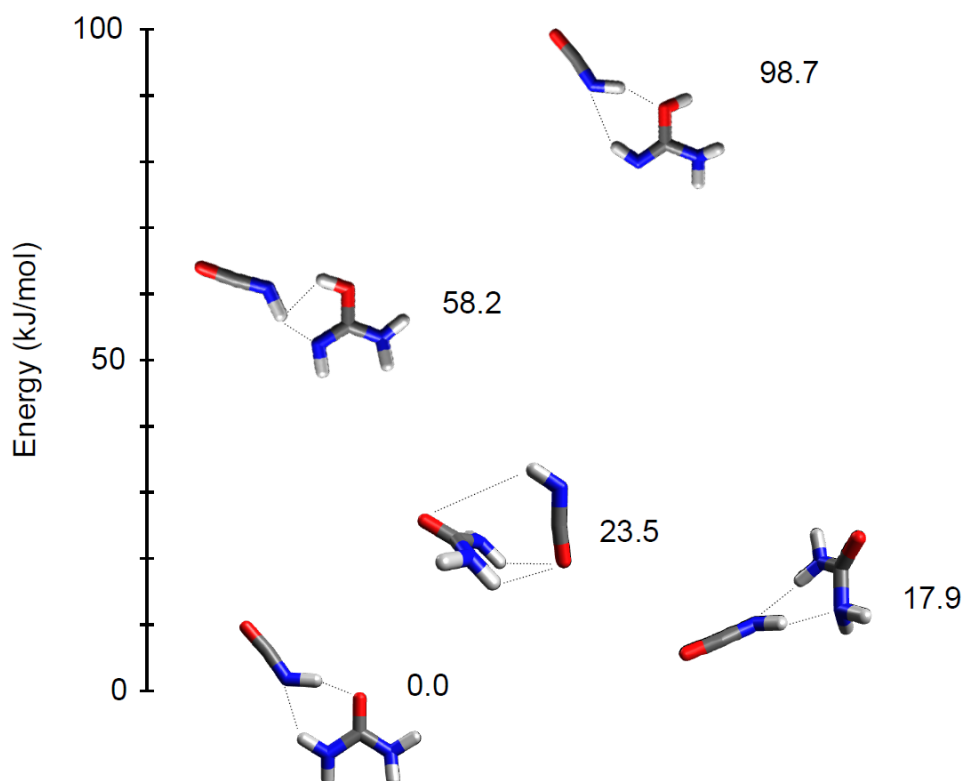
Figure 5.6 The calculated relative energies of different conformers of $(NH_2)_2CO\cdots HNCO$ and similar structures, calculated at the MP2/aug-cc-pVTZ level of theory by David Tew. Hydrogen bonded interactions are represented by dotted lines.
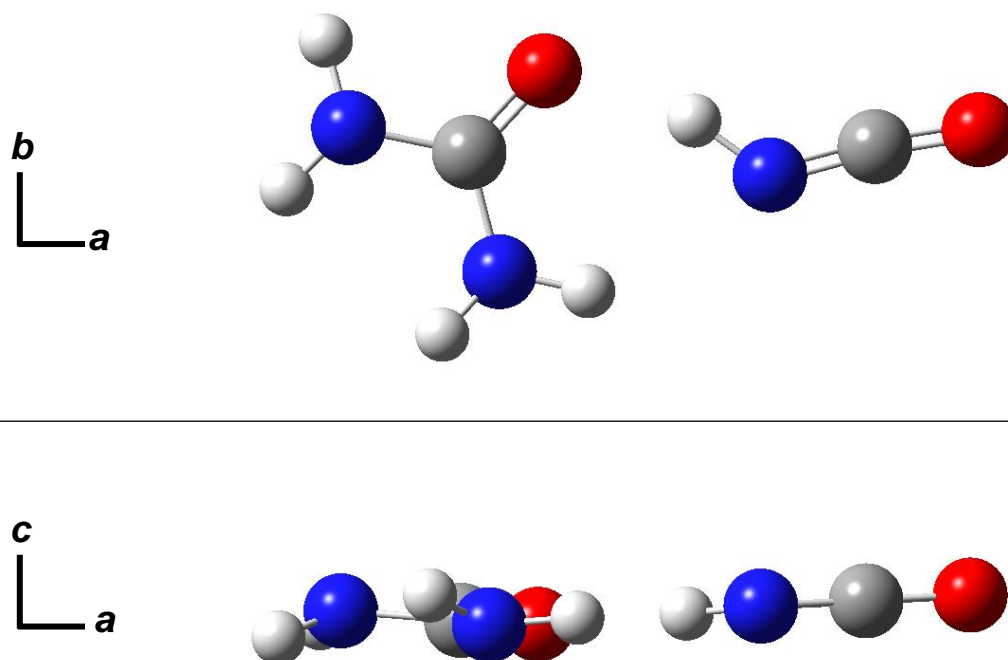
Figure 5.7 The calculated lowest energy structure of $(NH_2)_2CO \cdots HNCO$, at the MP2/aug-cc-pVTZ level of theory, with the inertial axes displayed.

The calculated results agree fairly well with the experimental constants. The calculated dipole moments were μ_a= 5.84 D, μ_b= 1.05 D and μ_c= 0.01 D, which agrees with the observed spectrum, where only *a*-type transitions were observed. The inertia defect is small and negative suggesting the molecule is not planar, which is in agreement with the calculated geometry shown in figure 5.7. In this geometry the N-H group of the isocyanic acid unit forms two hydrogen bonding interactions, one as a donor and one as an acceptor.

Further isotopic experiments were performed to confirm the identity of the fitted species. In total 12 isotopologues were measured, which are shown in tables 5.3 – 5.6. Each experiment revealed more information about the molecule, for example, three isotopologues containing ^{13}C were measured, showing the molecule contained two distinct carbon atoms. Similar deductions were made, such as the presence of two distinct oxygen atoms, at least two different nitrogen atoms, and two inequivalent hydrogen atoms in the complex.

The rotational constants for the parent species were scaled to predict the isotopologues and these values matched with the corresponding isotopologues of $(H_2N)_2CO\cdots HNCO$, providing further evidence of the identity of the fitted species is the lowest energy conformer of $(H_2N)_2CO\cdots HNCO$. Only a single conformer was detected, this was to be expected given the next lowest energy conformer is 17.9 kJ/mol higher in energy.

	$(H_2N)_2{}^{13}CO\cdots HN^{13}CO$	$(H_2N)_2{}^{13}CO\cdots HN^{12}CO$	$(H_2N)_2{}^{12}CO\cdots HN^{13}CO$
A_0 / MHz	10385.6(17)	10383(11)	10379.5(65)
B_0 / MHz	814.8093(12)	824.1557(31)	819.36788(341)
C_0 / MHz	757.1957(13)	765.2617(32)	761.12894(458)
D_{JK} / kHz	2.27(15)	2.75(132)	2.55(70)
D_J / kHz	0.1822(23)	0.1769(92)	0.1695(76)
d_1 / Hz	-15.1(28)	-13.7(74)	-18.5(100)
N	20	13	13
$\sigma_{r.m.s}$ / kHz	8.7	19.2	16.1

Table 5.3 Rotational constants determined for ^{13}C containing isotopologues of $(H_2N)_2CO\cdots HNCO$.

	$(H_2{}^{15}N)_2CO\cdots H^{15}NCO$	$(H_2{}^{15}N)_2CO\cdots H^{14}NCO$	$(H_2{}^{14}N)_2CO\cdots H^{15}NCO$
A_0 / MHz	10022.84(67)	10032.8(23)	10355.9(41)
B_0 / MHz	809.60067(48)	812.5968(15)	825.75939(245)
C_0 / MHz	750.76973(43)	753.39382(191)	766.5830(20)
D_{JK} / kHz	2.505(53)	2.69(15)	3.53(40)
D_J / kHz	0.17654(90)	0.1766(32)	0.1783(43)
d_1 / Hz	-7.4(11)	-8.5(41)	-20.4(52)
N	27	17	16
$\sigma_{r.m.s}$ / kHz	4.9	10.4	13.1

Table 5.4 Rotational constants determined for ^{15}N containing isotopologues of $(H_2N)_2CO\cdots HNCO$.

	$(H_2N)_2C^{18}O \cdots HNC^{18}O$	$(H_2N)_2C^{18}O \cdots HNC^{16}O$	$(H_2N)_2C^{16}O \cdots HNC^{18}O$
A_0 / MHz	9999.3(16)	10012.2(18)	10369.1(17)
B_0 / MHz	788.9340(20)	826.04043(81)	791.71554(57)
C_0 / MHz	732.8392(16)	764.77642(70)	737.18288(76)
D_{JK} / kHz	2.36(17)	1.86(19)	2.53(16)
D_J / kHz	0.1628(32)	0.1875(38)	0.1592(27)
d_1 / Hz	-15.7(42)	-21.5(63)	-20.4(47)
N	21	13	12
$\sigma_{r.m.s}$ / kHz	13.3	9.6	9.1

Table 5.5 Rotational constants determined for ^{18}O containing isotopologues of $(H_2N)_2CO \cdots HNCO$.

	$(D_2N)_2CO \cdots DNCO$	$(D_2N)_2CO \cdots HNCO$	$(H_2N)_2CO \cdots DNCO$
A_0 / MHz	8883.72(97)	8917.4(15)	10345.2(49)
B_0 / MHz	788.9446(15)	789.7975(22)	827.9495(26)
C_0 / MHz	726.5871(16)	727.5170(22)	768.32485(323)
D_{JK} / kHz	2.63(15)	4.49(25)	8.9(48)
D_J / kHz	0.1547(25)	0.1527(35)	0.1860(54)
d_1 / Hz	-14.2(36)	-21.3(49)	-10.9(69)
N	27	18	15
$\sigma_{r.m.s}$ / kHz	13.6	16.4	15.7

Table 5.6 Rotational constants determined for deuterium containing isotopologues of $(H_2N)_2CO \cdots HNCO$.

5.4 Structural analysis

The r_s method of Kraitchman[76], described in further detail in section 2.3.3, was used alongside r_0, also described in section 2.3.2, to determine structural parameters of the $(H_2N)_2CO\cdots HNCO$ complex. The internal parameters of urea and isocyanic acid were fixed to the monomer geometries when fitting the r_0 geometry of the complex. As data for isotopic substitution at every atom position is not available, particularly selective substitution of the hydrogen atoms in urea, the hydrogen positions and angles in the urea unit were fixed to that of the r_0 of the urea monomer when performing the r_0 fit of the complex. Such assumptions may be the most significant source of error and disagreement between structural fits from experimental data in comparison to calculations.

Various parameters are shown in table 5.7 alongside calculated results. Most parameters determined by r_s and r_0 methods agree fairly well, with some slight disagreement in parameters such as the angles $\angle(N_IH_I\cdots O_U)$ and $\angle(C_UO_U\cdots H_I)$, where subscripts I and U refer to atoms that are part of isocyanic acid and urea respectively. The extent to which the r_s and r_e geometries agree is shown in figure 5.8. The r_s and r_e geometries are generally in fair agreement, with the r_e geometry generally underestimating certain parameters such as the hydrogen-bond distance $r(O_U\cdots H_I)$. Table 5.8 shows the coordinates of atoms as determined by r_s and r_0 methods, alongside the calculated, r_e, coordinates. The position of hydrogen atoms in the complex are not precisely determined, as evidenced by slight inconsistencies in the determined $r(O_U\cdots H_I)$ and the coordinates of H_I. Overall the coordinates of each heavy atom are largely in agreement, comparing r_s, r_e, and r_0 structures.

	r_s	r_0	r_e (CCSD(T)/AVTZ)
$r(O_U \cdots H_I)$ / Å	1.820(6)	1.866(11)	1.773
$r(N_I \cdots O_U)$ / Å	2.762(8)	2.809(9)[a]	2.790
$r(N_I \cdots H_U)$ / Å	-	2.261(13)[a]	2.306
$\angle(N_I H_I \cdots O_U)$ / °	151.2(23)	156.8(6)	160.4
$\angle(C_U O_U \cdots H_I)$ / °	113.9(27)	112.5(6)	112.6
$\angle(N_U H_U \cdots N_I)$ / °	-	138.4(78)[b]	137.2

Table 5.7 Fitted values of structural parameters presented with calculated results. Subscript I denotes atoms part of isocyanic acid whereas subscript U denotes atoms that are part of urea. [a] Deduced from other fitted parameters.
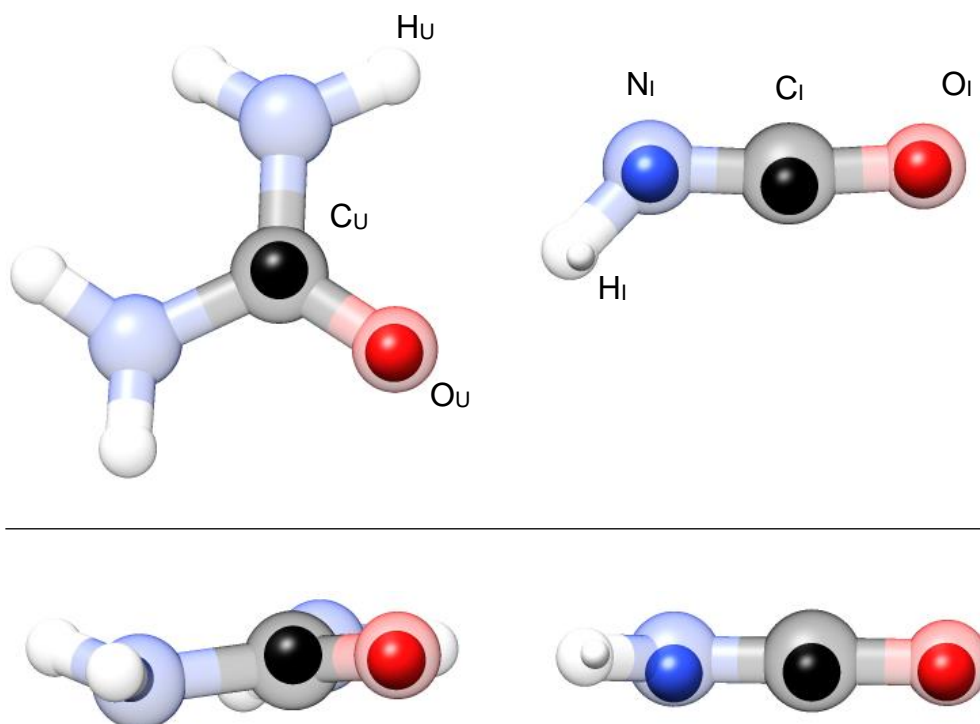
Figure 5.8 The geometry of $(H_2N)_2CO \cdots HNCO$, with the r_s geometry represented by small spheres and the calculated r_e geometry represented by large spheres.

Atom	a / Å	b / Å	c / Å	Method
	0.9976(24)	−0.9613(25)	0.000(40)[a]	r_s
O_U	1.0026	−0.9715	0.1058	r_e
	1.033(8)	−0.991(8)	0.10644(1)	r_0
	1.8395(21)	0.00(9)[a]	0.00(6)[a]	r_s
C_U	1.8319	−0.072	0.0225	r_e
	1.8419(6)	−0.080(1)	0.0221(2)	r_0
	−0.7387(49)	−0.4220(85)	0.072(50)	r_s
H_I	−0.6645	−0.3714	0.0332	r_e
	−0.732(2)	−0.387(9)	0.033(1)	r_0
	−1.4762(27)	0.259(15)	−0.131(30)	r_s
N_I	−1.4582	0.280	−0.0350	r_e
	−1.469(1)	0.278(6)	−0.0351(4)	r_0
	−2.6410(14)	−0.087(44)	−0.109(35)	r_s
C_I	−2.6353	−0.0054	−0.0207	r_e
	−2.6469(1)	−0.0132(9)	−0.0207(2)	r_0
	−3.80462(62)	−0.158(15)	−0.111(21)	r_s
O_I	−3.7958	−0.151	−0.0195	r_e
	−3.8058(6)	−0.146(4)	−0.0209(3)	r_0

Table 5.8 Values of atomic coordinates determined by the three noted methods. Atoms in the isocyanic acid moiety of the complex are tagged with I whereas atoms in the urea moiety are tagged with U. [a] Imaginary coordinates were obtained and therefore these values are fixed to zero.

The r_0 geometry, as shown in figure 5.9, shows that the complex exhibits a pair of hydrogen bonds between isocyanic acid and urea. The amide group of urea forms two hydrogen bonds to isocyanic acid, one as a donor and one as an acceptor. $r_0(O_U\cdots H_I)$ = 1.8661(11) Å is significantly shorter than $r_0(N_I\cdots H_U)$ = 2.261(13) Å, suggesting the first hydrogen bond is stronger. The dissociation energy of $(H_2N)_2CO\cdots HNCO$ was calculated with CCSD(T)(F12*)/aug-cc-pVTZ level of theory to be ~41 kJ/mol with counter poise correction, by David Tew. The value of the average calculated energy of hydrogen bonding interactions between urea and different peptide backbones has been reported as ~18 – 26 kJ/mol.[122] Comparing this to the dissociation energy suggests that the $(H_2N)_2CO\cdots HNCO$ contains two distinct hydrogen bonding interactions.
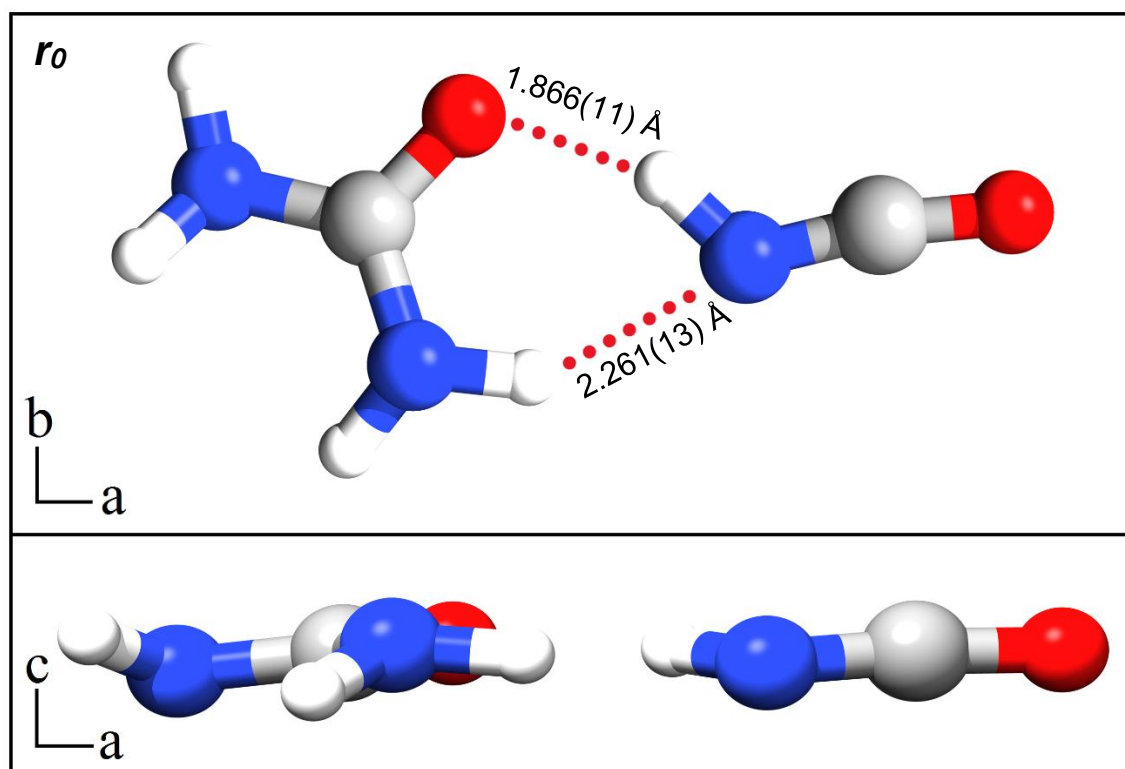
Figure 5.9 (Top): The r_0 structure of $(H_2N)_2CO\cdots HNCO$ with the inertial axes displayed. The two hydrogen bonding interactions are denoted by red dotted lines with their lengths labelled. (Bottom): The same structure as above from a different view.

5.5 Conclusions

A complex consisting of urea and isocyanic acid was observed using microwave spectroscopy in the 6.5 – 18.5 GHz range. The complex was shown to include two hydrogen-bonding interactions, with the N-H group of isocyanic acid acting as a hydrogen bond donor and acceptor. Various structural parameters were determined for the complex showing the length of the hydrogen bonding interaction between the hydrogen atom of isocyanic acid and the oxygen of urea to be 1.820(6) Å (r_s) and 1.866(11) Å (r_0) and the length of the hydrogen bonding interaction between the nitrogen atom of isocyanic acid and the hydrogen atom of urea to be 2.261(13) Å (r_0). The structure observed demonstrates the ability of urea to form multiple hydrogen bonding interactions. It has the capability of forming interactions as both a donor and an acceptor, even forming both simultaneously as shown by $(H_2N)_2CO^{..}HNCO$. This work could be further extended to attempt to form and examine complexes involving urea and multiple other molecules. For example, a trimer structure involving two isocyanic acid units and one urea would show the effect of more than two simultaneous hydrogen bonding interactions to urea.

Chapter 6. A complex of urea and imidazole

6.1 Introduction

As mentioned earlier in section 1.3, laser ablation is employed worldwide[123-124] as a means of generating species in the gas phase for study by high resolution spectroscopic techniques such as microwave spectroscopy. It has been used, in combination with molecular beams, to study molecules including organic monomers[125], metal containing species[126] and weakly bound complexes[127]. In particular laser ablation has been employed to study molecules that are difficult to generate in the gas phase, for example, due to a high melting point.

Alonso and co-workers[128] developed a laser ablation molecular beam Fourier-transform microwave spectrometer, and demonstrated its effectiveness in measuring the rotational spectrum of high melting point organic solids with the observation of molecules such as 1,3,5-trithiane[129], and the amino acids proline[130] and alanine[131] amongst others. With the advent of chirped-pulse techniques, developed by Pate and co-workers[22], a larger frequency range could be interrogated by microwave spectroscopy simultaneously and more efficiently. Several groups adopted the technique, in combination with laser ablation, to study biomolecules and the complexes they form. The structure and functionality of biological molecules continues to be a popular area of research amongst the scientific community. Bioactivity relies heavily on structure and to study the characteristics of, for example proteins, probing the structure of smaller prototypes, or molecules that possess similar active sites, can prove informative.

Typically laser ablation of biomolecules may result in fragmentation and unnecessary reaction products that would complicate rotational spectra. This chapter aims to highlight the utility of laser ablation to form weakly bound complexes and fragmentation products. This chapter also aims to build on previous work and characterise a complex involving both imidazole and urea, to further explore their capability to form weak stabilising intermolecular interactions.

6.2 Experimental details

Both imidazole (Sigma-Aldrich, 99% purity) and urea (Sigma-Aldrich, ≤99% purity) were used in the experiments in this chapter, without further purification. Rods were created by grinding and mixing powdered samples of copper, urea and imidazole in a 2:1:1 molar ratio and then compressing the mixture using a table top press to produce target rods with a diameter of 13 mm. A variety of synthetically enriched isotopologues of urea and imidazole were used during this experiments. $(H_2N)_2{}^{13}CO$ (Sigma-Aldrich, 99% ^{13}C, 99% purity), $(D_2N)_2CO$ (Sigma-Aldrich, 98% D, 99% purity) and Imidazole-d_4 (CDN Isotopes, 98% purity, 97% D) were used to measure isotopologues. Further details about the laser ablation and spectrometer setup are available in section 3.

6.3 Spectral analysis and identification

The spectrum was recorded in the range of 6.5 – 18.5 GHz. The full spectrum is shown in figure 6.1, where the most intense transitions were assigned to the previously reported monomers of urea[118] and imidazole[92]. The signal to noise ratio of both monomers of imidazole and urea, at 2.25 M FIDs, was sufficient enough to also observe the corresponding single ^{13}C isotopologues in the same experiment.
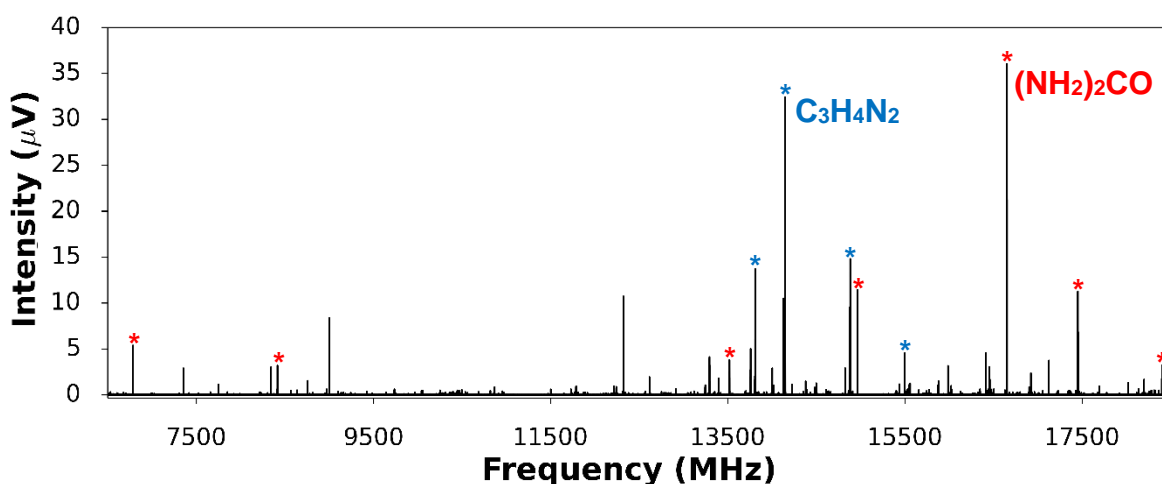
Figure 6.1 The full 6.5 – 18.5 GHz broadband rotational spectrum measured with laser ablation of a 2:1:1 copper to urea to imidazole rod with a pulsed gas sample consisting of argon held at a stagnation pressure of 6 bar (2.25 M FIDs). Transitions marked with a blue asterisk are due to $C_3N_2H_4$ and transitions marked with a red asterisk are due to $(NH_2)_2CO$.

As shown in the spectra discussed in sections 4 and 5, laser ablation is capable of producing a large amount of fragmentation products. Transitions due to previously reported molecules such as CH_3CN, CH_3CH_2CN, $HCCCN$, NH_2CH_2CN, HC_5N, HC_7N, CH_3C_3N, H_2CO and NH_3[93, 97-101, 119-120] amongst others were observed in the spectrum and were subtracted from the spectrum to aid in identification of other unassigned transitions. A number of transitions are left after the subtraction, some of which were unable to be assigned.

A set of regularly spaced transitions were identified and were fit to the S reduced[67] Hamiltonian of an asymmetric top using PGOPHER[78], with some of the lines shown in figure 6.2. These consisted of purely *a*-type transitions. The determined rotational constants, for the species herein referred to as C1, are shown in table 6.1. These transitions were not observed in the experiments detailed in section 4 and 5, suggesting C1 requires both urea and imidazole to be present in the target rod in order to be observed.
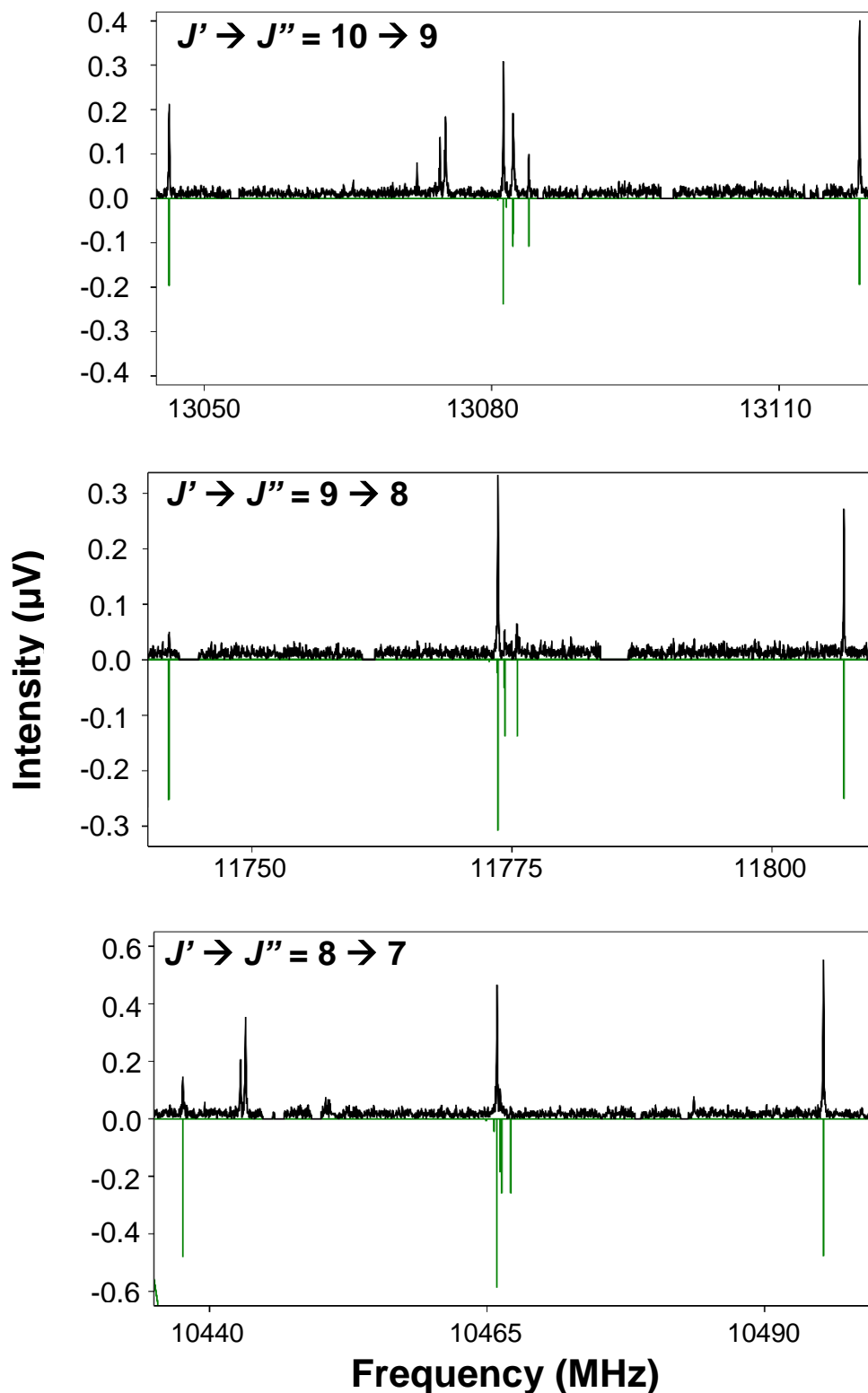
Figure 6.2 Expanded regions of the spectrum shown in figure 6.1, with known transitions subtracted from the spectrum (2.25 M FIDs). Various transitions of a previously unreported species are shown, referred to as C1. The simulated fit is shown in green and the experimental spectrum in black. $J' \rightarrow J'' = 10 \rightarrow 9$, (Top), $J' \rightarrow J'' = 9 \rightarrow$ 8, (middle), $J' \rightarrow J'' = 8 \rightarrow 7$, (bottom).

	C1
A_0 / MHz	4591.6(68)
B_0 / MHz	657.8294(11)
C_0 / MHz	650.6084(11)
D_{JK} / kHz	4.634(18)
D_J / kHz	0.3822(11)
d_1 / Hz	-17.9(18)
N	40
$\sigma_{r.m.s}$ / kHz	13.7

Table 6.1 Rotational constants determined for an unknown species C1.

Information regarding the identity of the species C1 can be gained by examining the rotational constants. The small B_0-C_0 indicates C1 is relatively heavy, suggesting it is possibly a complex containing more than one molecule. The large and negative inertial defect, Δo = -101.539 u Å^2, indicates C1 is not planar. If C1 is a complex, it likely includes any combination of the precursors such as urea, imidazole or argon, or any of the fragmentation products formed from the laser ablation. Transitions due to $(C_3H_4N_2)_2$ and $(NH_2)_2CO \cdots HNCO$ were also observed in the spectrum which prompted calculations to investigate other possible complexes that may have formed. The first candidate considered was a complex between urea and imidazole, given the high intensity of the respective monomer signals.

A conformational survey is necessary as multiple different conformations can be visualised using chemical intuition. An initial conformational survey was performed by Susana Blanco of the University of Vallodolid at the MP2/6-311++G(d,p) level of theory, which identified the lowest energy conformers. This survey informed later calculations which are discussed below.

Table 6.2 and figure 6.3 shows the results of calculations at the MP2/aug-cc-pVTZ level of theory for a few possible conformers of $(NH_2)_2CO{\cdots}C_3H_4N_2$, alongside the measured rotational constants of species C1. Conformers P1 and P2 have an almost perpendicular arrangement of monomers whereas conformers F1 and F2 have a flat arrangement of urea and imidazole. All of the conformers shown in figure 6.3 are relatively close in energy, with the highest, F2, being ~ 5.9 kJ mol^{-1} higher than the lowest energy conformer P1. Hydrogen bonding interactions feature in all potential conformers, with all forming at least one NH${\cdots}$N interaction.

Comparing the rotational constants show that conformer P1 most closely matches the rotational constants of C1. The dipole moments associated with P1 are in agreement with C1, as only *a*-type transitions were observed. The identity of the complex C1, is hence likely to be the lowest energy conformer, P1, of a $(NH_2)_2CO{\cdots}C_3H_4N_2$ complex.

	P1	F1	P2	F2	C1
A / MHz	4531.831	5025.136	4799.507	5067.033	4592.0(89)
B / MHz	680.1974	637.1220	621.9040	619.6746	657.8297(14)
C / MHz	673.0012	567.3246	683.8018	553.9948	650.6088(15)
μ_a / **D**	5.72	1.43	8.91	3.15	-
μ_b / **D**	1.90	0.04	0.63	2.24	-
μ_c / **D**	0.64	0.11	0.82	0.13	-
E / cm^{-1}	0.00	3.3	97.0	495.7	-

Table 6.2 Calculated rotational constants, dipole moments and energies of various conformers of $(NH_2)_2CO{\cdots}C_3H_4N_2$ at the MP2/aug-cc-pVTZ level of theory. Experimentally determined rotational constants for species C1 are also shown for comparison.

P1
0 cm^{-1}

P2
97.0 cm^{-1}

F1
3.3 cm^{-1}

F2
495.7 cm^{-1}
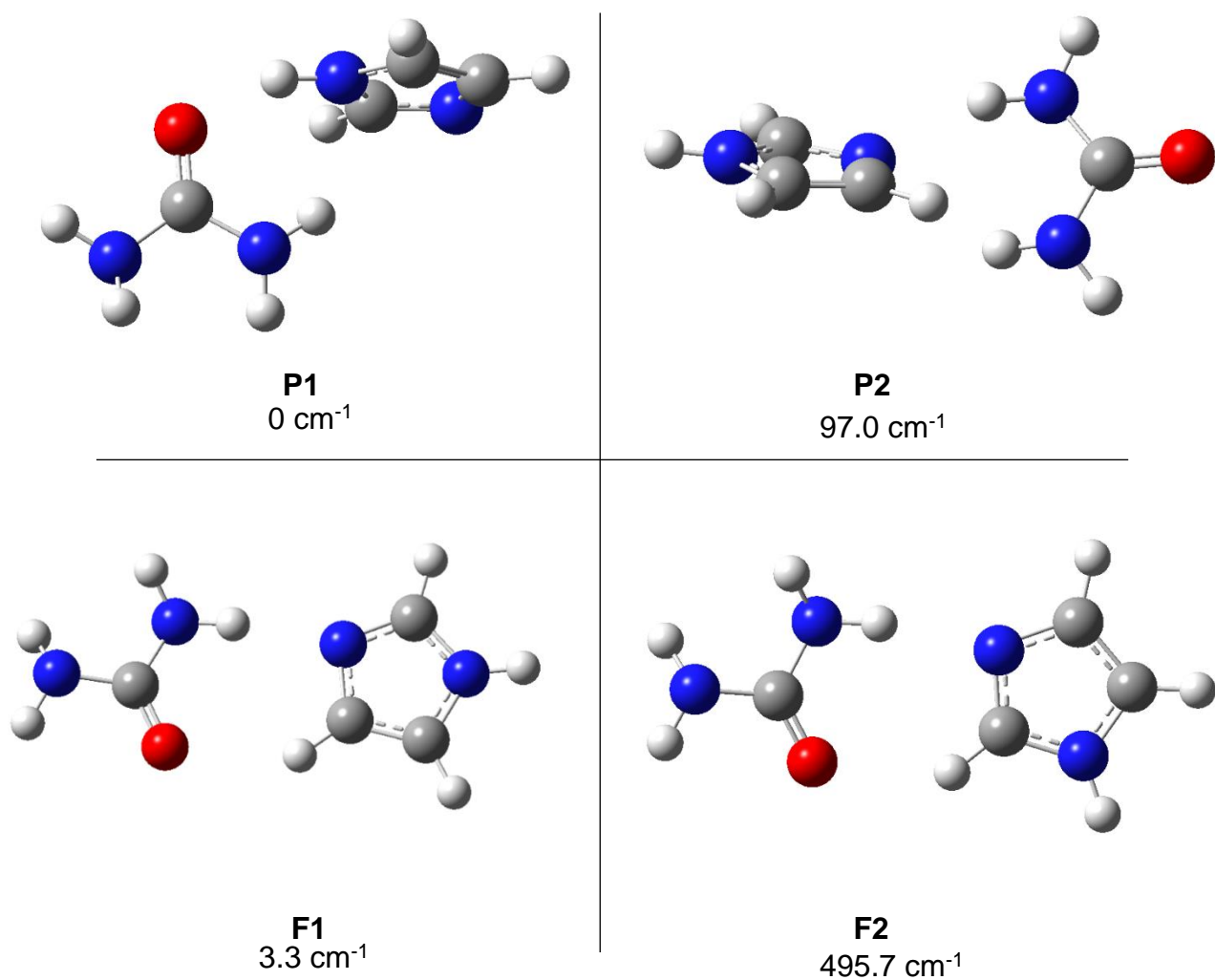
Figure 6.3 Calculated structures of the lowest energy conformers of $(NH_2)_2CO\cdots C_3H_4N_2$ at the MP2/aug-cc-pVTZ level of theory, also shown in table 6.2.

Experiments involving synthetically enriched urea and imidazole were carried out to confirm the identity of C1. $(H_2N)_2{}^{13}CO$ (Sigma-Aldrich, 99% ^{13}C, 99% purity), $(D_2N)_2CO$ (Sigma-Aldrich, 98% D, 99% purity) and $C_3D_4N_2$ (CDN Isotopes, 97% D, 98% purity) were used. Further isotopic substitution was not available due to the expense of certain synthetically enriched isotopologues of $(NH_2)_2CO$ and $C_3H_4N_2$. A set of transitions unable to be assigned to any previously reported species were found in each of these spectra, table 6.3 shows the determined rotational constants. The magnitude of the rotational constants of the isotopologues are similar to predictions for the corresponding isotopologues of structure P1, giving further evidence that the observed species is a conformer of $(NH_2)_2CO{\cdots}C_3H_4N_2$.

	$(D_2N)_2CO{\cdots}C_3H_4N_2$	$(D_2N)_2CO{\cdots}C_3D_4N_2$	$(H_2N)_2{}^{13}CO{\cdots}C_3H_4N_2$
A_0 / MHz	4264.9(37)	3999.3(80)	4592.2(94)
B_0 / MHz	626.7973(13)	605.8695(27)	653.2812(14)
C_0 / MHz	615.5264(14)	597.9251(23)	646.1610(14)
D_{JK} / kHz	4.48(12)	2.56(17)	4.524(45)
D_J / kHz	0.3437(16)	0.3248(20)	0.3757(15)
d_1 / Hz	-15.0(21)	-14.3(32)	-21.5(23)
N	23	17	44
$\sigma_{r.m.s}$ / kHz	13.3	16.7	18.4

Table 6.3 Rotational constants determined for three isotopologues of C1, identified as $(H_2N)_2CO{\cdots}C_3H_4N_2$.
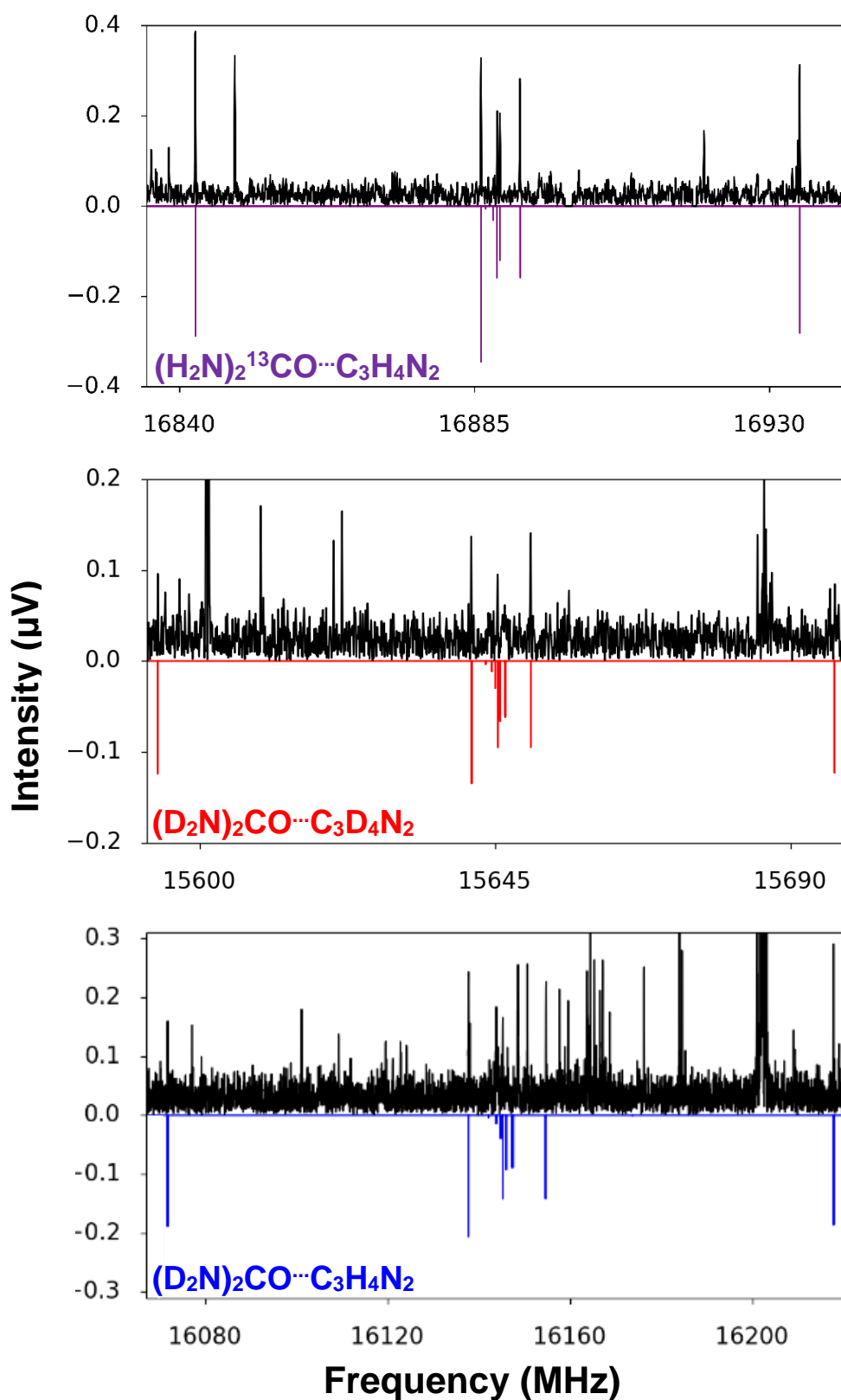
Figure 6.4 Small regions of the measured spectrum of laser ablation of rods containing various synthetically enriched isotopes of imidazole and urea. Showing $J' \rightarrow J'' = 13 \rightarrow 12$ for $(H_2N)_2{}^{13}CO\cdots C_3H_4N_2$ (top, 550k FIDs), $(D_2N)_2CO\cdots C_3D_4N_2$ (middle, 850k FIDs) and $(D_2N)_2CO\cdots C_3H_4N_2$ (bottom, 375k FIDs). Experimental spectra is shown in black and the simulations are labelled and shown as a negative.

Shown in figure 6.4 are the same $J' \rightarrow J'' = 13 \rightarrow 12$ transition for each isotopologue of the $(NH_2)_2CO \cdots C_3H_4N_2$ complex. Each transition is shifted to a lower frequency by the increase in mass, changing by ~ 750 MHz between $(H_2N)_2{}^{13}CO \cdots C_3H_4N_2$ and $(D_2N)_2CO \cdots C_3D_4N_2$. The spectra of $(ND_2)_2CO \cdots C_3D_4N_2$ and $(ND_2)_2CO \cdots C_3H_4N_2$ were particularly difficult to measure. As shown in figure 6.4 both were relatively weak in the spectra, which also contained numerous lines due to isotopologues of fragmentation products and other less abundant species.

Due to the lack of substitution at most atom positions only limited structural information can be obtained from the measured spectra. Single substitution at various atom positions would give the corresponding atomic coordinates of the substitution, r_s, structure. ^{13}C and ^{15}N containing isotopologues of imidazole were prohibitively expensive and the corresponding isotopologues of urea were also not available. The calculated geometry of $(H_2N)_2CO \cdots C_3H_4N_2$ is shown in figure 6.5. The complex features two intermolecular hydrogen bond interactions, between the oxygen atom of urea and the NH hydrogen atom of imidazole and between the NH hydrogen atom of urea and the pyrrolic nitrogen atom of imidazole. Similar arrangements are seen in other complexes such as the previously discussed $(NH_2)_2CO \cdots HNCO$ complex, section 5. Both involve simultaneous $O \cdots H$ and $N \cdots H$ interactions, across the amide group of $(NH_2)_2CO$. Various parameters of the calculated r_e geometry, including the length of the hydrogen bonding interactions, are shown in table 6.4.

	MP2/aug-cc-pVTZ r_e
$r(O \cdots H)$ / Å	1.835
$r(N \cdots H)$ / Å	2.393
$\angle(CO \cdots H)$ / °	114.4
$\angle(NH_{urea} \cdots N)$ / °	136.7

Table 6.4 Parameters of the calculated r_e structure of the $(H_2N)_2CO \cdots C_3H_4N_2$ complex.

$r_e(\text{O}\cdots\text{H}) = 1.835$ Å

$r_e(\text{N}\cdots\text{H}) = 2.393$ Å
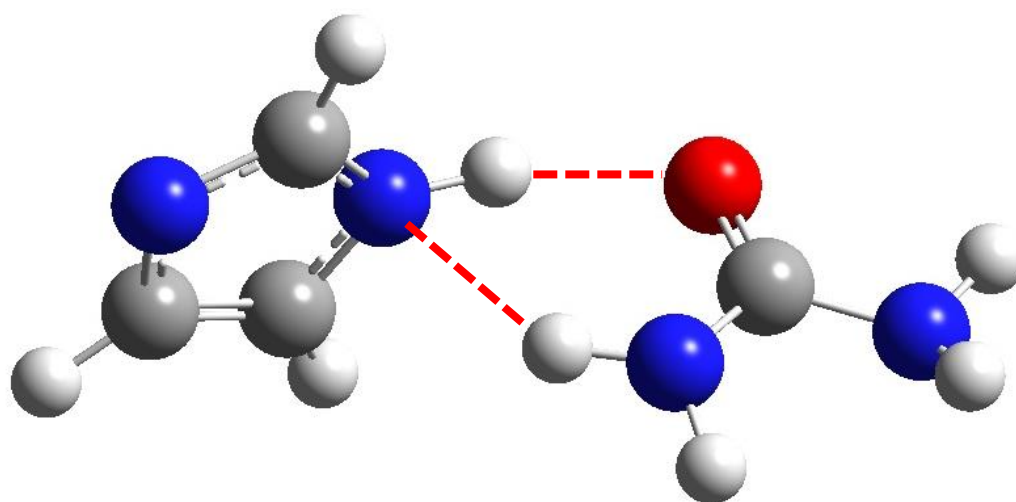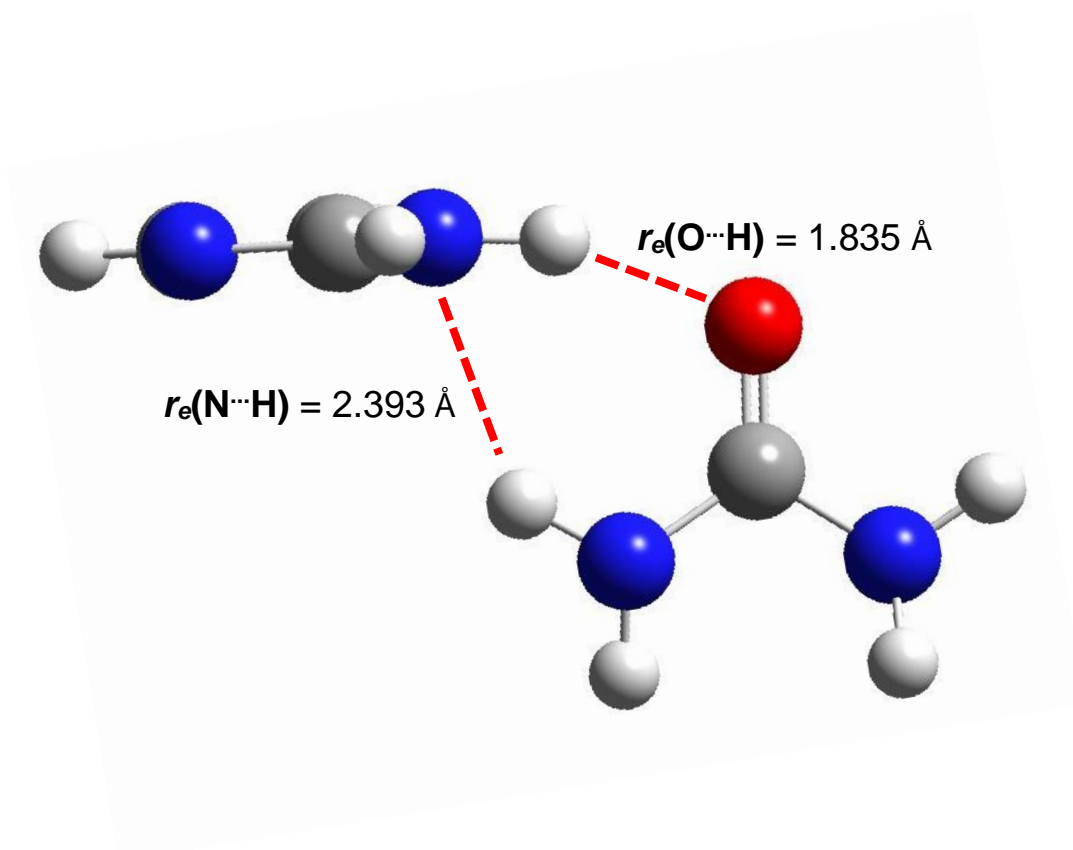
Figure 6.5 Calculated r_e geometry of the $(NH_2)_2CO\cdots C_3H_4N_2$ complex. The hydrogen bonding interactions are indicated with red dashed lines.

6.4 Conclusions

The spectrum of the laser ablation of imidazole and urea was measured for the first time in the 6.5 – 18.5 GHz range. It showed that both monomers undergo significant fragmentation and form a wide variety of fragmentation products and complexes under the current experimental conditions. Both $(C_3H_4N_2)_2$ and $(NH_2)_2CO\cdots HNCO$ were observed in the spectrum, alongside a species that was identified as a conformer of a complex of $(H_2N)_2CO\cdots C_3H_4N_2$. Calculations of the complex shows it exhibits two hydrogen bond interactions between the amide group of $(NH_2)_2CO$ and the N-H of $C_3H_4N_2$, $r_e(O\cdots H) = 1.835$ Å and $r_e(N\cdots H) = 2.393$ Å. Future experiments involving the measurement other isotopologues would provide more structural information about the complex. Given the relatively small energy difference between the lowest energy conformers, further experiments involving the use of different carrier gases such as neon or helium may be successful in observing different conformers of $(H_2N)_2CO\cdots C_3H_4N_2$.

Comparing this to the complex discussed in section 5, $(NH_2)_2CO\cdots HNCO$ to $(H_2N)_2CO\cdots C_3H_4N_2$, both form two hydrogen bonding interactions around the amide group of urea. $(H_2N)_2CO\cdots C_3H_4N_2$ features an almost perpendicular arrangement of monomers whereas $(NH_2)_2CO\cdots HNCO$ adopts a more planar structure, with HNCO forming two hydrogen bonds almost in the same plane as $(NH_2)_2CO$. The bond lengths and angles are comparable for the C=O$\cdots$H interaction in both complexes, differing in length by only ~ 0.03 Å and in <CO$\cdots$H by ~ 2°. Both also feature an NH$\cdots$N hydrogen bonding interaction, both of which are significantly larger (~ 0.4 – 0.5 Å) than the CO$\cdots$H interaction.

The hydrogen bonding interactions in $(H_2N)_2CO\cdots C_3H_4N_2$, are focused around the N-H group of imidazole in the observed complex. Performing experiments involving different molecules containing the same N-H hydrogen bond donor and acceptor character but with different structural and electronic features, e.g. pyrazole, would be of interest to see the effect on intermolecular interactions of any complexes formed.

7. The water – thiourea complex

7.1 Introduction

The versatility of water to form multiple different types of hydrogen bonding interactions is evidenced by the wide range of complexes that have been studied. Many examples of water containing complexes exist in the literature, where species have been studied using different spectroscopic techniques[132-134]. For example a variety of water-aromatic/heteroaromatic[135-136] complexes have been measured and characterised using microwave spectroscopy. Benzene-water[137] was one of the first of these systems to be studied and it was found that the water molecule lies above the π system with both hydrogen atoms pointing towards the ring. Studies probing the solvation of amino acids by characterising the complexes they form with water are also prevalent, being of great interest for the insight they can give to protein solvation.

One example which showcases the different types of hydrogen bonds water can form to organics is the formamide-water[138-139] complex. Multiple conformers were measured, where the water molecule acts as a hydrogen bond donor and acceptor and in a different experiment where two water molecules form a complex with formamide as shown in figure 7.1. One conformer exhibits a structure wherein the water forms two hydrogen bonding interactions to the CO and NH group of formamide. Such systems are of interest as prototypes for solvation of the peptide group of amino acids without the complexity added by the rest of the protein structure.
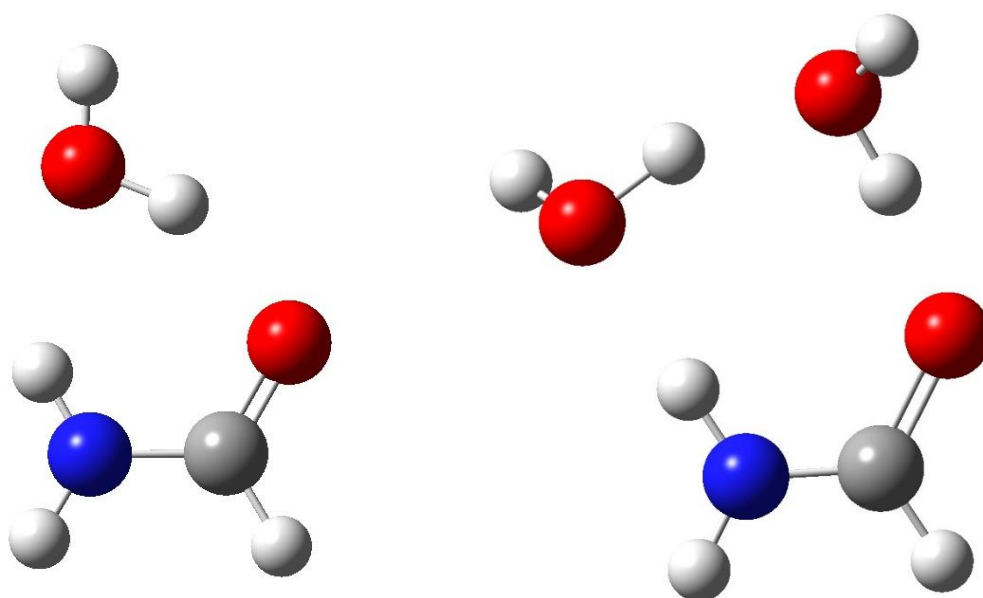
Figure 7.1 Structures of low energy conformers of formamide⋯H_2O and formamide⋯$(H_2O)_2$[138-139].

Thiourea has been shown to exhibit similar protein disrupting properties[140] as urea, and like urea, the mechanism by which it acts is still debated. Both molecules have the ability to form multiple hydrogen bonding interactions, thiourea is poorly soluble in water and as such is often used in tandem with urea to denature proteins.[141] The crystal structures of urea and thiourea provide an interesting contrast as depicted in figure 7.2.
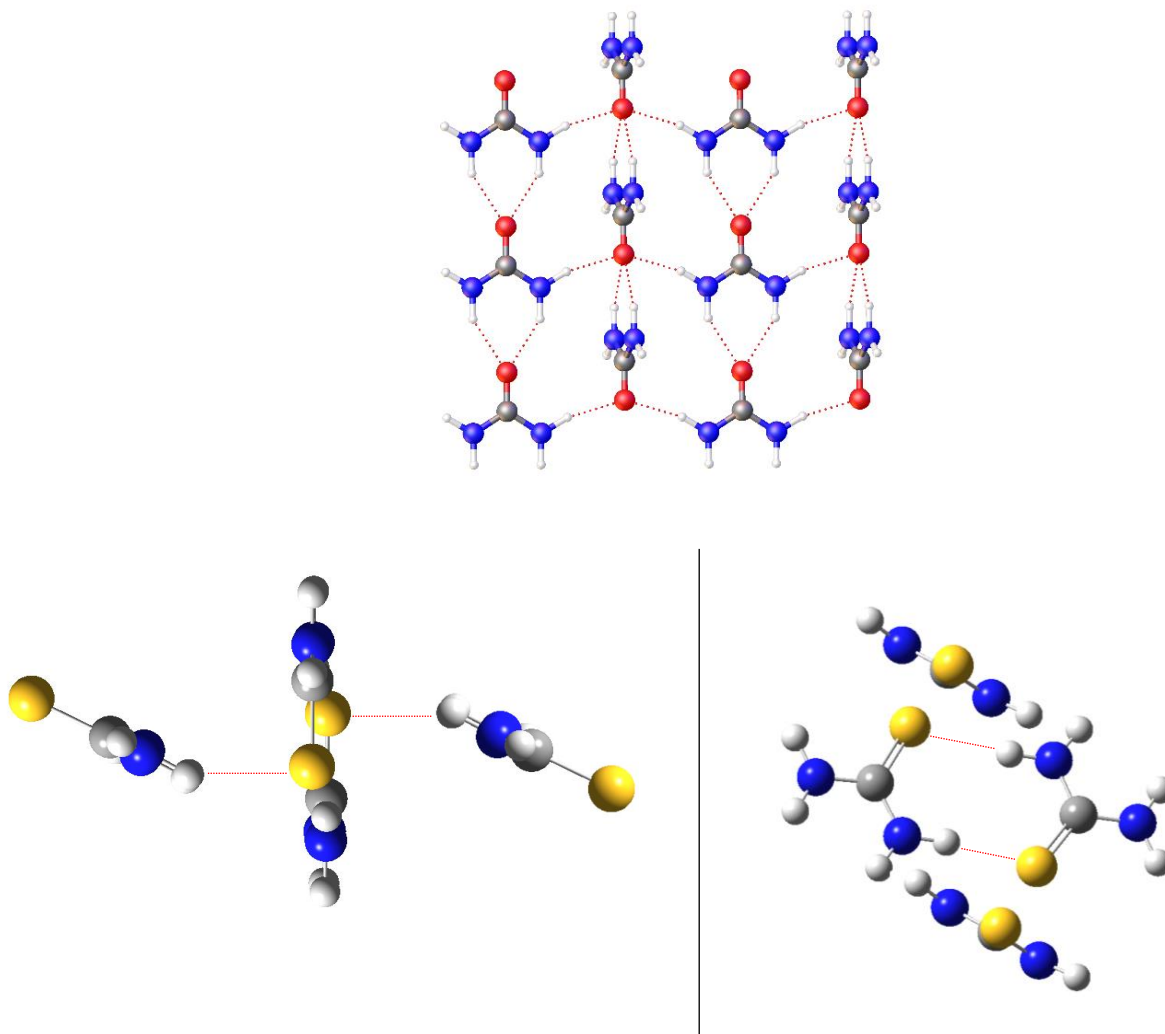
Figure 7.2 (Top): Crystal structure of urea[112], (Bottom): The unit cell of crystalline thiourea,[142] shown from different angles to illustrate the hydrogen bonding interactions shown as red lines.

Both predominately feature multiple hydrogen bonding interactions, with urea packing to maximise the amount of interactions involving oxygen, in a regular sheet-like manner. Thiourea forms multiple S⋯H hydrogen bonds and stacks in such a way that forms pseudocycle-like interactions with additional longer bifurcated NH_2⋯S interactions. The distances of the interactions are dramatically different when

comparing urea to thiourea. The hydrogen bond lengths in the crystal structure of urea are close to ~ 2 Å, whereas the lengths in thiourea are ~2.40 – 2.78 Å, with the bifurcated interaction in thiourea being the longest. These structures give insight into the hydrogen bonding properties of urea and thiourea. Despite being chemically and having similar structures in the gas phase, the effect of substituting oxygen for sulphur appears to have significant implications on the strength and character of hydrogen bonds formed.

The hydrogen bond forming capability of sulphur[143] has been explored extensively. In general it is observed that sulphur acts as a poor hydrogen bond acceptor but a good hydrogen bond donor. The dimer of H_2S is of interest as it is the most chemically simple molecule where sulphur acts as both a hydrogen bond donor and acceptor. Various computational studies have been performed, exploring the shape and strength of interaction, with some studies reporting the bond energy as low as ~4.6 kJ/mol.[144]. Recently the dimer was measured by microwave spectroscopy but is yet to be published.

The water dimer, $(H_2O)_2$, has been widely studied by various spectroscopic techniques. Comparing the MP2 calculated structure[145] of $(H_2S)_2$ to the experimental structure[146] of $(H_2O)_2$, figure 7.3, highlights the differences of hydrogen bonded oxygen and sulphur containing complexes. The main differences are the O-O or S-S distance, and the angle labelled as θ. The S-S distance is ~ 1 Å larger than the O-O distance, and also the S⋅⋅⋅H distance is over 0.5 Å longer than the corresponding O⋅⋅⋅H interaction. θ also differs significantly, with $\theta = 59.7°$ in $(H_2O)_2$ and $\theta = 88.7°$ in $(H_2S)_2$.

(H₂O)₂   **(H₂S)₂**
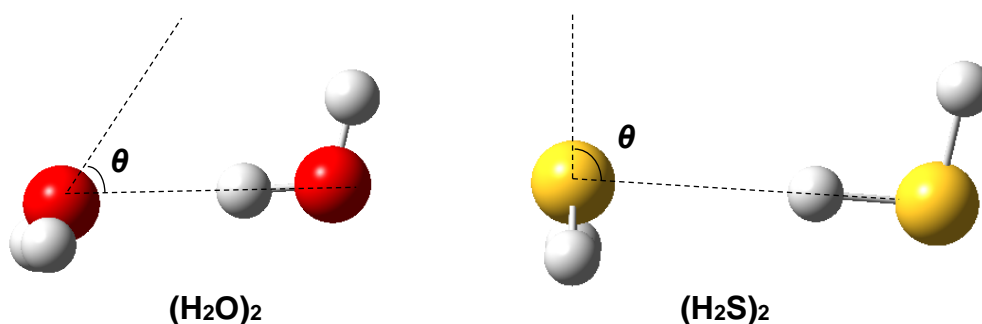
Figure 7.3 The geometries of the lowest energy conformer of $(H_2O)_2$ and $(H_2S)_2$.

This chapter aims to study the nature of the hydrogen bonding interactions thiourea can form, and how they differ to those of urea, by investigating a complex formed between thiourea and water. This work also aims to build on the existing body of work involving organic species and the complexes they form with water.

7.2 Experimental details

Thiourea (Sigma-Aldrich, 99% purity) was used in the experiments in this chapter without further purification, alongside powdered copper (Sigma-Aldrich, 98% purity). As previously noted, copper powder was also used to prepare sample rods. Rods were produced using a table top press and 13 mm die (Specac), by grinding and mixing the solids together and applying ~6 tonnes of pressure. All rods consisted of a 1:1 molar ratio of thiourea to copper. In order to measure the isotopologues of the complex a bespoke reservoir was utilised, which is discussed in section 3.6 in greater detail. In each case 0.2 mL of water was placed in the reservoir, either $H_2^{18}O$ (Sigma Aldrich, 97% ^{18}O) or a 1:1 mixture of D_2O (Sigma Aldrich, 99% D) and H_2O. The D_2O isotopologue was not observed, even when using only D_2O. The details of the CP-FTMW spectrometer used in the experiments in this chapter is described in section 3.

7.3 Spectral analysis

The full 6.5 – 18 GHz spectrum was measured using a CP-FTMW spectrometer, and is shown in figure 7.4, where the most intense lines in the spectrum can be assigned to thiourea[57]. Many weaker transitions are due to the isotopologues of $(NH_2)_2CS$ such as $(NH_2)_2{}^{13}CS$ and ${}^{34}SC(NH_2)_2$. Similar to the other work in this thesis, various fragmentation products are also observed in this spectrum, such as HCCCN. Signals due to $(H_2O)_2$ were also observed, meaning water was present in the sample. After subtracting the assigned transitions to previously reported molecules, a pattern of a-type and b-type transitions were identified and fit the Hamiltonian of an asymmetric top. The determined constants are shown in table 7.1, for the species herein referred to as T1.
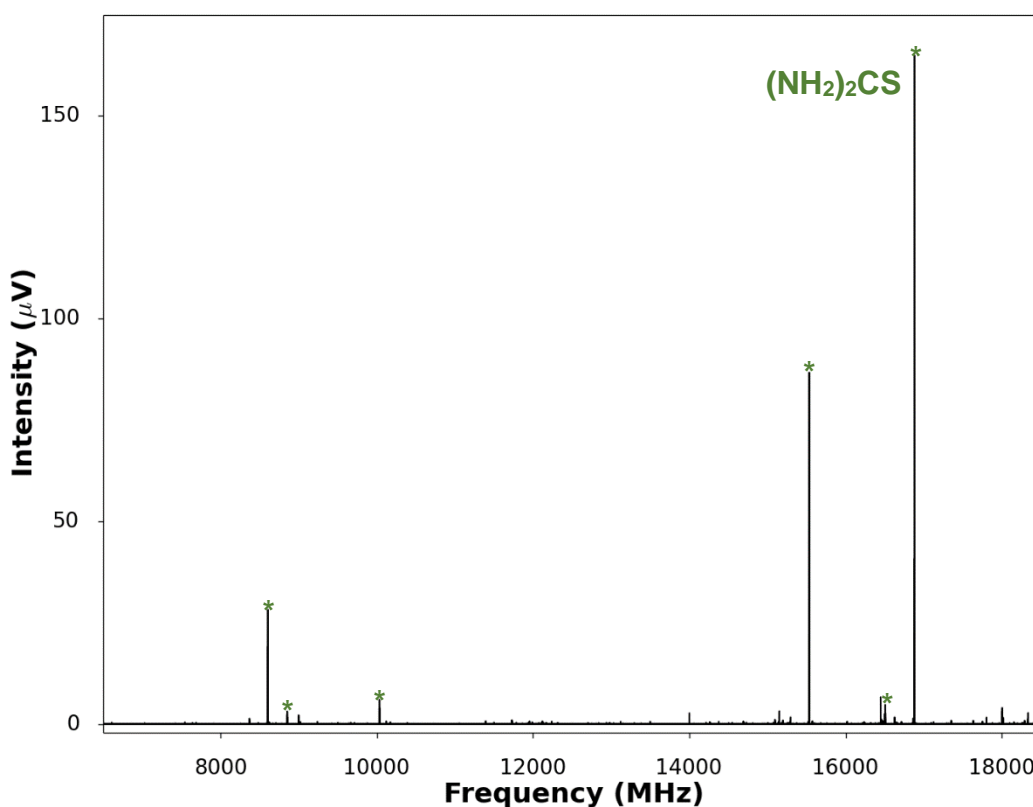
Figure 7.4. The full 6.5 – 18.5 GHz spectrum of the ablation of a 1:1 copper/thiourea rod in the presence of a supersonic expansion of argon held at a stagnation pressure of 6 bar. The spectrum consists of 3240k FIDs.

	T1
A_0 / **MHz**	5361.5776(18)
B_0 / **MHz**	2329.4520(21)
C_0 / **MHz**	1628.5380(21)
D_{JK} / **kHz**	2.904(24)
D_J / **kHz**	1.177(20)
D_K / **kHz**	3.919(66)
d_1 / **Hz**	60.55(63)
χ_{aa} (N_1) / (MHz)	1.241(50)
χ_{bb}-χ_{cc} (N_1) / (MHz)	5.65(11)
χ_{aa} (N_2) / (MHz)	2.221(29)
χ_{bb}-χ_{cc} (N_2) / (MHz)	6.354(79)
N	57
$\sigma_{r.m.s}$ / **kHz**	17.5

Table 7.1 Table of fitted constants for the fitted species T1.

The transitions of T1 are split due to hyperfine effects which is consistent with the presence of two quadrupolar nuclei each possessing I = 1. Given the composition of the rod and gas sample, these nuclei are likely to be nitrogen. The inertia defect, Δ = -0.884 u A^2, suggests T1 is a non-planar species. Figure 7.5 shows two transitions of the fitted species, where the transitions are split due to the asymmetry of the molecule and from the hyperfine effects. The transitions were fit to an S reduced[67] Hamiltonian for an asymmetric top using Western's PGOPHER[78] program.
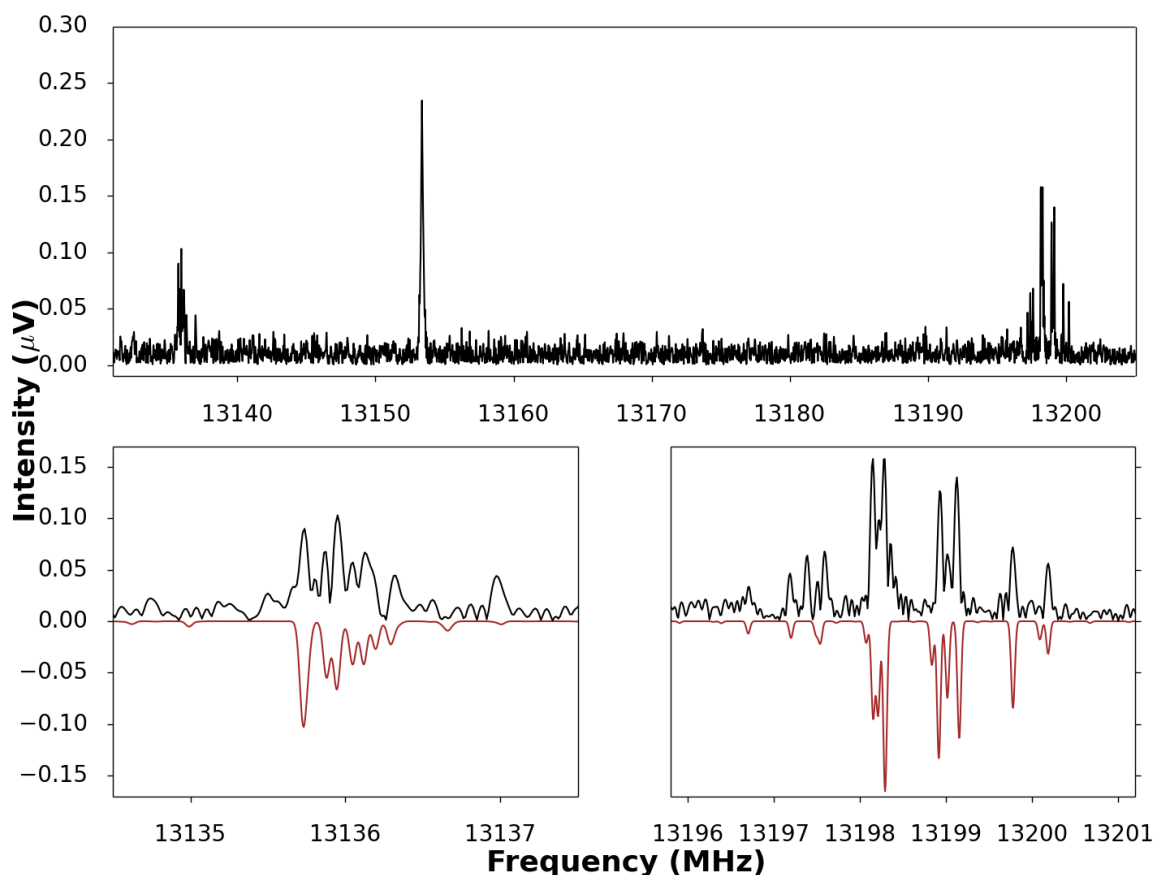
Figure 7.5. (Top): A section of the rotational spectrum, from 13.13 to 13.21 GHz (3240k FIDs). (Bottom left): An expanded view showing $J' \rightarrow J'' = 4 \rightarrow 3$ with the experimental spectrum in black and simulation in brown. (Bottom right): An expanded view showing $J' \rightarrow J'' = 3 \rightarrow 2$ R branch transition in black and simulation in brown.

A variety of species were initially explored. Given the presence of signals due to $(H_2O)_2$, conformers of a complex between thiourea and water were amongst the first to be investigated. Complexes analogous to the $(H_2N)_2CO \cdots HNCO$ complex discussed in section 5 were also explored. Two predominant conformers of a complex between thiourea and water were identified by *ab initio* calculations. The calculated rotational constants at the MP2/aug-cc-pVTZ level of theory for the two lowest energy conformers of $(NH_2)_2CS \cdots H_2O$ are shown in table 7.2. The corresponding structures are shown in figure 7.6.

	A	B
A / MHz	5230.935	10352.917
B / MHz	2345.735	1481.531
C / MHz	1629.238	1303.976
μ_a / D	2.034	8.394
μ_b / D	-3.452	0.003
μ_c / D	-1.137	0.012
E / cm^{-1}	0	120

Table 7.2 The calculated rotational constants, dipole moments and relative energies of two conformers of $(NH_2)_2CS \cdots H_2O$ at the MP2/aug-cc-pVTZ level of theory.

A

B
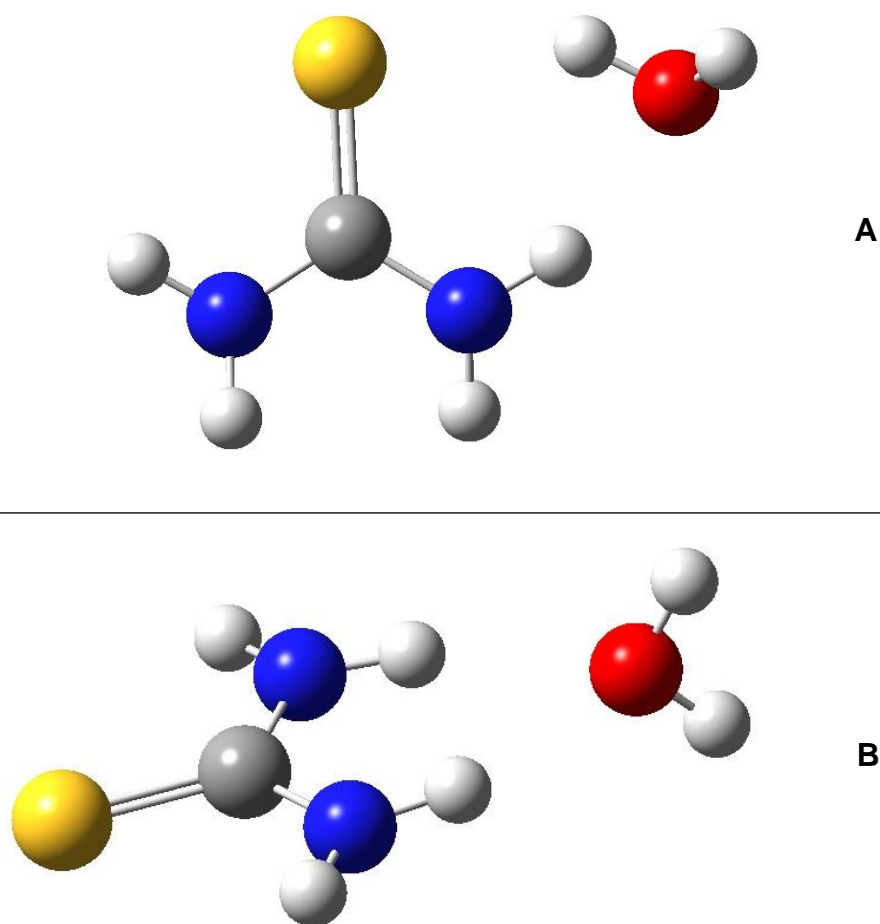
Figure 7.6 The two lowest energy conformers of $(NH_2)_2CS \cdots H_2O$ calculated at the MP2/aug-cc-pVTZ level of theory.

Conformer A exhibits a hydrogen bonded geometry, similar to the $(H_2N)_2CO\cdots HNCO$ complex discussed in section 5, with water forming two hydrogen bonding interactions. Conformer B exhibits a bifurcated hydrogen bonding geometry, with the oxygen atom of water forming two hydrogen bonds to the different NH_2 groups of $(NH_2)_2CS$. This conformer also features a geometry where the NH_2 groups are planar. The energy difference between both conformers is relatively small at ~1.4 kJ mol^{-1} meaning potentially both conformers could be observed. Given the magnitude of the calculated dipole moments and rotational constants both conformers should be easily distinguishable, with conformer B exhibiting strong *a*-type transitions and smaller spacing between transitions.

In the spectrum of T1 both *a*-type and *b*-type transitions were observed, which is consistent with the calculated dipole moments of A. Shown in table 7.3 is a comparison of the rotational constants of T1 and those calculated for A. The fitted constants of T1 generally agree with the calculated constants, suggesting that the identity of T1 is a low energy conformer of the $(NH_2)_2CS\cdots H_2O$ complex. Further experiments using D_2O and $H_2^{18}O$ were performed to confirm the identity of T1. In each spectrum a similar set of transitions were identified and fit, with the determined constants shown in table 7.4.

	T1	MP2/aug-cc-pVTZ **A**
***A* / MHz**	5361.5776(18)	5230.9352
***B* / MHz**	2329.4520(21)	2345.7351
***C* / MHz**	1628.5380(21)	1629.2380

Table 7.3 The rotational constants determined for the $(NH_2)_2CS\cdots H_2O$ complex alongside the calculated constants from the r_e geometry.

	$(NH_2)_2CS\cdots DHO$	$(NH_2)_2CS\cdots H_2^{18}O$
A_0 / MHz	5350.7919(20)	5348.7879(33)
B_0 / MHz	2284.1536(17)	2187.8597(21)
C_0 / MHz	1605.5174(16)	1557.0217(12)
D_{JK} / kHz	2.087(46)	2.16(30)
D_J / kHz	0.641(27)	1.286(14)
D_K / kHz	[3.919][a]	3.19(62)
d_1 / Hz	[60.55][a]	[60.55][a]
X_{aa} (N_1) / (MHz)	[1.241][a]	[1.241][a]
X_{bb-cc} (N_1) / (MHz)	[5.65][a]	[5.65][a]
X_{aa} (N_2) / (MHz)	[2.221][a]	[2.221][a]
X_{bb-cc} (N_2) / (MHz)	[6.354][a]	[6.354][a]
N	44	48
$\sigma_{r.m.s}$ / kHz	19.3	17.9

Table 7.4 Table of fitted constants for the $(NH_2)_2CS\cdots H_2O$ complex and two measured isotopologues. [a] Denotes parameters that could not be determined and hence were fixed to the corresponding value for the parent species.

Two isotopologues of $(NH_2)_2CS\cdots H_2O$ were measured, $(NH_2)_2CS\cdots DHO$ and $(NH_2)_2CS\cdots H_2^{18}O$. The identity of the deuterated isotopologue was confirmed as $(NH_2)_2CS\cdots DHO$, where the deuterium is involved in the hydrogen bonding interaction, by comparison of scaled constants for the corresponding structures. The signal to noise ratio of the transitions due to the parent complex was insufficient to measure the $(NH_2)_2C^{34}S\cdots H_2O$ or $(NH_2)_2^{13}CS\cdots H_2O$ species at natural abundance and ^{13}C / ^{34}S /^{15}N synthetically enriched isotopologues of thiourea are prohibitively expensive. Hyperfine splitting was resolved and the corresponding nuclear quadrupole coupling constants were able to be determined for the parent species.

7.4 Structural Analysis

Due to the lack of isotopic substitution at every atom position only limited structural information is able to be determined. The r_0 structure was unable to be determined due to the lack of isotopic substitution on the thiourea unit of the complex. The r_s structure, generated based on Kraitchman's equations[76] and using Kisiel's program KRA, is compared to the r_e structure in figure 7.6. This method assumes that the structure of the isotopologues is identical to the parent species. The position of the oxygen atom and the hydrogen atom that is involved in a hydrogen bonding interaction to the sulphur atom of thiourea is shown in figure 7.7. The coordinates of the oxygen and hydrogen atom are shown and compared to calculated results in table 7.5.
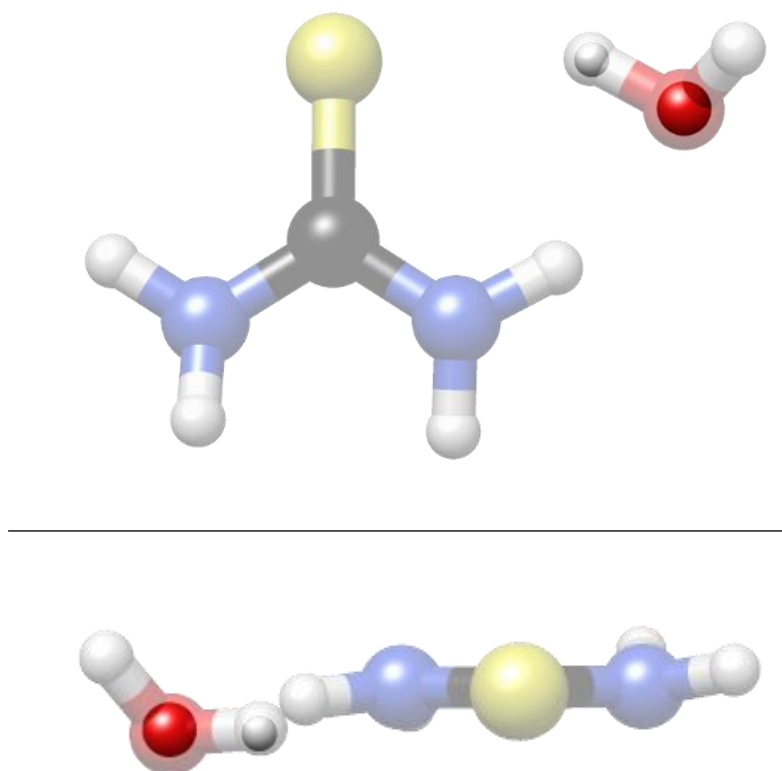
Figure 7.7 Geometry of the $(NH_2)_2CS \cdots H_2O$ complex from the c inertial axis (top) and from the axis of the C=S bond (bottom).The calculated r_e geometry is represented by the larger transparent spheres and the r_s determined atom positions are represented by the smaller opaque spheres.

Atom	a / Å	b / Å	c / Å	Method
O	-2.67180(56)	-0.3528(43)	0.058(26)	r_s
	-2.655998	-0.355860	0.097923	r_e
H	-2.07278(73)	0.4189(36)	0.148(10)	r_s
	-2.060442	0.423397	0.121808	r_e

Table 7.5 Values of atomic coordinates for the oxygen and hydrogen atom of water in the $(NH_2)_2CS \cdots H_2O$ complex. The r_e structure was calculated at the MP2/aug-cc-pVTZ level of theory.

The position of the oxygen and hydrogen atoms determined by the substitution geometry agree well with the r_e geometry as shown in figure 7.7. The coordinates shown in table 7.5 show the same comparison, with disagreement only in the small c coordinate of the oxygen atom of water in the complex. Various structural parameters of the calculated r_e structure are shown in table 7.6. The complex features two hydrogen bonding interactions, S···H and H···N. The r(S···H) distance in the complex is of slightly shorter than that of the crystal structure of thiourea, as shown in figure 7.8. The $(NH_2)_2CS \cdots H_2O$ complex adopts a similar structure to part of the crystal structure adopted by thiourea, with the presence of two hydrogen bonding interactions, one to sulphur and the other to a hydrogen atom of the NH_2 group.

	r_e
r(S···H) / Å	2.316
r(O···H) / Å	1.916
∠(CS···H) / °	90.9
∠(NH···O) / °	155.3

Table 7.6 Parameters of the calculated r_e structure of the $(NH_2)_2CS \cdots H_2O$ complex.
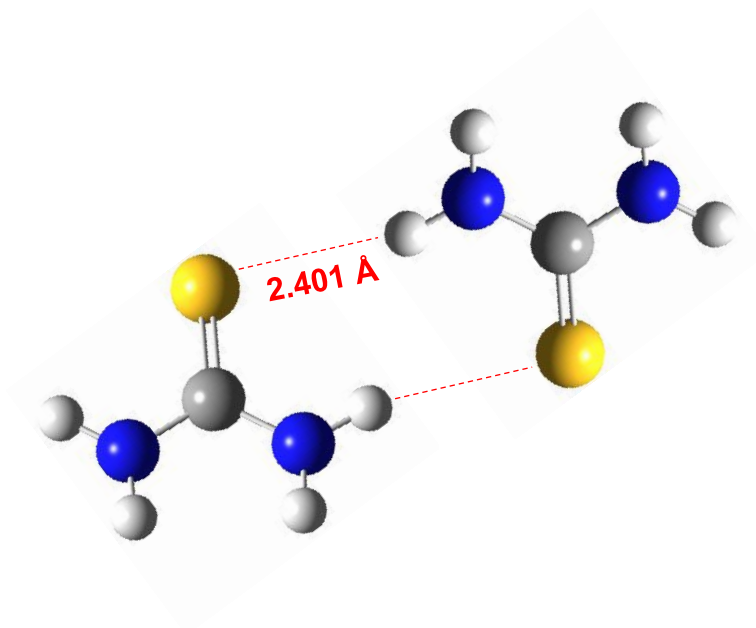
Figure 7.8 Part of the unit cell of crystalline thiourea shown in figure 7.2,[142] with hydrogen bonding interactions labelled and indicated with red lines.

7.5 Conclusions

The $(NH_2)_2CS\cdots H_2O$ complex was observed by microwave spectroscopy in the 6.5 – 18 GHz range for the first time. Only a single conformer was detected, where the water molecule acts as both a hydrogen bond donor and acceptor. $S\cdots H$ and $O\cdots H$ hydrogen bonding interactions form between water and thiourea to stabilise the complex. The length of the hydrogen bonding interactions were calculated to be $r_e(S\cdots H) = 2.316$ Å and $r_e(O\cdots H) = 1.916$ Å. This work could be further extended by performing further isotopic work in order to determine more structural information, or examining similar complexes such as $(NH_2)_2CS\cdots H_2S$. Measurement of similar species would show how the relative strength of the hydrogen bonding interactions of thiourea are affected by the identity of the adduct.

Chapter 8. Conclusions

The rotational spectra of $(C_3H_4N_2)_2$, $(H_2N)_2CO \cdots HNCO$, $(H_2N)_2CO \cdots C_3H_4N_2$ and $(NH_2)_2CS \cdots H_2O$ were measured by microwave spectroscopy for the first time. The complexes described in this thesis were generated by laser ablation and studied using the Newcastle CP-FTMW spectrometer. This work provides further evidence that the combination of laser ablation and CP-FTMW spectroscopy can be effectively used to generate and study weakly bound organic containing complexes.

The imidazole dimer, $(C_3H_4N_2)_2$, has been previously studied using IR spectroscopy[89-90] with the experiments detailed in this thesis being the first reported microwave spectrum of the complex. Geometrical parameters of the lowest energy conformer of the $(C_3H_4N_2)_2$ complex have been determined experimentally for the first time. The complex was shown to exhibit a twisted geometry with an almost perpendicular T-shaped arrangement of the imidazole monomer units and a single intermolecular NH $\cdots$ N hydrogen bonding interaction. This work could be further extended by examining similar systems, for example those that contain pyrrolic or pyridinic nitrogen atoms and measuring the complexes they form with imidazole. The study of substituted imidazoles would be of interest as it would determine whether the substituents of the ring affect the strength or formation of the intermolecular hydrogen bond. Measuring and determining the geometry of a trimer of imidazole, which has been studied by IR spectroscopy, would also be of interest and extend the scope of this work.

This work also presents the first study of the lowest energy conformer of a complex between urea and isocyanic acid, $(H_2N)_2CO \cdots HNCO$. The complex consists of two distinct hydrogen bonding interactions between urea and isocyanic acid, where the NH group of the isocyanic acid acts as both a hydrogen bond donor and acceptor. The length of the hydrogen bonding interactions were determined as $r(O \cdots H) = 1.866(11)$ Å (r_0) and $r(N \cdots H) = 2.261(13)$ Å (r_0). Measurement of similar but more complex species such as urea and two isocyanic acid units would further explore the hydrogen bonding capability of urea.

Expanding on the previous work of the intermolecular interactions of urea and imidazole, a conformer of a complex of the two was measured for the first time. The identity and shape of the complex was confirmed with isotopic experiments and *ab*

initio calculations. The calculated geometry shows the complex features two hydrogen bonding interactions, O⋯H and N⋯H. No other conformers were observed despite the relatively small energy difference of the lowest energy conformers. Measuring the complex using a different carrier gas such as neon, may allow for the measurement of additional conformers.

A conformer of a complex of water and thiourea, $(NH_2)_2CS \cdots H_2O$, was also measured for the first time in this work. The nuclear quadrupole coupling constants of the complex were determined for both nitrogen nuclei. The complex exhibits a similar structure to other organic water containing complexes, such as the formamide water complex.[138-139] The calculated geometry shows the water is involved in two intermolecular hydrogen bonds to the thiourea, forming O⋯H and S⋯H interactions. Measurement of additional isotopologues would give experimental values for the length of these interactions.

The efficacy of mixing copper with organic species for generating molecules in the gas phase, using laser ablation, has been shown with this work. All of the complexes described here were generated using rods consisting of an equimolar concentration of copper and organics. Copper containing species were absent in the measured spectra, unless a source of halogens, such as CCl_4, were used in the gas sample. In those cases the corresponding copper halide is observed, alongside signals resulting from the organic and its fragmentation products. Additional avenues for experiments to optimise rod composition, with regards to signal intensity, could explore the effect of the properties of the laser. Adjusting the laser power or type are some examples of variables that could be explored. Seeking to optimise signals is advantageous, and often sought after, as it may offer opportunities to observe isotopologues that otherwise may not be accessible. A limitation of microwave spectroscopy is the necessity of measuring isotopologues of species to gain structural information. If isotopologues are observable at natural abundance then this eliminates any additional cost or time spent obtaining or measuring synthetically enriched samples. This is demonstrated by the experiments detailing rod composition, where the ^{13}C containing isotopologues of imidazole were not observed when using a rod of pure imidazole, compared to when using a rod of 1:1 molar ratio of copper and imidazole.

References

1. C. E. Cleeton and N. H. Williams, *Phys. Rev.*, 1934, **45**, 234-237

2. J. W. Simmons and W. Gordy, *Phys. Rev.*, 1948, **73**, 713.

3. W. E. Good, *Phys. Rev.*, 1946, **70**, 213.

4. W. Gordy and M. Kessler, *Phys. Rev.*, 1947, **71**, 640

5. R. S. Henderson, *Phys. Rev.*, 1948, **74**, 107.

6. J. M. Jauch, *Phys. Rev.*, 1947, **72**, 715.

7. C. H. Townes, B. P. Dailey, *J. Chem. Phys.*, 1949, **17**, 782.

8. B. P. Dailey, R. L. Kyhl, M. W. P. Strandberg, J. H. Van Vleck, and E. B. Wilson, 1946, *Phys. Rev.*, 1946, **70**, 984.

9. D. K. Coles and W. E. Good, *Phys. Rev.*, 1946, **70**, 979.

10. M. L. Stitch, A. Honig and C. H. Townes, *Phys. Rev.*, 1952, **86**, 813.

11. M. L. Stitch, A. Honig and C. H. Townes, *Rev. Sci. Instrum.*, 1954, **25**, 759.

12. A. C. Cheung, D. M. Rank, C. H. Townes, D. D. Thornton and W. J. Welch, *Phys. Rev. Lett.*, 1968, **21**, 1701.

13. A. C. Cheung, D. M. Rank and C. H. Townes, *Astrophys. J.*, 1969, **157**, L13.

14. A. C. Cheung, D. D. Thornton, D. M. Rank, W. J. Welch and C. H. Townes, *Nature*, 1969, **221**, 626.

15. N. W. Broten, T. Oka, L. W. Avery, J. M. MacLeod and H. W. Kroto, *Astrophys. J.*, 1978, **223**, L105.

16. M. W. Sinclair, N. Fourikis, J. C. Ribes, B. J. Robinson, R. D. Brown and P. D. Godfrey, *Aust. J. Phys.*, 1973, **26**, 85.

17. 14. F. F. Gardner and G. Winnewisser, *Astrophys. J.*, 1975, **195**, L127.

18. L. E. Snyder, D. Buhl, B. Zuckerman and P. Palmer, *Phys. Rev. Lett.*, 1969, **22**, 679.

19. R. H. Rubin, G. W. Swenson, R. C. Benson, H. L. Tigelaar, and W. H. Flygare, *Astrophys. J.*, 1971, **169**, L39.

20. T. J. Balle, E. J. Campbell, M. R. Keenan, and W. H. Flygare, *J. Chem. Phys.*, 1979, **71**, 2723.

21. T. J. Balle and W. H. Flygare, *Rev. Sci. Instrum.*, 1981, **52**, 33.

22. G. G. Brown, B. C. Dian, K. O. Douglass, S. M. Geyer, S. T. Shipman, and B. H. Pate, *Rev. Sci. Instrum.*, 2008, **79**, 053103.

23. G. B. Park and R. W. Field, *J. Chem. Phys.*, 2016, **144**, 200901.

24. S. P. Dempster, O. Sukhorukov, Q.Lei, and W. Jäger, *J. Chem. Phys.*, 2012, **137**, 174303.

25. J. M. Oldham, C. Abeysekera, B. Joalland, L. N. Zack1, K. Prozument, I. R. Sims, G. B. Park, R. W. Field, and A. G. Suits, *J. Chem. Phys.*, 2014, **141**, 154202.

26. I. A. Finneran, D. B. Holland, P. B. Carrol and G. A Blake, *Rev. Sci. Instrum.*, 2013, **84**, 083104.

27. D. Patterson, M. Schnell and J. M. Doyle, *Nature*, 2013, **497**, 475.

28. S. Lobsiger, C. Perez, L. Evangelisti, K. K. Lehmann and B. H. Pate, *J. Phys. Chem. Lett.*, 2015, **6**, 196.

29. V. A. Shubert, D. Schmitz, D. Patterson, J. M. Doyle, and M. Schnell, *Angew. Chem. Int. Ed.*, 2014, **53**, 1152.

30. C. Medcraft, R. Wolf, M. Schnell, *Angew. Chem. Int. Ed.*, 2014, **53**, 11656.

31. E. Arunan, G. R. Desiraju, R. A. Klein, J. Sadlej, S. Scheiner, I. Alkorta, D. C. Clary, R. H. Crabtree, J. J. Dannenberg9, P. Hobza, H. G. Kjaergaard, A. C. Legon, B. Mennucci, D. J. Nesbitt, *Pure Appl. Chem.*, 2011, **83**, 1619.

32. K. –M. Marstokk and H. Mollendal, *J. Mol. Struct.*, 1970, **5**, 205

33. K. –M. Marstokk and H. Mollendal, *J. Mol. Struct.*, 1971, **7**, 101

34. K. S. Buckton and R. G. Azrak, *J. Chem. Phys.*, 1970, **52**, 5652.

35. R. G. Azrak and E. B. Wilson, *J. Chem. Phys.*, 1970, **52**, 5299.

36. P. Buckley and M. Brochu, *Can. J. Chem.*, 1972, **50**, 1149.

37. A. S. Khalil, T. M. Duguay and R. J. Lavrich, *J. Mol. Struct.*, 2017, **1138**, 12.

38. T. R. Dyke, B. J. Howard and W. Klemperer, *J. Chem. Phys.*, 1972, **56**, 2442.

39. T. R. Dyke and S. J. Muenter, *J. Chem. Phys.*, 1974, **60**, 2929.

40. A. C. Legon and D. J. Millen, *Acc. Chem. Res.*, 1987, **20**, 39.

41. S. L. Stephens, D. M. Bittner, V. A. Mikhailov, W. Mizukami, D. P. Tew, N. R. Walker and A. C. Legon, *Inorg. Chem.*, 2014, **53**, 10722.

42. J. C. Mullaney, S. L. Stephens, D. P. Zaleski, M. J. Sprawling, D. P. Tew, N. R. Walker and A. C. Legon, *J. Phys. Chem. A*, 2015, **119**, 9636.

43. C. Medcraft, D. M. Bittner, D. P. Tew, N. R. Walker and A. C. Legon, *J. Chem. Phys.*, 2016, **145**, 194306.

44. S. Melandri, M. E. Sanz, W. Caminati,, P. G. Favero, and Z. Kisiel, *J. Am. Chem. Soc.*, 1998, **120**, 11504.

45. W. Caminati, L. B. Favero, P. G. Favero, A. Maris, and Sonia Melandri, *Angew. Chem. Int. Ed.*, 1998, **37**, 792.

46. P. A. Stockman, G. A. Blake F. J. Lovas and Richard D. Suenram, *J. Chem. Phys.*, 1997, **107**, 3782.

47. L. Evangelisti and W. Caminati, *Phys. Chem. Chem. Phys.*, 2010, **12**, 14433.

48. L. Evangelisti, Q. Gou, G. Feng, W. Caminati, G. J. Mead, I. A. Finneran, P. B. Carroll and G. A. Blake, *Phys. Chem. Chem. Phys.*, 2017, **19**, 568.

49. C. Pérez, M. T. Muckle, D. P. Zaleski, N. A. Seifert, B. Temelso, G. C. Shields, Z. Kisiel and B. H. Pate, *Science*, 2012, **336**, 897.

50. D. Loru, M. A. Bermudez and M. E. Sanz, *J. Chem. Phys.*, 2016, **145**, 074311.

51. A. K. Huff, R. B. Mackenzie, C. J. Smith and K. R. Leopold, *J. Phys. Chem. A*, 2017, **121**, 5659.

52. Y. Ohshima, Y. Endo, *Chem. Phys. Lett.*, 1993, **213**, 95.

53. J. B. Hopkins, P. R. R. Langridge-Smith, M. D. Morse and R. E. Smalley, *J. Chem. Phys.*, 1983, **78**, 1627.

54. K. A. Walker and M. C. L. Gerry, *J. Mol. Spectrosc.*, 1997, **182**, 178.

55. K. D. Hensel, C. Styger, W. Jager, A. J. Merer and M. C. L. Gerry, *J. Chem. Phys.*, 1993, **99**, 3320.

56. F. J. Lovas, Y. Kawashima. J. –U. Grabow, R. D. Suenram, G. T. Fraser and E. Hirota, *Astrophys. J.*, 1995, **455**, L201.

57. A. Lesarri, S. Mata, S. Blanco, J. C. López, and J. L. Alonso, *J. Chem. Phys.*, 2004, **120**, 6191.

58. P. Ecija,M. Vallejo-Ljpez, I. Uriarte, F. J. Basterretxea, A Lesarri, J. A. Fernandez and E. J. Cocinero, *ChemPhysChem*, 2016, **17**, 3030.

59. J. C. Mullaney, D. P. Zaleski, D. P. Tew, N. R. Walker, A. C. Legon, *ChemPhysChem*, 2016, **8**, 1154.

60. J. C. Mullaney, C. Medcraft, D. P. Tew, L. Lewis-Borrell, B. T. Golding, N. R. Walker and A. C. Legon, *Phys. Chem. Chem. Phys.*, 2017, **19**, 25080.

61. R. Custelcean, *Chem. Comm.*, 2008, 295.

62. J. F. Brandts and L. Hunt, *J. Am. Chem. Soc.*, 1967, **89**, 4826.

63. W. Caminati, S. Melandri, I. Rossi and P. G Favero, *J. Am. Chem. Soc.*, 1999, **121**, 10098.

64. C. Calabrese, Q. Gou, A. Maris, W. Caminati and S. Melandri, *J. Phys. Chem. Lett.*, 2016, **7**, 1513.

65. P. Ecija, M. Vallejo-Lopez, L. Evangelisti, J. A. Fernandez, A. Lesarri, W. Caminati, and E. J. Cocinero, *ChemPhysChem*, 2014, **15**, 918.

66. C. H. Townes and A. L. Schalow, *Microwave Spectroscopy*, Dover Publications, New York, 2012.

67. J. K. G. Watson, *Mol. Phys.*, 1968, **15**, 479

68. J. K. G. Watson, *J. Chem. Phys.*, 1967, **46**, 1935.

69. J. M. Thomas, N. R. Walker, S. A. Cooke and M. C. L. Gerry, *J. Am. Chem. Soc.*, 2004, **126**, 1235.

70. S. G. Francis, N. R. Walker and A. C. Legon, *Chem. Phys. Lett.*, **452**, 1.

71. J. L. Alonso, F. J. Lorenzo, J. C. Lopez, A. Lesarri, S. Mata and H. Driezler, *Chem. Phys.,* 1997, **218**, 267.

72. H. Driezler, *Mol. Phys.*, 1986, **59**, 1.

73. J. C. McGurk, T. G. Schmalz and W. H. Flygare, *J. Chem. Phys.*, 1974, **60**, 4181.

74. J. H. Yoo, H. Kockert, J. C. Mullaney, S. L. Stephens, C. J. Evans, N. R. Walker and R. J. Le Roy, *J. Mol. Spectrosc.*, 2016, **330**, 80.

75. Z. Kisiel, *J. Mol. Spectrosc.*, 2003, **218**, 58.

76. J. Kraitchman, *Am. J. Phys.*, 1953, **21**, 17.

77. C. C. Costain, *J. Chem. Phys.*, 1958, **29**, 864.

78. C. M. Western, B. E. Billinghurst, *Phys. Chem. Chem. Phys.*, 2017, **19**, 10222.

79. S. L. Stephens and N. R. Walker, *J. Mol. Spectrosc.*, 2010, **263**, 27.

80. www.python.org

81. www.tek.com

82. J. L. Neill, K. O. Douglass, B. H. Pate and D. W. Pratt, *Phys. Chem. Chem. Phys.*, 2011, **13**, 7253.

83. G. Scoles, D. Bassi, U. Buck and D. Laine, *Atomic and Molecular Beam Methods*, Oxford University Press, Oxford, 1988.

84. S. Khademi, J. O'Connell, J. Remis, Y. Robles-Colmenares, J. W. Miercke and R. M. Stroud, *Science*, 2004, **305**, 1587.

85. L. Zheng, D. Kostrewa, S. Berneche, F. K. Winkler and X. –D. Li, *Proc. Natl. Acad. Sci. U.S.A.*, 2004, **101**, 17090.

86. B. M. Craven, R. K. McMullan, J. D. Bell and H. C. Freeman, *Acta Cryst.*, 1977, **B33**, 2585.

87. R. K. McMullan, J. Epstein, J. R. Ruble and B. M. Craven, *Acta Cryst.*, 1979, **B35**, 688.

88. S. Martinez-Carrera, *Acta Cryst.*, 1966, **20**, 783.

89. M. Y. Choi and R. E. Miller, *J. Phys. Chem. A*, 2006, **110**, 9344.

90. M. Y. Choi and R. E. Miller, *Chem. Phys. Lett.*, 2009, **477**, 276.

91. C. Hattig, W. Klopper, A. Kohn and D. P. Tew, *Chem. Rev.*, 2012, **112**, 4.

92. D. Christen, J. H. Griffiths and J. Sheridan, *Z. Naturforsch.*, 1982, **37a**, 1378.

93. D. Boucher, J. Burie, J. Demaison, A. Dubrulle, J. Legrand and B. Segrand, *J. Mol. Spectrosc.*, 1977, **64**, 290.

94. 136. V. W. Laurie, *J. Chem. Phys.*, 1959, **31**, 1500.

95. R. A. Creswell, G. Winnewisser and M. C. L. Gerry, *J. Mol. Spectrosc.*, 1977, **65**, 420.

96. H. M. Pickett, *J. Mol. Spectrosc.*, 1973, **46**, 335.

97. C. Kirby, H. W. Kroto and D. R. M. Walton, *J. Mol. Spectrosc.*, 1980, **83**, 261.

98. A. J. Alexander, H. W. Kroto and D. R. M. Walton, *J. Mol. Spectrosc.*, 1976, **62**, 175.

99. N. W. Broten, J. M. MacLeod, L. W. Avery, W. M. Irvine, B. Hoglund, P. Friberg and A. Hjalmarson, *Astrophys. J.*, 1984, **276**, L25.

100. G. Winnewisser, *J. Chem. Phys.*, 1972, **57**, 1803.

101. G. Winnewisser, *J. Chem. Phys.*, 1972, **56**, 2944.

102. F. Gowland Hopkins, *Nature*, 1930, **126**, 329.

103. P. L. Whitney and C. Tanford, *J. Biol. Chem.*, 1962, **237**, 1735.

104. J. F. Brandts and L. Hunt, *J. Am. Chem. Soc.*, 1967, **89**, 4826.

105. D. R. Canchi, D. Paschek and A. E. Garcia, *J. Am. Chem. Soc.*, 2010, **132**, 2338.

106. T. T. Herskovits, *Biochemistry*, 1963, **2**, 336.

107. S. Nilsson, L. Piculell and M. Malmsten, *J. Phys. Chem.*, 1990, **94**, 5149.

108. A. Wallqvist, D. G. Covell and D. Thirumalai, *J. Am. Chem. Soc.*, 1998, **120**, 427.

109. B. J. Bennion and V. Daggett, 2003, *Proc. Natl. Acad. Sci.*, **100**, 5142.

110. A. Das and C. Mukhopadhyay, *J. Phys. Chem. B*, 2008, **112**, 7903.

111. P. J. Rossky, *Proc. Natl. Acad. Sci.*, 2008, **105**, 16825.

112. H. Guth, S. Klein, W. Treutmann, C. Scheringer and G. Heger, *Zeitschrift fur Krist. – New Cryst. Struct.*, 1980, **153**, 137.

113. A. Olejniczak, K. Ostrowska and A. Katrusiak, *J. Phys. Chem. C*, 2009, **113**, 15761.

114. R. B. Hammond, C. Ma, K. J. Roberts, P. Y. Ghi and R. K. Harris, *J. Phys. Chem. B.*, 2003, **107**, 11820.

115. S. Wishkerman, J. Bernstein and M. B. Hickey, *Cryst. Growth Des.*, 2009, **9**, 3204.

116. G. Smith, K. E. Baldry, K. A. Byriel and C. H. L. Kennard, *Aust. J. Chem.*, 1997, **50**, 727.

117. A. E. Smith, *Acta Cryst.*, 1952, **5**, 224.

118. P. D. Godfrey, R. D. Brown and A. N. Hunter, *J. Mol. Struct.*, 1997, **413-414**, 405.

119. T. Oka, *J. Phys. Soc. Jpn.*, 1960, **15**, 2274.

120. J. P. Gordon, H. J. Zeiger and C. H. Townes, *Phys. Rev.*, 1954, **95**, 282.

121. S. D. Yim, S. J. Kim, J. H. Baik, I. Nam, Y. S. Mok, J. Lee, B. K. Cho and S. H. Oh, *Ind. Eng. Chem. Res.*, 2004, **43**, 4856.

122. M. C. Stumpe and H. Grubmuller, *J. Am. Chem. Soc.*, 2007, **129**, 16126.

123. G. S. Grubbs, C. T. Dewberry, K. C. Etchison, K. E. Kerr and S. A. Cooke, *Rev. Sci. Instrum.*, 2007, **78**, 096106.

124. M. Sun, D. T. Halfen, J. Min, B. Harris, D. J. Clouthier and L. M. Ziurys, *J. Chem. Phys.*, 2010, **133**, 174301.

125. U. Kretschmer, D. Consalvo, A. Knaack, W. Schade, W. Stahl and H. Driezler, *Mol. Phys.*, 1995, **87**, 1159.

126. K. D. Hensel and M. C. L. Gerry, *J. Chem. Soc.*, *Faraday Trans.*, 1997, **93**, 1053.

127. C. Medcraft, J. C. Mullaney, N. R. Walker and A. C. Legon, *J. Mol. Spectrosc.*, 2017, **335**, 61.

128. A. Lesarri, S. Mata, J. C. Lopez and J. L. Alonso, *Rev. Sci. Instrum.*, 2003, **74**, 4799.

129. S. Antonlinez, A. Lesarri, S. Mata, S. Blanco, J. C. Lopez and J. L. Alonso, *J. Mol. Struct.*, **612**, 125.

130. A. Lesarri, S. Mata, E. J. Cocinero, S. Blanco, J. C. Lopez, and J. L. Alonso, *Angew. Chem. Int. Ed.*, 2002, **41**, 4673.

131. S. Blanco, A. Lesarri, J. C. Lopez and J. L. Alonso, *J. Am. Chem. Soc.*, 2004, **126**, 11675.

132. A. Engdahl, B. Nelander, *Chem. Phys. Lett.*, 1983, **100**, 129.

133. P. Herbine and T. R. Dyke, *J. Chem. Phys.*, 1985, **83**, 3768.

134. O. Dopfer, G. Reiser, K. Muller-Dethlefs, E. W. Schlag and S. D. Colson, *J. Chem. Phys.*, 1994, **101**, 974.

135. M. Gerhards, M. Schmitt and K. K. Stahl, *J. Chem. Phys.*, 1996, **104**, 967.

136. W. Caminati, L. B. Favero, P. G. Favero, A. Maris and S. Melandri, *Angew. Chem. Int. Ed.*, 1998, **37**, 792.

137. S. Suzuki, P. G. Green, R. E. Bumgarner, S. Dasgupta, W. A. Goddard and G. A. Blake, *Science*, 1992, **257**, 942.

138. F. J. Lovas, R. D. Suenram, G. T. Fraser, C. W. Gillies and J. Zozom, *J. Chem. Phys.*, 1988, **88**, 722.

139. S. Blanco, J. C. Lopez, A. Lesarri and J. L. Alonso, *J. Am. Chem. Soc.*, 2006, **128**, 12111.

140. J. A. Gordon and J. R. Warren, *J. Biol. Chem.*, 1968, **243**, 5663.

141. J. A. Gordon and W. P. Jencks, *Biochem*, 1963, **2**, 47.

142. M. M. Elcombe and J. C. Taylor, *Acta Cryst.*, 1968, **24**, 410.

143. J. R. Sabin, *J. Am. Chem. Soc.*, 1970, **93**, 3613.

144. M. J. Frisch, J. A. Pople and J. E. Del Bene, *J. Phys. Chem.*, 1985, **89**, 3664.

145. A. Bhattacherjee, Y. Matsuda, A. Fujii and S. Wategaonkar, *ChemPhysChem*, 2013, **14**, 905.

146. J. A. Odutola and T. R. Dyke, *J. Chem. Phys.*, 1980, **72**, 5062.

147. A. Lesarri, S. Mata, S. Blanco, J. C. Lopez and J. L. Alonso, *J. Chem. Phys.*,

Appendix

List of publications:

1. J. C. Mullaney, C. Medcraft, D. P. Tew, L. Lewis-Borrell, B. T. Golding, N. R. Walker and A. C. Legon, *Phys. Chem. Chem. Phys.*, 2017, **19**, 25080.

2. C. Medcraft, J. C. Mullaney, N. R. Walker and A. C. Legon, *J. Mol. Spectrosc.*, 2017, **335**, 61.

3. J. H. Yoo, H. Köckert, J. C. Mullaney, S. L. Stephens, C. J. Evans, N. R. Walker and R. J. Le Roy, *J. Mol. Spectrosc.*, 2016, **330**, 80.

4. J. C. Mullaney, D. P. Zaleski, D. P. Tew, N. R. Walker, A. C. Legon, *ChemPhysChem*, 2016, **8**, 1154.

5. D. P. Zaleski, J. C. Mullaney, D. M. Bittner, D. P. Tew, N. R. Walker and A. C. Legon, *J. Chem. Phys.*, 2015, **143**, 164314.

6. J. C. Mullaney, S. L. Stephens, D. P. Zaleski, M. J. Sprawling, D. P. Tew, N. R. Walker and A. C. Legon, *J. Phys. Chem. A*, 2015, **119**, 9636.

List of presentations:

1. *Microwave spectra of Ar···AgI and H_2O···AgI produced by laser ablation*, International Symposium on Molecular Spectroscopy, University of Illinois (2017), http://hdl.handle.net/2142/96872

2. *The rotational spectrum of the urea isocyanic acid complex* – International Symposium on Molecular Spectroscopy, University of Illinois (2016), http://hdl.handle.net/2142/91217

3. *Geometry of an Isolated Dimer of Imidazole Characterised by Rotational Spectroscopy and Ab Initio Calculations* – International Symposium on Molecular Spectroscopy, University of Illinois (2016), http://hdl.handle.net/2142/91259

4. *Rotational spectra of the imidazole and urea dimers* – Spectroscopy and Dynamics Group Meeting, Warwick University (2016)

5. *The broadband rotational spectrum of the imidazole dimer* – Annual Northern Universities Meeting Of Chemical Physics XXV - Leeds University (2015)